TÉCNICO LISBOA

Transport through driven systems - Application to Floquet topological states

Pedro António Correia Ninhos

Thesis to obtain the Master of Science Degree in

Engineering Physics

Supervisors: Prof. Dr. Pedro José Gonçalves Ribeiro
Prof. Dr. Miguel António da Nova Araújo

Examination Committee

Chairperson: Prof. Dr. Carlos Manuel Dos Santos Rodrigues da Cruz
Advisor: Prof. Dr. Miguel António da Nova Araújo
Member of the Committee: Prof. Dr. Pedro Domingos Santos do Sacramento

September 2020

Acknowledgments

I am deeply thankful to my supervisors, Prof. Dr. Pedro Ribeiro and Prof. Dr. Miguel Araújo, without whom this work would not be possible. I appreciate all their patience and availability to guide me through this work, their involvement from the beginning to the end, and the ideas they contributed with.

Along my degree I had the opportunity to meet wonderful people. From colleagues from MEFT and from other (not so interesting) degrees, to inspiring professors with a sharp sense of humor, all of them have contributed to turn my academic life so joyful and full of nostalgic memories I will keep with me until I can. I am in debt to all the colleagues I was lucky to befriend, as I will not be able to reciprocate all the help and encouragement they gave me throughout these years.

I also wish to thank my family, for the unconditional love and support they give me since I can remember.

Resumo

Esta tese investiga a combinação de dois tópicos - transporte eléctrico e sistemas periódicos no tempo (de Floquet) topológicos - que têm atraído a atenção da comunidade científica nas últimas décadas. Especificamente, estudamos o papel que a topologia desempenha nas propriedades de transporte em sistemas de Floquet unidimensionais. Isto leva-nos naturalmente à investigação do papel das simetrias no bombeamento de carga e calor.

Considera-se uma cadeia de Su-Schrieffer-Heeger (SSH) guiada. Viu-se que a corrente média como função da amplitude da oscilação é monótona na fase não topológica, mas não monótona na fase topológica.

Aborda-se também transporte induzido por estados ligados, monitorizando os picos de transmissão quando os potenciais químicos se situam dentro do hiato de energia em cadeias heterogéneas. O aumento no número de estados localizados favorece a conductância devido ao tunelamento electrónico através desses estados.

Por fim, investiga-se o bombeamento de carga e calor em dois modelos pertencentes à classe de simetria BDI. A presença da simetria partícula-lacuna (PHS) implica que a carga (o calor) seja uma função ímpar (par) do potencial químico. Isto ocorre se a simetria espacial (PS) for quebrada. Se a PHS é quebrada, o produto de PHS por PS produz bombeamento de carga/calor par/ímpar. Uma simetria adicional semelhante à PHS, embora não a usual, é introduzida, que explica que o bombeamento de carga/calor seja uma função ímpar/par. Estes resultados constituem um critério simples de inverter (ou manter) o sentido do fluxo de carga ou calor.

Palavras-chave: Sistemas de Floquet, Isolante topológico, Transporte, Simetrias

Abstract

This thesis investigates the interplay between two topics - electrical transport and driving-induced (Floquet) topological systems - that have been drawing the attention of the scientific community in the last decades. Specifically, we study the role of topology on the transport properties of one-dimensional Floquet systems. This naturally leads us to investigate the role of symmetries on charge and heat pumping.

We consider a driven Su-Schrieffer-Heeger (SSH) chain. The average current as a function of the oscillation amplitude was found to be monotonic in the non-topological phase whereas in the topological phase it is non-monotonic.

We also address bound-state-induced transport by monitoring the transmission peaks when the chemical potentials lie inside the energy gap in an inhomogeneous setup. The increase in the number of localized states enhances the conductance due to electronic tunneling through those states.

Finally, we investigate charge and heat pumping in two models belonging to the BDI symmetry class. The presence of particle-hole symmetry (PHS) implies that the pumped charge (heat) is an odd (even) function of the chemical potential. This occurs if spatial symmetry (PS) is broken. If PHS is broken, the product of PHS with PS produces even/odd charge/heat pumping. An additional symmetry that behaves like a PHS, although not the usual one, is introduced, which renders the pumped charge/heat an odd/even function. Our results provide a simple criterion for reversing (or maintaining) the direction of the charge or heat flux.

Keywords: Floquet Systems, Topological Insulator, Transport, Symmetries

Contents

List of Tables

List of Figures

Chapter 1

Introduction

One goal of Condensed Matter Physics is to classify the states of matter according to the properties of the system. Usually we are taught that matter can be found in three phases: gas, solid and liquid. Eventually we are told about the plasma state. However, this picture is a little bit reductive. In fact, there are many more states of matter that can be identified, such as superfluids, superconductors, liquid crystals or the Bose-Einstein condensate.

In fact, the 2016th Nobel Prize in Physics was awarded to the scientists David Thouless, Duncan Haldane and J. Michael Kosterlitz for theoretical discoveries of topological phase transitions and topological phases of matter, which can be found in topological insulators. While topological insulators in equilibrium are well established, the same can not be said about their non-equilibrium counterparts, object of current and active research.

Periodic driving of a topologically trivial system can render it topological [1], providing an alternative route to synthesize and manipulate topological nontrivial materials. However, with periodic driving the notion of Fermi energy can no longer be used to determine the occupation number of the eigenmodes and the nature of the quantum states differs from that of static systems. This is because when isolated, the system's dynamics strongly depends on its initial condition while for open systems the assimptotic long time dynamics is dictated by their environment. To model this effect several works [2, 3] consider electron-phonon interactions as a mean to thermalize the recurrent state. In this work we consider instead that the main thermalization mechanism is due to the contact with metallic leads used to probe the system's transport properties.

1.1 State of the art

Topological phases of matter have captured the scientific community's attention for a long time. Topological insulators have been realized in experiments [4], one example being HgTe/CdTe quantum-wells [5] , providing evidence for the quantum spin Hall effect. Other works searched for the quantized anomalous Hall (QAH) effect in tetradymite semiconductors Bi_2Te_3, Bi_2Se_3, and Sb_2Te_3 doped with transition metal elements (Cr or Fe) [6], which are known to be topological insulators. In QAH insulators spontaneous

magnetic moments and spin-orbit coupling combine to give rise to a topologically non-trivial electronic structure characterized by a finite Chern number, leading to the quantized Hall effect without any external magnetic field. The observation of the QAH effect has already been reported [7]. However, the choice of materials that exhibit these unique topological properties remains rather scarce. Thus new methods to achieve and control topological structures at will would be of great importance.

Fortunately, external periodic driving opens a route to engineer that kind of topological materials from materials that are topologically trivial in equilibrium. The materials that display topological properties under periodic driving are usually called Floquet topological insulators (FTIs) [8].

One example is a graphene ribbon attached to two electrodes (one in each edge) and irradiated by circularly polarized light as described in a work of T. Oka and H. Aoki [9]. They show how the opening of a gap in the Dirac cone may induce a dc Hall current when the electrodes are submitted to a finite dc bias. Moreover, we can find in the literature reports of experimental realizations involving graphene, namely in Ref. [10], where the driving induces the Haldane model [11]. To reproduce it, both time-reversal and parity symmetries must be broken. The time-reversal symmetry (TRS) was broken by introducing complex next-nearest-neighbours hopping amplitudes. That was accomplished by ultracold atoms in optical lattices periodically modulated in time. To break parity symmetry (PS), an energy offset between neighbouring sites was created.

However, there is one crucial question that needs to be addressed: what are the properties of the steady-state the system evolves to? In closed systems, the fate of the system is determined by the initial conditions, while for open systems the steady-state is fully determined by the system's environment. In the work [3] by Thomas Iadecola *et al.*, the system considered is composed by a graphene sheet coupled to a heat bath of acoustic phonons, with a periodically driven mass term. They take the acoustic phonons to constitute a heat bath which allows the fermions to achieve a steady state in the presence of the time dependent mass term. Floquet theory is applicable, since the time-dependence is periodic. The authors solve numerically the Floquet equation just as described in the next chapter. The authors present also an alternative to the Floquet theory, by mapping the time dependent Hamiltonian to a time independent one by making a gauge transformation. Other work in which the dissipation mechanism is done through electron-phonon interactions is the work [2] by Esin *et al.*, where the main goal is to obtain the steady-state population of the dynamically induced edge-states. At first, they make a phenomenological approach by writting rate equations for the density of excited electrons in the upper bulk Floquet band and for the density of excited particles above the Fermi level of the ideal FTI ($\varepsilon = 0$) on the right edge, considering several processes such as excitations from the lower to the upper bulk Floquet band mediated by radiative recombination, relaxation to the lower Floquet band (mediated by phonons), transitions between the bulk and the edge (also mediated by phonons) and within the edge. Next they do a microscopic analysis of the steady-state following a Floquet-Boltzmann approach, considering all kinds of scattering processes. They were able to conclude that the topological properties of the band structures of FTIs, and in particular the existence of edge states, can be manifested in an experimentally accessible transport measurement.

Transport along one dimensional driven systems has been studied by P. Hänggi *et al.* in Ref. [12],

where a Floquet Green function approach was adopted to compute the average charge current through a driven chain with each end in contact with a lead. The work of P. Hänggi *et al.* represented a step forward in the moddeling of open Floquet systems. In Ref. [12] and in this project the thermalization mechanism is due to the contact with two leads, one coupled to each end site, contrasting with the examples outlined in the previous paragraph.

Transport properties of Floquet topological phases in one dimension has been reported by O. Balabanov and H. Johannesson in [13]. Predictions for transmission spectra are presented. Namely, peaks in the transmission spectra that lie in the gaps whenever the system is in a topological phase are observed. The height of the peaks depends non-monotonically with the chain size. In this work we extend that type of analysis to non-homogeneous chains, with two portions of the chain being driven with different amplitudes.

There are other observables that encode topological features. One example is the photocurrent $I(k_x, k_y, \omega)$ which is measured in angle-resolved photoemission spectroscopy [14] (ARPES) methods. A. Farrel *et al* in Ref. [15] tried to understand the behavior of a graphene irradiated with linearly and circularly polarized light in the presence of a non-periodic and subbandwidth external perturbation while probing the system continuously over time. To do that experimentally, the technology they propose is the (ARPES), where the key measured quantity is the photocurrent. Linearly polarized light induces the creation of side bands (Dirac cones). For the electric field along the x axis, the shape of the dirac cones in the plot of $I(k_x, 0, \omega)$ versus k_x remain the same. In the plot of $I(0, k_y, \omega)$ versus k_y a gap opens at each side band. For circularly polarized light a Dirac point only splits into two copies of side bands (the plots of $I(k_x, 0, \omega)$ and $I(0, k_y, \omega)$ are similar).

In the context of quantum charge pumping, symmetries play a huge role. Earlier works [16–18] suggested that at least two parameters should have time-dependence to have a pumped current. L. Torres in [19] explains that the lack of attention given to mono-parametric pumps is based in the fact that no pumping can be obtained in the low frequency regime up to first order in the driving parameter. Hence, obtaining a nontrivial result requires going beyond the adiabatic limit described by the standard parametric pumping theory as put forward by P. W. Brouwer in [16]. The model considered by L. Torres in [19] is an open ring with a dot embedded in one of its arms. L. Torres shows that a cyclic driving of the dot levels by a single parameter leads to a pumped current when a static magnetic flux is simultaneously applied to the ring. M. Moskalets and M. Büttiker in [20] develop a Floquet scattering theory for quantum-mechanical pumping in mesoscopic conductors that goes beyond the adiabatic regime. Then the formalism developed is applied to an exactly solvable example, which is an oscillating double barrier. What both L. Torres and M. Büttiker point out is that to obtain a pumped current the left-right symmetry of the system must be broken. So symmetries play a big role in charge pumping, as we shall see later in this work. Furthermore, L. Torres in [19] establishes a criterion for the inversion of the charge flow, which is the reversal of the direction of the magnetic field, while M. Büttiker establishes that the charge flow is reversed in the large frequencies limit by tuning the frequency of the oscillation to the level spacing in the sample. In this work we will see another way to reverse the charge or heat flows.

1.2 Objectives and Outline

In this work the main goal is to establish transport properties of Floquet topological phases in one dimension. For that we compute the average current for one model and the transmission spectra for different topological phases of another model. We study the implications symmetries have on the charge pumping for two distinct models as well. The tools acquired also allow for the study of the heat pumping for the models already considered in the charge pumping.

This thesis is organized as follows. In Chapter 2 we introduce the Floquet formalism which provides the tools needed to deal with periodically driven systems. In Chapter 3 we consider Floquet topological insulators, by introducing first the equilibrium case and only then the out of equilibrium case. We introduce a model which is a variant of a driven SSH model and take considerations on inhomogeneous chains of that model. In Chapter 4 we give an introduction to electrical transport. First we refer to the static Landauer-Büttiker formalism and then move on to the Floquet non-equilibrium Green function formalism, explaining how to compute the average current. In Chapter 5 we present the main results of this work. First we study the effect topology has on the transport by using two variants of a driven SSH chain. Then we study the odd/even behavior of the charge pumping as a function of the chemical potential, and explain that behavior by analysing the symmetries present. We end with the study of the total heat and the heat pumping using models already introduced. In Chapter 6 we take our conclusions and suggest future work. In Appendix A we do the Fourier transform of one of the models considered. In Appendix B we show the phase diagram of a variant of a driven SSH model already introduced in Chapter 3. Finally, in Appendix C we present a discussion of the symmetry properties of the Floquet scattering matrix in general terms.

Chapter 2

Time-periodic quantum systems

The goal of this chapter is to introduce the tools available to describe quantum systems periodic in time, needed later on in this work. Although some time-independent quantum systems can be described exactly, the same can not be said about time-dependent ones. The general time-dependent case is not exactly solvable, so we must resort to approximation methods such as time-dependent perturbation theory, the magnus expansion or the adiabatic approximation.

In this work we are interested only in time-periodic systems in particular. This interest is justified, since time-periodic perturbations are the most implemented ones in experiments. That can be achieved by irradiating a static system of interest, like graphene. Fortunately, we can make use of the Floquet formalism, which is based in an exact result called Floquet's theorem, valid for any time-periodic quantum system. In this chapter we start with the foundations of quantum mechanics, particularizing for time-independent systems. Then, we narrow down the time-dependent case to the time-periodic one. The Floquet's theorem and its implications are enunciated. Afterwards, systems that enjoy discrete spatial invariance are discussed. Furthermore, we give an outline of how to solve the time-dependent Schrödinger equation for a time-periodic Hamiltonian. At the end we address open quantum systems, as it will be necessary in subsequent chapters.

2.1 The Schrödinger equation

According to the basic postulates of quantum mechanics, a state in which a quantum system can be found at a given instant t is represented by a vector $|\psi(t)\rangle$, referred to state-vector, or simply state, living in a Hilbert space $\mathcal{H}$, where an inner product $\langle\psi'|\psi\rangle$ is defined. The time-evolution of the system is governed by the time-dependent Schrödinger equation (TDSE)

$$i\hbar\partial_t |\Psi(t)\rangle = \hat{H}(t) |\Psi(t)\rangle \ , \tag{2.1}$$

with initial condition $|\Psi(0)\rangle$. In (2.1), $\hbar$ is the Planck's constant (divided by 2π), and $\hat{H}(t)$ is the Hamiltonian operator of the system[1].

[1] The hat means that we are dealing with an operator. We will keep it for now.

If the Hamiltonian is time-independent, or more briefly, static, we can resort to separation of variables in (2.1), and arrive at the time-independent Schrödinger equation (TISE) for a time-independent state $|\psi\rangle$

$$\hat{H}|\psi\rangle = E|\psi\rangle\,, \tag{2.2}$$

which can be seen as an eigenvalue equation. The set of the solutions of this equation, $\{|\psi_n\rangle\}$, are the eigenvectors, or eigenstates, of the Hamiltonian. Since time-dependence was eliminated, these states, not being dynamical, are said to be stationary. An eigenvalue, E_n, is associated to each eigenstate. These eigenvalues are interpreted as energies, so they are commonly mentioned as eigenenergies. The set of all eigenenergies $\{E_n\}$ composes the spectrum of the Hamiltonian. Eigenstates with the same energy are called degenerate. We further assume that the set $\{|\psi_n\rangle\}$ is complete, in the sense that any state can be written as a linear combination of states in that set. As such, the set $\{|\psi_n\rangle\}$ forms a basis for the Hilbert space. If the set $\{|\psi_n\rangle\}$ is not orthonormalized, we could apply a procedure to orthonormalize it[2]. So, without loss of generality, we assume

$$\langle\psi_m|\psi_n\rangle = \delta_{m,n}\,. \tag{2.3}$$

Once we find both the eigenvectors and eigenvalues of the Hamiltonian, we can write its spectral decomposition

$$\hat{H} = \sum_{\alpha} E_\alpha |\psi_\alpha\rangle\langle\psi_\alpha|\,. \tag{2.4}$$

Thus we say that the Hamiltonian is diagonal in the basis $\{|\psi_\alpha\rangle\}$, since the matrix elements are of the form $\langle\psi_\beta|\hat{H}|\psi_\alpha\rangle = E_\alpha\delta_{\alpha,\beta}$.

In general the index α might represent a set of quantum numbers that are needed to fully specify the state of the system, according to the degrees of freedom of the one-particle system. If the Hamiltonian is diagonal in the basis $\{|\psi_\alpha\rangle\}$, as in (2.4), we say that α is a good quantum number (for the Hamiltonian). The set $\{E_\alpha, |\psi_\alpha\rangle\}$ solves the TISE, but recall that we want to solve the time-dependent one. To construct the general solution of (2.1), we integrate it to find the dynamical state $|\Psi(t)\rangle$, given the initial condition $|\Psi(0)\rangle$:

$$|\Psi(t)\rangle = e^{-i\hat{H}t/\hbar}|\Psi(0)\rangle\,. \tag{2.5}$$

Now we impose the initial condition $|\Psi(0)\rangle = |\psi_\alpha\rangle$. In that case, we have

$$|\Psi_\alpha(t)\rangle = e^{-iE_\alpha t/\hbar}|\psi_\alpha\rangle\,. \tag{2.6}$$

As (2.1) is a linear equation, its general solution, with initial condition $|\Psi(0)\rangle$, is

[2]For example, using the Gram-Schmidt process.

$$|\Psi(t)\rangle = \sum_{\alpha} c_\alpha e^{-iE_\alpha t/\hbar}|\psi_\alpha\rangle\,, \tag{2.7}$$

where $c_\alpha = \langle\psi_\alpha|\Psi(0)\rangle$ are complex numbers.

If the Hamiltonian is time-dependent, in general we can not find an analytical solution for the TDSE. The best we can do for the general case is to write a formal solution for (2.1). This solution is obtained in terms of the time-evolution operator, which is defined through

$$|\Psi(t)\rangle = \hat{U}(t,t_0)|\Psi(t_0)\rangle\,. \tag{2.8}$$

What this operator does is propagate in time the state of the system. From the previous equation, we can see directly that $\hat{U}(t,t) = \mathbb{1}$[3] must be satisfied. Other property we can infer from (2.8) is

$$\hat{U}(t,t_1)\hat{U}(t_1,t') = \hat{U}(t,t'), \forall t_1,t',t\,. \tag{2.9}$$

If in (2.1) we insert $|\Psi(t)\rangle$ as it is written in (2.8) we obtain a partial differential equation for the time-evolution operator:

$$i\hbar\partial_t\hat{U}(t,t_0) = \hat{H}(t)\hat{U}(t,t_0)\,, \tag{2.10}$$

with initial condition $\hat{U}(t_0,t_0) = \mathbb{1}$. The problem is now to find a solution for this equation given $\hat{H}(t)$. For that we write from the equation above the equivalent integral equation (dropping the hats)

$$U(t,t_0) = \mathbb{1} - \frac{i}{\hbar}\int_{t_0}^{t} H(t')U(t',t_0)\,\mathrm{d}t'\,. \tag{2.11}$$

The problem is not solved yet, since the time-evolution operator appears in both hand sides of (2.11). To solve for $U(t,t_0)$ we follow an iterative process[4] in which we compute a sequence of operators $\{U_n(t,t_0)\}$ that verify the recursive relation

$$U_{n+1}(t,t_0) = U_0 - \frac{i}{\hbar}\int_{t_0}^{t} H(t')U_n(t',t_0)\,\mathrm{d}t'\,, \tag{2.12}$$

where $U_0 = \mathbb{1}$. By computing successive terms of the sequence we arrive at a series for the time-evolution operator, known as Dyson series, and it writes

$$U(t,t_0) = \mathbb{1} + \sum_{n=1}^{\infty}\left(-\frac{i}{\hbar}\right)^n \int_{t_0}^{t}\mathrm{d}t_1\int_{t_0}^{t_1}\mathrm{d}t_2 ... \int_{t_0}^{t_{n-1}}\mathrm{d}t_n\; H(t_1)H(t_2)...H(t_n)\,. \tag{2.13}$$

This result is commonly used in time-dependent perturbation theory, upon truncation of the series. As the reader may notice, only one integration has the time t as upper limit. It would be more enlightening if all integrations were over the full interval from t_0 to t. That can be done using the concept of time-ordering product. The time-ordering product of a set of time-dependent operators,

[3] $\mathbb{1}$ denotes the identity operator on $\mathcal{H}$.
[4] This process is identical to Picard iterative process in Mathematics.

$$\mathbb{T}[O_1(t_1)O_2(t_2)...O_n(t_n)]\,, \tag{2.14}$$

is a permutation of the factors such that latter times appear at the left of former times. The symbol $\mathbb{T}$ can be interpreted as an operator, called time-ordering operator. It can be shown that the Dyson series can be rewritten as

$$U(t,t_0) = \mathbb{1} + \sum_{n=1}^{\infty} \frac{1}{n!} \left(-\frac{i}{\hbar}\right)^n \int_{t_0}^{t} \mathrm{d}t_1 \int_{t_0}^{t} \mathrm{d}t_2 ... \int_{t_0}^{t} \mathrm{d}t_n \; \mathbb{T}[H(t_1)H(t_2)...H(t_n)]\,, \tag{2.15}$$

which is commonly abbreviated as

$$U(t,t_0) = \mathbb{T} e^{-\frac{i}{\hbar}\int_{t_0}^{t} H(t')\;\mathrm{d}t'}\,. \tag{2.16}$$

The solution of (2.1) follows from applying (2.16) to $|\Psi(0)\rangle$, as in (2.8). In the case the Hamiltonian commutes with itself at different times, the time-ordering in (2.15) has no effect and (2.16) reduces to

$$U(t,t_0) = e^{-\frac{i}{\hbar}\int_{t_0}^{t} H(t')\;\mathrm{d}t'}\,. \tag{2.17}$$

If additionally the Hamiltonian is time-independent we end up with

$$U(t,t_0) = U(t-t_0) = e^{-\frac{i}{\hbar}H(t-t_0)}\,, \tag{2.18}$$

similarly to what appeared in (2.5).

From a numerical point of view, (2.16) is not particularly useful, so we need an alternative expression for the time-evolution operator. It can be shown that for a small enough time interval δt the following relation holds

$$U(t+\delta t,t) \approx e^{-\frac{i}{\hbar}H(t)\delta t} + \mathcal{O}((\delta t)^2)\,, \tag{2.19}$$

where we discarded terms of higher order. Dividing the time interval from t_0 to t in N slices of length $\Delta t = (t-t_0)/N$ and applying (2.9) several times we have a numerical expression for $U(t,t_0)$:

$$U(t,t_0) \approx \prod_{n=0}^{N} e^{-\frac{i}{\hbar}H(t_n)\Delta t},\; t_n = t_0 + n\Delta t\,, \tag{2.20}$$

with later times appearing at the left.

In general, due to the hermiticity of the Hamiltonian ($H = H^\dagger$), the time-evolution operator is unitary, that is, $U^{-1}(t,t') = U^\dagger(t,t')$. For a generic unitary operator, it can be shown that its spectrum is a subset of the unit circle in the complex plane.

Even if the time-dependent case is more complicated and in general non-solvable analytically, we can do more in the case where the system has discrete translational invariance in time, that is, the Hamiltonian is periodic in time, with no trivial dependence. That will be the subject of the next section.

2.2 Periodically driven systems

Before studying transport along time-periodic systems, we need to understand first the fundamental concepts inherent to this type of systems. As such, the tools developed in this section will be fundamental throughout this work. We consider a time-periodic system to be a system whose time-evolution is dictated by an Hamiltonian, acting on $\mathcal{H}$, periodic in time with period T. That is, for any instant of time t, the following is satisfied:

$$H(t) = H(t+T)\,, \tag{2.21}$$

This kind of systems can be created through an external driving field (which could be, for example, electromagnetic [1, 12]). The central result common to all periodically-driven systems is the Floquet's theorem[5], which we will enunciate now.

2.2.1 Floquet's theorem and Floquet's equation

The Floquet's theorem states that for any time-periodic Hamiltonian of period T there exists a complete set of vectors $\{|\psi_\alpha(t)\rangle\}$ of the form

$$|\psi_\alpha(t)\rangle = e^{-i\epsilon_\alpha t/\hbar}|u_\alpha(t)\rangle\,, \tag{2.22}$$

which verify the TDSE, where the vectors $|u_\alpha(t)\rangle$ are time-periodic with period T, and the scalars ϵ_α are real numbers. The states $|\psi_\alpha(t)\rangle$ are called Floquet states or Floquet modes, and the vectors $|u_\alpha(t)\rangle$ Floquet functions.

The Floquet's theorem ensures that any solution of the TDSE can be written in the form

$$|\Psi(t)\rangle = \sum_\alpha c_\alpha e^{-i\epsilon_\alpha t/\hbar}|u_\alpha(t)\rangle\,, \tag{2.23}$$

with the coefficients c_α not depending on time, assuming without loss of generality that the set $\{|\psi_\alpha(t)\rangle\}$ is normalized and orthogonal at equal times. You can notice that (2.23) resembles expression (2.7). The phases ϵ_α are mentioned as quasienergies. As the complex exponential function is periodic, these quasienergies are defined up to an integer multiple of $\hbar 2\pi/T \equiv \hbar\Omega$, where we defined the driving frequency $\Omega = 2\pi/T$. Something similar happens with quasimomentum of a particle in a crystal, where the momentum is defined up to an integer multiple of the reciprocal lattice vector. Any momentum falling outside the first Brillouin zone of the reciprocal lattice is redundant. Thus we refer to momentum as quasimomentum (in this work we will interchange the terms momentum and quasimomentum). In one dimension, the first Brillouin zone is the interval $]-\pi/a, \pi/a]$ (a is the unit cell size). Similarly, we define the first Floquet zone, or just Floquet zone, to be the interval $]-\hbar\Omega/2, \hbar\Omega/2]$.

The ambiguity in the quasienergies can be expressed through a gauge transformation. If we plug the state (2.22) in the TDSE, an equation for the Floquet function is obtained,

[5] For a proof of this theorem see [21].

$$[H(t) - i\hbar\partial_t]\,|u_\alpha(t)\rangle = \epsilon_\alpha\,|u_\alpha(t)\rangle\ , \tag{2.24}$$

called Floquet's equation. It is easy to see that the equation above is invariant under the gauge transformation

$$\epsilon_\alpha \to \epsilon_\alpha + m\hbar\omega,\ \ |u_\alpha(t)\rangle \to e^{im\omega t}\,|u_\alpha(t)\rangle\ , \tag{2.25}$$

for any integer m. This reinforces the fact that the quasienergies come in classes of equivalent representatives, from which we choose a representative of the class. We can see (2.24) as an eigenvector equation, but now on the extended Hilbert space $L_2[0,T]\otimes\mathcal{H}$, where $L_2[0,T]$ is the Hilbert space of periodic functions with period T, and $\mathcal{H}$ the usual space $H(t)$ acts on. The operator in the left-hand side of (2.24) which acts on the extended Hilbert space is usually called Floquet Hamiltonian. We will refer to it using the symbol $\mathbb{K}$. At this stage, the time parameter t is treated in the same footing as x, that is, it is considered as an additional coordinate or dimension. To give technical meaning to the extended Hilbert space picture, the inner product defined in this space is the following:

$$\langle\langle u'|u\rangle\rangle = \frac{1}{T}\int_0^T \langle u'|u\rangle\ \mathrm{d}t\,, \tag{2.26}$$

where $|u\rangle\rangle$ denotes a state belonging to $L_2[0,T]\otimes\mathcal{H}$.

The extended Hilbert space formalism can be useful to do a rigorous mathematical analysis of periodically time-dependent quantum systems, as pointed out in [21]. However, we will not explore the subject, as the key point to retain is that we end up with an eigenvector problem to solve.

2.2.2 Effective Hamiltonian and rotating frame

Now we ask: is there a static Hamiltonian whose eigenenergies are the quasienergies ϵ_α? The answer is yes. To see that we pick a certain Floquet state at $t=0$ and propagate it to $t=T$. We have

$$U(T,0)|\psi_\alpha(0)\rangle = |\psi_\alpha(T)\rangle \Leftrightarrow U(T,0)|u_\alpha(0)\rangle = e^{-i\epsilon_\alpha T/\hbar}|u_\alpha(T)\rangle = e^{-i\epsilon_\alpha T/\hbar}|u_\alpha(0)\rangle\,. \tag{2.27}$$

So, the spectrum of the operator $U(T,0)\equiv U(T)$, which we will call Floquet operator from now on, is the set $\{e^{-i\epsilon_\alpha T/\hbar}\}$, which is a subset of the unit circle (the quasienergies are real). The quasienergies are obtained by taking the logarithm. The Brillouin zone structure of the quasienergy spectrum is kept since the complex logarithm is a multi-valued function. The static effective Hamiltonian whose eigenenergies coincide with the quasienergies can be defined through

$$U(T) = e^{-iH_{\text{eff}}T/\hbar}\,. \tag{2.28}$$

If we compute also the eigenstates of the Floquet operator, labeled by $|u_\alpha\rangle$, we obtain a spectral representation for $U(T)$:

$$U(T) = \sum_{\alpha} |u_\alpha\rangle e^{-i\epsilon_\alpha T/\hbar} \langle u_\alpha| \,. \tag{2.29}$$

If we want to compute the effective Hamiltonian we need to take the logarithm of the Floquet operator. How we do that is saved for later. Another operator of interest is the one that propagates the Floquet functions $|u_\alpha(t)\rangle$ in time. We will call it periodized time-evolution operator, and it is defined by

$$V(t) \equiv U(t) e^{iH_{\text{eff}}t/\hbar} \,. \tag{2.30}$$

It is easy to show that it is time-periodic and propagates the Floquet functions.

Considering (2.29), we make the identification

$$|u_\alpha(t)\rangle = V(t)|u_\alpha\rangle \,. \tag{2.31}$$

If we apply the unitary transformation

$$|\Psi(t)\rangle = V(t)|\Phi(t)\rangle \,, \tag{2.32}$$

from the TDSE and the definition of $V(t)$, we can show that the transformed states obey

$$i\hbar\partial_t|\Phi(t)\rangle = H_{\text{eff}}|\Phi(t)\rangle \,. \tag{2.33}$$

The interesting point is that the dynamics of the transformed states is governed by the static effective Hamiltonian H_{eff}. Thus we say that we moved to the rotating frame.

2.2.3 Floquet-Bloch Hamiltonian

In the previous section we mentioned that the quasienergy spectrum has a Brillouin zone like structure, and compared quasienergy, in time-periodic systems, to quasimomentum, in space-periodic systems. This analogy comes from the similarity between the Floquet's theorem and the Bloch's theorem. We have already exploited the former, but now we will dwell on the latter[6]. The fact that the system is periodic in the real space ensures that the Hamiltonian is block diagonal in the momentum space. Hence, the states with crystal momentum $\mathbf{k}$ evolve in time according to a Hamiltonian written in momentum space, $H(\mathbf{k})$, called Bloch Hamiltonian. Thus a TISE for each $\mathbf{k}$ can be written:

$$H(\mathbf{k})\psi(\mathbf{r}) = E\psi(\mathbf{r}) \,. \tag{2.34}$$

Bloch's theorem [22] states that the eigenstates, represented by their wave function, are of the form

$$\langle \mathbf{r}|\psi_{\alpha,\mathbf{k}}\rangle \equiv \psi_{\alpha,\mathbf{k}}(\mathbf{r}) = e^{i\mathbf{k}.\mathbf{r}} u_{\alpha,\mathbf{k}}(\mathbf{r}) \,, \tag{2.35}$$

[6]To be precise, Bloch's theorem, as it is in the context of solids, is actually based on the first version of the Floquet's theorem, discovered by the mathematician Gaston Floquet, in 1883.

where $u_{\alpha,\mathbf{k}}(\mathbf{r})$ is a periodic function with the same period of the potential, called Bloch function, and $\mathbf{k}$ the crystal momentum (or quasimomentum, as we have been calling it). Making the analogy between both theorems, we identify the crystal momentum with the quasienergy, and the spatial position with the "position" in time. Each eigenstate $\psi_{\alpha,\mathbf{k}}(\mathbf{r})$ can be seen as a plane-wave modulated by the Bloch function. It is often called a Bloch wave. Each Bloch wave $\psi_{\alpha,\mathbf{k}}(\mathbf{r})$ has energy $E_\alpha(\mathbf{k})$. The index α serves to distinguish states with the same momentum, but with different Bloch functions. For a fixed α, $E_\alpha(\mathbf{k})$ varies continuously with $\mathbf{k}$, and can be interpreted as a dispersion relation. The set of energies $\{E_\alpha(\mathbf{k})\}$ for a fixed α forms an energy band, and α it's the band index. The set of all bands forms the electronic band structure of the solid[7]. The band structure and their occupation determines the transport properties of the material. The point of this section is to check if we can bring some concepts of the static case to the driven one. In fact, if both Bloch's and Floquet's theorem apply, the Hamiltonian is still diagonal in momentum space, and then we speak in a Floquet-Bloch Hamiltonian $H(\mathbf{k},t)$ periodic in time. To see how the concept of band structure can be carried over to the driven case, we write the time-evolution operator in momentum space according to (2.16)

$$U(\mathbf{k};t,t') = \mathbb{T}\exp\left[-\frac{i}{\hbar}\int_{t'}^{t} H(\mathbf{k},\tau)\,\mathrm{d}\tau\right], \tag{2.36}$$

to obtain the Floquet operator in momentum space

$$U(\mathbf{k};T,0) \equiv U(\mathbf{k},T) = \mathbb{T}\exp\left[-\frac{i}{\hbar}\int_{0}^{T} H(\mathbf{k},t')\,\mathrm{d}t'\right]. \tag{2.37}$$

As stated above, we can obtain the quasienergies $\{\epsilon_\alpha(\mathbf{k})\}$ from the eigenvalues of the Floquet operator, where α specifies the band. In the driven case, we refer to the bands as Floquet bands. Thus, the Floquet bands form an effective band structure in the same sense of the static case.

2.2.4 Frequency domain

In this section we present a method to solve (2.24). Since the Floquet functions are time-periodic, as ensured by Floquet's theorem, and the Hamiltonian is time-periodic as well, we can make the expansions in Fourier series

$$|u_\alpha(t)\rangle = \sum_n e^{-in\Omega t}\,|u_{\alpha,n}\rangle\,, \tag{2.38a}$$

$$H(t) = \sum_n h_n e^{in\Omega t}\,. \tag{2.38b}$$

Note that there are two indices, α is a quasienergy index and n is a Fourier, or sideband, index. Inserting the decompositions above in (2.24) we obtain the Floquet equation in the frequency domain

[7]The concept of energy band exists whether translational symmetry is present or not. As we are not concerned with band structures in general, the cases here discussed will suffice.

$$(\epsilon_\alpha + n\hbar\Omega)\,|u_{\alpha,n}\rangle = \sum_{m\in\mathbb{Z}} h_m\,|u_{\alpha,n+m}\rangle\ . \tag{2.39}$$

Most commonly, the Hamiltonian contains only one harmonic of the driving frequency, such that $H(t) = h_0 + h_1 e^{i\Omega t} + h_1^\dagger e^{-i\Omega t}$. If that is the case, the previous equation reads

$$\epsilon_\alpha\,|u_{\alpha,n}\rangle = (h_0 - n\hbar\omega\mathbb{1})\,|u_{\alpha,n}\rangle + h_1\,|u_{\alpha,n+1}\rangle + h_1^\dagger\,|u_{\alpha,n-1}\rangle\ , \tag{2.40}$$

The previous equation can be seen as an eigenvector problem with matrix representation

$$\underbrace{\begin{bmatrix} \ddots & h_1 & 0 & 0 & 0 & 0 & \dots \\ h_1^\dagger & h_0+2\Omega\mathbb{1} & h_1 & 0 & 0 & 0 & \dots \\ 0 & h_1^\dagger & h_0+\Omega\mathbb{1} & h_1 & 0 & 0 & \dots \\ 0 & 0 & h_1^\dagger & h_0 & h_1 & 0 & \dots \\ 0 & 0 & 0 & h_1^\dagger & h_0-\Omega\mathbb{1} & h_1 & \dots \\ 0 & 0 & 0 & 0 & h_1^\dagger & h_0-2\Omega\mathbb{1} & h_1 \\ \vdots & \vdots & \vdots & \vdots & \vdots & h_1^\dagger & \ddots \end{bmatrix}}_{\mathbb{K}} \begin{bmatrix} \vdots \\ |u_{\alpha,-2}\rangle \\ |u_{\alpha,-1}\rangle \\ |u_{\alpha,0}\rangle \\ |u_{\alpha,1}\rangle \\ |u_{\alpha,2}\rangle \\ \vdots \end{bmatrix} = \epsilon_\alpha \begin{bmatrix} \vdots \\ |u_{\alpha,-2}\rangle \\ |u_{\alpha,-1}\rangle \\ |u_{\alpha,0}\rangle \\ |u_{\alpha,1}\rangle \\ |u_{\alpha,2}\rangle \\ \vdots \end{bmatrix}\ , \tag{2.41}$$

where $\mathbb{K}$ in here is the matrix representation of the Floquet Hamiltonian in the frequency domain, which is an infinite matrix. To obtain the quasienergies and the Floquet states we need now to diagonalize it. In practice, we truncate $\mathbb{K}$ at a certain multiple of the frequency, such that the uppermost diagonal block has $m\Omega\mathbb{1}$ while the lowest has $-m\Omega\mathbb{1}$. The parameter m must be chosen upon convergence of the spectrum and eigenvectors.

2.2.5 Magnus Hamiltonian

If the energy scale $\hbar\Omega$ is much larger than every other energy present in the problem, a perturbative solution of (2.40) is justified. We assume that the n-the Fourier component of the Floquet function $|u_{\alpha,n}\rangle$ is of the order $1/(\hbar\Omega)^n$, and therefore, that the Hamiltonian has an expansion in powers of $1/(\hbar\Omega)$, called the Magnus expansion. Writing (2.40) for $n = 0, -1, 1$ and collecting terms in the same power, we arrive at

$$\epsilon_\alpha|u_{\alpha,0}\rangle = H_{\text{eff}}|u_{\alpha,0}\rangle\,, \tag{2.42}$$

where

$$H_{\text{eff}} = h_0 + \frac{1}{\hbar\Omega}[h_1, h_1^\dagger]\,, \tag{2.43}$$

is the Magnus Hamiltonian to first order. An outline for computing terms of higher order in the Magnus expansion is given in [23]. In the same reference, it is pointed out that the effective Magnus Hamiltonian is in general different than the one present in (2.30).

2.2.6 Open quantum systems

In this thesis we will deal with finite one dimensional systems tight-binding systems, as a center region, coupled to two external leads, the left one and the right one. Since following the dynamics of the states of the full system is impossible, what we do is follow the dynamics of the center region in the presence of the leads, which act as an environment. The total Hamiltonian can be partitioned in five components [24]: a first contribution from the left lead, a second from the coupling of the center region to the left lead, a third from the center region, a fourth from the coupling of the center region to the right lead and a fifth from the right lead. In symbols,

$$H = H_L + V_{LC} + H_C + V_{CR} + H_R. \tag{2.44}$$

If we write the Schrödinger equation for the system, decoupling the states of the central region from the ones of the leads, we obtain for the Hamiltonian of the center region two non-hermitian contributions called self-energies, one from the coupling to the left lead, Σ_L, and other from the coupling to the right lead, Σ_R. Equation (2.1) reads

$$i\hbar\partial_t \left|\Psi(t)\right\rangle = \left[H(t) + \Sigma_L + \Sigma_R\right] \left|\Psi(t)\right\rangle\,. \tag{2.45}$$

Floquet's theorem is still applicable, and the Floquet equation reads

$$[H(t) + \Sigma_L + \Sigma_R - i\hbar\partial_t]|u_\alpha(t)\rangle = \bar{\epsilon}_\alpha|u_\alpha(t)\rangle\,. \tag{2.46}$$

The bar over the quasienergy denotes that it is complex. As the Hamiltonian operator is non-hermitian, the eigenstates of the Floquet Hamiltonian are not mutually orthogonal anymore. Therefore, we need to solve (2.46) for the left eigenstates in addition to the usual ones, that is, solve the adjoint equation

$$\left[H(t) + \Sigma_R^\dagger + \Sigma_L^\dagger - i\hbar\partial_t\right] |u_\alpha^+(t)\rangle = \bar{\epsilon}_\alpha^*|u_\alpha^+(t)\rangle\,. \tag{2.47}$$

In practice, this means we need to diagonalize both $\mathbb{K}$ and $\mathbb{K}^\mathsf{T}$. In this way, the Floquet functions form a bi-orthogonal basis at equal times,

$$\langle u_\alpha^+(t)|u_\beta(t)\rangle = \delta_{\alpha\beta} \text{ and } \sum_\alpha |u_\alpha^+(t)\rangle\langle u_\alpha(t)| = 1\,. \tag{2.48}$$

We can write a spectral decomposition for the time-evolution operator at two distinct times given by

$$U(t,t') = \sum_{\alpha} e^{-i\bar{\epsilon}_\alpha (t-t')/\hbar} |u_\alpha(t)\rangle\langle u_\alpha^+(t')| \,, \tag{2.49}$$

where the sum is over all states within one Floquet zone.

Chapter 3

Floquet topological insulators

In this chapter the topic of Floquet topological insulators is introduced. Topological insulators are materials that have peculiar electrical conduction properties compared to conventional conductors, insulators and semiconductors. Topological insulators block the flow of current in the bulk, behaving as conventional insulators in that sense, but conduct electrons on their edges or surfaces through localized states. These states, whose presence is determined solely by bulk properties of the system, are immune to small perturbations that do not close the spectral gap, such as back-scattering induced by impurities, allowing for non-dissipative electronic transport. These unusual properties make topological insulators promising in respect to applications in high-performance electronics and quantum computing. However, reproducing topologically non-trivial materials requires careful band-structure engineering and high degree of sample control. Fortunately, external periodic driving opens a route to engineer topological materials with high tunability from materials that are topologically trivial in equilibrium. Topological materials obtained by this via are called Floquet topological insulators, the key topic of this chapter.

3.1 Topological insulators

Before diving in the subject of Floquet topological insulators, it is instructive to first consider topological insulators in equilibrium. In general, topological insulators are non-interacting systems with fully filled bands and gapped in bulk, but host gapless boundary modes. Although being insulators in bulk, the boundaries of these systems have a metallic behaviour, conducting electricity through the surface or edge states. These states are topologically protected. This means that they remain present under arbitrary deformations of the Hamiltonian, as long as the gap remains open.

The first phenomenon that has topological features to be discovered was the integer quantum Hall effect. The Hall effect is verified when we apply a static electric field along a material and then apply a static magnetic field perpendicular to the plane of the material (let us consider a bidimensional one). The Hall effect is thus the appearance of a conductivity (the Hall conductivity) transverse to the electric field along the material. Classical physics predicts that the conductivity grows linearly with increasing magnetic field. However, measurements for a silicon metal-oxide-semiconductor field-effect transistor,

in an experiment held by the physicist Klaus von Klitzing in 1980 [25], revealed that the resistivity varies in discrete jumps of h/e^2, for high magnetic fields, at low temperatures. This result is depicted in the figure below.

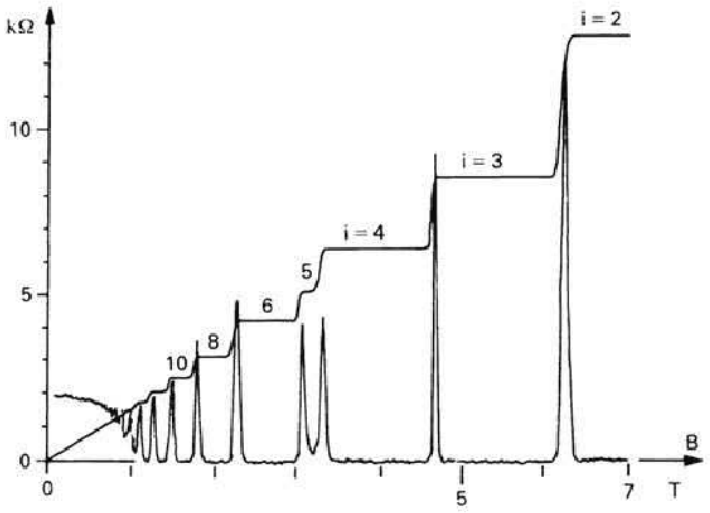

Figure 3.1: Vertical axis: Hall resistivity ρ_{xy} (plateaus) and longitudinal resistivity ρ_{xx} (peaks) in a 2D electron gas, as a function of the applied magnetic field.

This effect was considered revolutionary, once it allowed for a very high precision measurement of the fine structure constant. It can only be explained in the light of quantum mechanics, so it became famous with the name of quantum Hall effect. Thanks to this discovery, von Klitzing was awarded with the 1985 Nobel Prize in Physics. The plot in Fig. 3.1 tells us that the conductivity is given by

$$\sigma_{xy} = \frac{e^2}{h} n, \tag{3.1}$$

where n is an integer, and the pre-factor e^2/h can be interpreted as a conductance quantum. The effect discovered by von Klitzing is the nowadays called integer quantum Hall effect, and it is observed if electron-electron interactions are weak. Electron-electron interactions give place to the fractional quantum Hall effect, where n is a rational number. The integer n is intimately related to the topology of the bands. It can be proved [26] that the Hall conductivity is given by the TKNN formula (named after Thouless, Kohomoto, Nightingale and den Nijs)

$$\sigma_{xy} = \frac{e^2}{h} \sum_{\alpha} C_\alpha, \tag{3.2}$$

where the sum is over all filled bands α and C_α is the Chern number associated to that band. The Chern number is a quantity that cannot change upon continuous deformations of the Hamiltonian that keep the gap open. It is thus called a topological invariant. There are models that have a non-vanishing Chern number without the need of external magnetic fields. Those models with filled bands are called Chern insulators. The condition for a non-trivial Chern number is the breaking of the time-reversal symmetry, as defined in (3.3). Insulators which host gapless edge or surface states but without time-reversal symmetry breaking are called topological insulators. The first topological insulator to be introduced was the $\mathbb{Z}_2$

topological insulator by Kane and Mele [27]. Nonetheless, soon it was realised that other symmetries play a significant role in the topological protection of boundary states, and other topological invariants exist besides the $\mathbb{Z}_2$. The classification of the topological invariant is based on the symmetries that are present and the dimension of the system. As such, symmetries will be rather important throughout this work. The classification of topological insulators is the subject of the next subsection.

3.1.1 Symmetry classes

The concept of symmetry is ubiquitous in all subfields of Physics. It reveals itself to be more prominent in condensed matter and high-energy physics. Although the symmetries we are going to study here appear frequently in the context of particle physics, we will adapt the language to condensed matter. Symmetries have many mathematical formulations. Here we will follow a simple formulation in terms of operators, and avoid the discussion of their mathematical foundations, such as groups. The operators implement symmetry transformations, and symmetry is seen as a manifestation of invariance under those transformations. We can classify symmetries as continuous or discrete. Examples of the former are the (continuous) time-translation and (continuous) spatial-translation symmetries. As examples of the latter, we have spatial inversion (or parity) symmetry (PS), time-reversal symmetry (TRS), particle-hole symmetry (PHS) and chiral symmetry (CS). The last three symmetries are the ones of interest in what respects the protection of edge states, so in this subsection we will explore these ones in particular. Additionally, we will consider only one dimensional systems with (discrete) spatial translation invariance. The three symmetries are defined as

- Time-reversal symmetry: there exists an unitary matrix T such that

$$TH^{\mathsf{T}}(-\mathbf{k})T^{\dagger} = H(\mathbf{k})\,; \tag{3.3}$$

- Particle-hole symmetry: there exists an unitary matrix C such that

$$CH^{*}(\mathbf{k})C^{\dagger} = -H(-\mathbf{k})\,; \tag{3.4}$$

- Chiral symmetry: there exists an unitary matrix Γ such that

$$\Gamma H(\mathbf{k})\Gamma^{\dagger} = -H(\mathbf{k})\,. \tag{3.5}$$

For Hermitian Hamiltonians, TRS as per (3.3) is equivalent to the more frequent definition with complex conjugation instead of the transpose of the Hamiltonian. For non-hermitian Hamiltonians this is not true anymore. There is TRS and TRS†. TRS as defined in (3.3) is in fact TRS† according to K. Kawabata *et al.* [28]. The same goes for PHS and CS. We will make an abuse of notation and refer to these symmetries without the dagger.

Note that the three symmetries are not independent. For instance, let us assume the system has both TRS and PHS. Then

$$
\begin{aligned}
H(\mathbf{k}) &= -CH^{\mathsf{T}}(-\mathbf{k})C^{\dagger} = \\
&= -CT^{\dagger}TH^{\mathsf{T}}(-\mathbf{k})T^{\dagger}TC^{\dagger} = \\
&= -CT^{\dagger}H(\mathbf{k})TC^{\dagger} = -(TC^{\dagger})^{\dagger}H(\mathbf{k})(TC^{\dagger})\,,
\end{aligned}
\tag{3.6}
$$

so it has CS as well, with $\Gamma = TC^{\dagger}$. Whenever a Hamiltonian has TRS, one can have either $T^{*}T = +\mathbb{1}$ or $T^{*}T = -\mathbb{1}$. The same goes for PHS, i.e., we have two possibilities for the product $C^{*}C$. So, when both TRS and PHS are present, CS is present as well, and this happens with four possibilities (4). When there is only TRS, we have two possibilities (2). When there is only PHS, we have two more possibilities (2). It can also happen that the Hamiltonian has CS having neither TRS nor PHS (1). It might also happen that the Hamiltonian has none of these three symmetries (1). So we have 4+2+2+1+1=10 cases in total. At the end, any Hamiltonian falls in one of these cases. Each case is called a symmetry class. The symmetry class the Hamiltonian belongs to and the dimension of the system define the kind of topological invariant the system has, which can be of the type $\mathbb{Z}$ (any integer), $\mathbb{Z}_2$ (0 or 1, or ± 1, according to convention) and $2\mathbb{Z}$ (even integer). In Table 3.1 we assign to each symmetry class the different type of topological invariants according to the dimension of the system.

	Symmetry			d					
Class	TRS	PHS	CS	0	1	2	3	4	5
A	0	0	0	$\mathbb{Z}$	0	$\mathbb{Z}$	0	$\mathbb{Z}$	0
AIII	0	0	1	0	$\mathbb{Z}$	0	$\mathbb{Z}$	0	$\mathbb{Z}$
AI	+1	0	0	$\mathbb{Z}$	0	0	0	$2\mathbb{Z}$	0
BDI	+1	+1	1	$\mathbb{Z}_2$	$\mathbb{Z}$	0	0	0	$2\mathbb{Z}$
D	0	+1	0	$\mathbb{Z}_2$	$\mathbb{Z}_2$	$\mathbb{Z}$	0	0	0
DIII	-1	+1	1	0	$\mathbb{Z}_2$	$\mathbb{Z}_2$	$\mathbb{Z}$	0	0
AII	-1	0	0	$2\mathbb{Z}$	0	$\mathbb{Z}_2$	$\mathbb{Z}_2$	$\mathbb{Z}$	0
CII	-1	-1	1	0	$2\mathbb{Z}$	0	$\mathbb{Z}_2$	$\mathbb{Z}_2$	$\mathbb{Z}$
C	0	-1	0	0	0	$2\mathbb{Z}$	0	$\mathbb{Z}_2$	$\mathbb{Z}_2$
CI	+1	-1	1	0	0	0	$2\mathbb{Z}$	0	$\mathbb{Z}_2$

Table 3.1: Classification of the topological invariant according to symmetry class and number of dimensions [29]. The absence of symmetry is denoted by "0". For TRS, "$+1$" symbolizes $T^{*}T = \mathbb{1}$, "-1" symbolizes $T^{*}T = -\mathbb{1}$ and "0" symbolizes absence of the symmetry. The same for PHS. For CS, "1" symbolizes $\Gamma^{2} = \mathbb{1}$ and "0" symbolizes the absence of the symmetry. Nomenclature of the symmetry classes is the one attributed by Altland and Zirnbauer [30].

See reference [29] for a complete review on topological insulators, along with a strong mathematical foundation for their understanding, and how to compute the invariant for each symmetry class. The table goes on for higher dimensions, keeping the pattern observed in it. It is commonly called the periodic table of topological insulators and superconductors, as it is also valid for superconductors.

3.1.2 Su-Schrieffer-Heeger model

A paradigmatic example of a topological system is the Su-Schrieffer-Heeger (SSH) model. We study it in this section to pave the way for subsequent work. The SSH model is the most simple example of a non-trivial topological system. It consists of a tight-binding chain with alternating hopping amplitudes, as shown in Fig. 3.2, belonging to the BDI class.

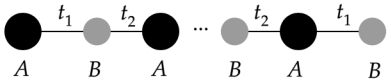

Figure 3.2: SSH chain. Each unit cell is composed by two distinct sites, A and B. t_1 is the intracell hopping amplitude, and t_2 is the intercell hopping amplitude. t_1 and t_2 might be complex.

In real space, the Hamiltonian has the following non-zero matrix elements:

$$\langle a, n|H_0|b, n\rangle = t_1,\ \langle b, n|H_0|a, n+1\rangle = t_2\,. \tag{3.7}$$

If we consider an infinite system with periodic boundary conditions we can apply the Fourier transform and obtain the Bloch Hamiltonian

$$H_0(k) = \begin{bmatrix} 0 & t_1 + t_2^* e^{-ik} \\ t_1^* + t_2 e^{ik} & 0 \end{bmatrix}. \tag{3.8}$$

If we compute the eigenvalues of the Bloch Hamiltonian (3.8), we obtain for the dispersion relation (with real hopping amplitudes to simplify)

$$\epsilon(k) = \pm\sqrt{t_1^2 + t_2^2 + 2t_1 t_2 \cos k}. \tag{3.9}$$

The minus sign corresponds to the lower band, and the plus sign corresponds to the upper band. We visualize the bands of this model for different combinations of t_1 and t_2 in Fig. 3.3.
We see that for $t_2 \neq t_1$ the bands have a finite gap. For $t_1 = t_2$, we end up in the particular case of a chain with one atom per unit cell, and the gap closes.

Although closing the chain allows to obtain the band structure analytically, it hides an important feature of the finite system. Going back to real space, for stationary states $|n\rangle = (a_n\ b_n)^\mathsf{T}$ the TISE can be written as

$$\begin{aligned} E a_n &= t_1 b_n + t_2^* b_{n-1}\,, \\ E b_n &= t_2 a_{n+1} + t_1^* a_n\,. \end{aligned} \tag{3.10}$$

Considering a semi-infinite system with $n \geq 0$, the system admits a zero energy state if

$$a_n = \left(-\frac{t_1^*}{t_2}\right)^n a_0\,,\ b_n = 0\,, \tag{3.11}$$

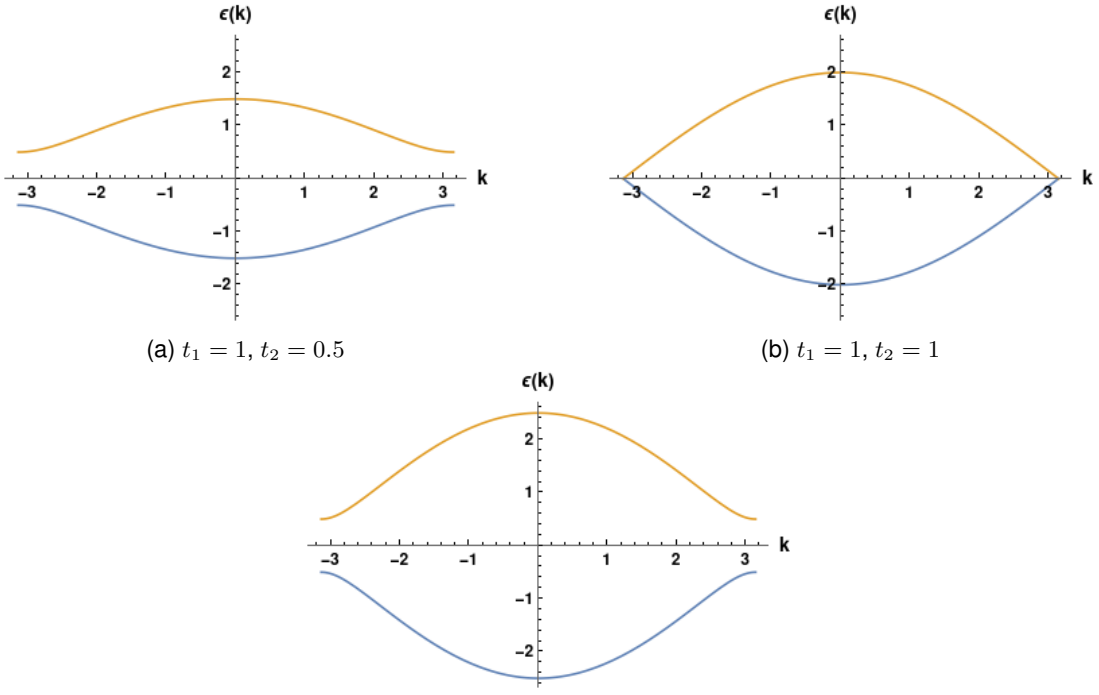

(a) $t_1 = 1, t_2 = 0.5$ (b) $t_1 = 1, t_2 = 1$

(c) $t_1 = 1, t_2 = 1.5$

Figure 3.3: Band structure of the SSH model for different values of the hopping t_2, with t_1 fixed.

which is only possible for $|t_2| > |t_1|$. We see that this state is localized in the left edge, decaying exponentially along the chain. We can also truncate the system at the site N. In that case, for $n \leq N$

$$b_n = \left(-\frac{t_1}{t_2^*}\right)^{N-n} b_N \,, \; a_n = 0 \,, \tag{3.12}$$

We see that this state is localized in the right edge, decaying exponentially along the chain. In a finite but very long chain, both edge states appear, each one occupying a different sub-lattice. We can observe this effect numerically.

We can see in Fig. 3.4c that for $t_2 > t_1$ two zero energy states appear in the spectrum. We refer to these states as bound states. All the other energies belong to what we call the bulk band. In Fig. 3.5 we plot the wave function of two eigenstates picked from the bulk band and the wave function of the zero-energy eigenstates. The bulk states are delocalized, as can be seen in the top panels of Fig. 3.5. The zero-energy states are quite different, as they are localized in the edges of the chain.The left edge state lives on the A sub-lattice, while the right one lives on the B sub-lattice, as predicted. These states are topologically protected because they persist under continuous deformations of the system, as long as the gap remains open. We then say that for $t_2 > t_1$ the system is in a topological phase, while for $t_2 < t_1$ the system is in a topologically-trivial phase. When the gap closes ($t_1 = t_2$) the system undergoes a topological phase transition. As this model belongs to the BDI symmetry class and is one dimensional, there is a topological invariant that identifies in which topological phase the system is, according to Table 3.1. To check that it belongs to the BDI class, we first rewrite the Bloch Hamiltonian (3.8) in terms of the Pauli matrices:

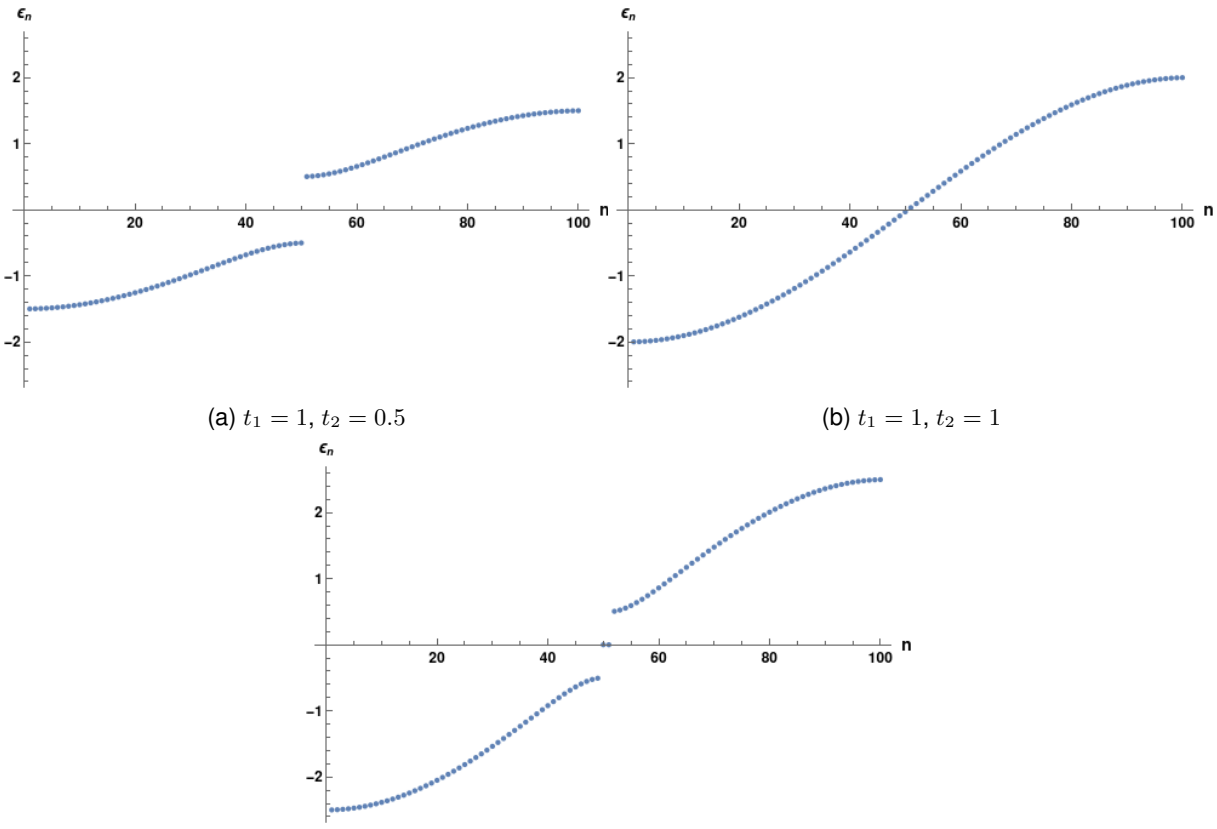

(a) $t_1 = 1$, $t_2 = 0.5$

(b) $t_1 = 1$, $t_2 = 1$

(c) $t_1 = 1$, $t_2 = 1.5$

Figure 3.4: Band structure of the open Shockley model in real space for different values of the hopping t_2, with t_1 fixed. 100 sites.

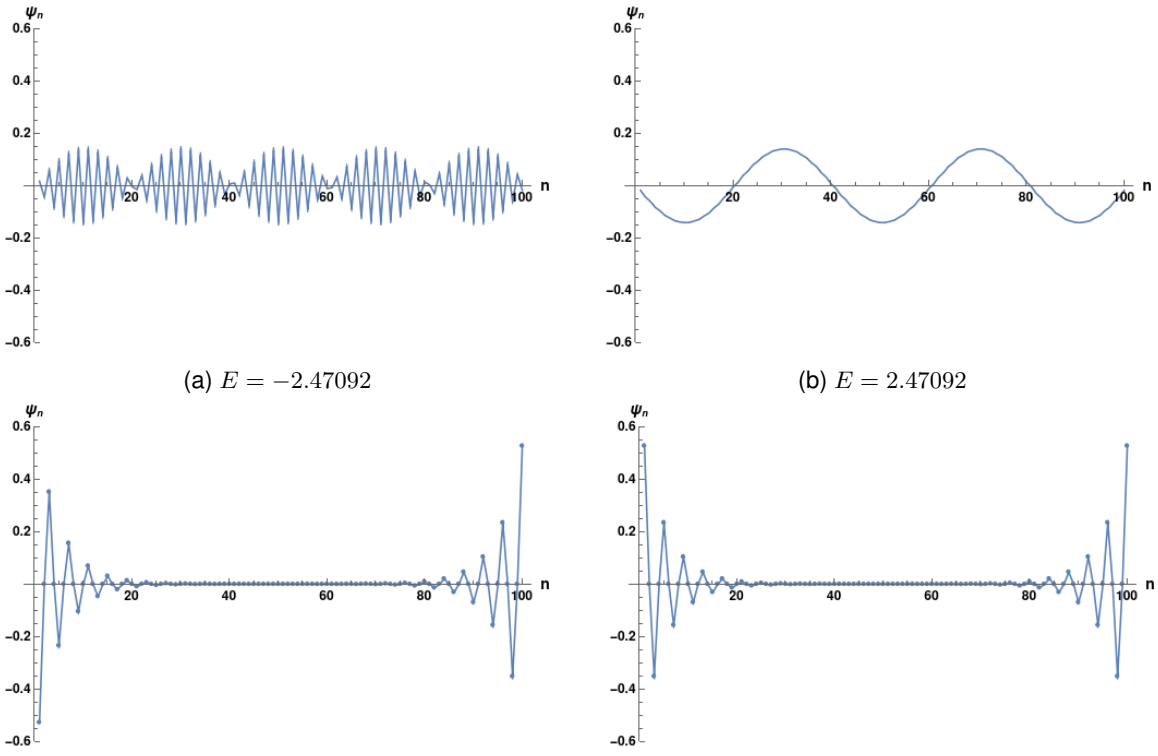

(a) $E = -2.47092$

(b) $E = 2.47092$

(c) $E = 0$

(d) $E = 0$

Figure 3.5: (a),(b): Eigenstates belonging to the bulk band; (c),(d): Bound states. $t_1 = 1$, $t_2 = 1.5$.

$$H(k) = (t_1 + t_2 \cos k)\, \sigma_x + t_2 \sin k\, \sigma_y\,, \tag{3.13}$$

and then we test for each one the symmetries:

- For TRS, we must have $H(k) = TH^{\mathsf{T}}(-k)T^{\dagger}$. Looking at the Hamiltonian above we can tell $H^{\mathsf{T}}(-k) = H(k)$. So the condition for TRS is equivalent to $[H(k), T] = 0$, which is satisfied for $T = \mathbb{1}$. So the Hamiltonian has TRS (with $T^*T = \mathbb{1}$);
- For PHS, we must have $H(k) = -CH^*(-k)C^{\dagger}$. It is easy to see that $H^*(-k) = H(k)$. So the condition for PHS is equivalent to $\{H(k), C\} = 0$, which translates to $\{\sigma_x, C\} = \{\sigma_y, C\} = 0$, valid for $C = \sigma_z$. So the Hamiltonian has PHS (with $C^*C = 1$);
- As discussed at the end of 3.1.1, if two of the three symmetries exist, then the third one also exists. So the Hamiltonian has also CS, with $\Gamma = TC^{\dagger} = \sigma_z$.

It is now confirmed that the Hamiltonian belongs to BDI class, which has a topological invariant for $d = 1$, according to the table 3.1. We will see now how to compute it. For systems with CS, the Hamiltonian can be rotated to an off-diagonal form through an unitary transformation (the same one that diagonalizes the chiral matrix Γ). Then, the rotated Hamiltonian, for two band systems, is of the form

$$H(k) = \begin{bmatrix} 0 & h(k) \\ h^*(k) & 0 \end{bmatrix}. \tag{3.14}$$

The topological invariant, denoted by ν, can be computed through

$$\nu = \frac{1}{2\pi i} \int_{\mathsf{BZ}} \mathrm{d}k\, \frac{\mathrm{d}}{\mathrm{d}k} \log h(k) = \frac{1}{2\pi i} \int_{\mathsf{BZ}} \mathrm{d}k\, \frac{h'(k)}{h(k)}\,. \tag{3.15}$$

It has the following geometrical interpretation. Focusing on the quantity $t_1 + t_2 e^{-ik}$ which appears in the Bloch Hamiltonian (3.8), varying k from 0 to 2π, the affix of $t_1 + t_2 e^{-ik}$ in the complex plane draws a circle clockwise, centered at t_1 and with radius $|t_2|$. Two cases might occur, as shown in the figure below.

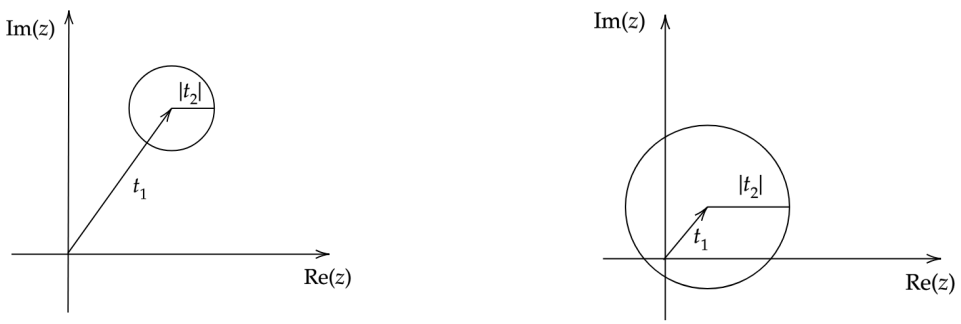

(a) Non topological case

(b) Topological case

Figure 3.6: Geometrical interpretation of the topological invariant (3.15) in the complex plane for the SSH model.

If the circle does not wrap around the origin, the system is in a non-topological phase ($\nu = 0$). If the circle wraps around the origin, the system is in a topological phase ($\nu = 1$). We identify the topological invariant with the number of times the matrix element $(H(k))_{12}$ wraps around the origin. So it is usually called winding number.

The number of states localized at an interface is equal to the (absolute) value of the difference between the topological invariants of the regions the interface separates. This rule is called bulk-edge correspondence principle. In this case, the edges are the interface between the chain and the vacuum, which for the latter $\nu = 0$.

A real life example of the SSH model is the molecule of polyacetylene. Many other theoretically proposed TIs have been confirmed in experiments [31], such as CdTe/HgTe/CdTe quantum wells (2D) or Bi_2Se_3 (3D). Nevertheless, the variety of samples is always limited. Periodic driving widens vastly the amount of potential TIs, since in that way one can induce topology on topologically trivial materials. This kind of insulators are called Floquet topological insulators and are the subject of the next section.

3.2 Floquet topological insulators

Floquet topological insulators (FTIs) are topological phases of matter resulting from external time-periodic perturbations, most commonly achieved through light-matter interactions. A common situation considered is graphene under illumination [9]. These topological phases can be achieved even in materials that in equilibrium lack topological states. The reasoning the first works on FTIs follow is that the non-equilibrium topological properties of the driven system are dictated by the topological properties of the Floquet operator and the effective Hamiltonian defined as in (2.28) [32]. However, this line of thought breaks down, since there are examples where the invariants characterizing the Floquet operator and the effective Hamiltonian vanish, and yet the system hosts topologically protected states at the boundaries [33]. This suggests that a topological classification scheme beyond the static systems is needed. M. Fruchart in [34] only considers the classes A and AIII. A complete and unified formulation of topological invariants of Floquet systems was done by Z. Wang *et al.* in [35]. The nomenclature for the symmetry classes is the same as in Table 3.1. However they need to be redefined to include the time-dependence. Being $H(\mathbf{k}, t)$ the Floquet-Bloch Hamiltonian of the system, the symmetries are defined as:

- TRS: there exists an unitary matrix T such that

$$TH^{\mathsf{T}}(-\mathbf{k}, -t)T^{\dagger} = H(\mathbf{k}, t)\,; \tag{3.16}$$

- PHS: there exists an unitary matrix C such that

$$CH^{*}(\mathbf{k}, t)C^{\dagger} = -H(-\mathbf{k}, t)\,; \tag{3.17}$$

- CS: there exists an unitary matrix Γ such that

$$\Gamma H(\mathbf{k}, -t)\Gamma^\dagger = -H(\mathbf{k}, t)\,. \tag{3.18}$$

Regarding the form of the invariants, there is a striking difference that stems from the ambiguity in the calculation of the spectrum. In static systems the topological invariant is defined as a sum over all the valence bands (recall the TKNN formula from the beginning section 3.1). In the driven case the concept of valence/conduction band is problematic since the energies are defined modulo the driving frequency, so we cannot unambiguously say that a certain band has a higher or lower energy than another one. As such, in the driven case we will have an invariant for each gap. If there are n quasienergy gaps, each one enjoying a $\mathbb{Z}$ invariant, then the classification is $\mathbb{Z}^n$. If PHS or CS is present (or both), then there are only two gaps of interest, the gap at 0 and the gap at π[1]. The classification is summarized in Table 3.2.

	Symmetry			d					
Class	TRS	PHS	CS	0	1	2	3	4	5
A	0	0	0	$\mathbb{Z}^n$	0	$\mathbb{Z}^n$	0	$\mathbb{Z}^n$	0
AIII	0	0	1	0	$\mathbb{Z}^2$	0	$\mathbb{Z}^2$	0	$\mathbb{Z}^2$
AI	+1	0	0	$\mathbb{Z}^n$	0	0	0	$2\mathbb{Z}^n$	0
BDI	+1	+1	1	$\mathbb{Z}_2^2$	$\mathbb{Z}^2$	0	0	0	$2\mathbb{Z}^2$
D	0	+1	0	$\mathbb{Z}_2^2$	$\mathbb{Z}_2^2$	$\mathbb{Z}^2$	0	0	0
DIII	-1	+1	1	0	$\mathbb{Z}_2^2$	$\mathbb{Z}_2^2$	$\mathbb{Z}^2$	0	0
AII	-1	0	0	$2\mathbb{Z}^n$	0	$\mathbb{Z}_2^n$	$\mathbb{Z}_2^n$	$\mathbb{Z}^n$	0
CII	-1	-1	1	0	$2\mathbb{Z}^2$	0	$\mathbb{Z}_2^2$	$\mathbb{Z}_2^2$	$\mathbb{Z}^2$
C	0	-1	0	0	0	$2\mathbb{Z}^2$	0	$\mathbb{Z}_2^2$	$\mathbb{Z}_2^2$
CI	+1	-1	1	0	0	0	$2\mathbb{Z}^2$	0	$\mathbb{Z}_2^2$

Table 3.2: Classification of the topological invariant according to symmetry class and number of dimensions for Floquet systems [35]. The absence of symmetry is denoted by "0". For TRS, "$+1$" symbolizes $T^*T = \mathbb{1}$, "-1" symbolizes $T^*T = -\mathbb{1}$ and "0" symbolizes absence of the symmetry. The same for PHS. For CS, "1" symbolizes $\Gamma^2 = \mathbb{1}$ and "0" symbolizes the absence of the symmetry. Nomenclature of the symmetry classes is the one atributed by Altland and Zirnbauer [30]

If the system has no topological invariant according to Table 3.2, we can try the effective Magnus Hamiltonian, and see if it belongs to a symmetry class which has a topological invariant according to Table 3.1. Nonetheless, this only makes sense for high-frequencies, and does not capture the full picture. If we want to understand the topology of Floquet systems, we must resort to a Hamiltonian belonging to a class that has a dynamical topological invariant. In this work we compute the topological invariant only for chiral systems, which can be interpreted as winding numbers in the dynamical case as well. The difference between different classes is just the restriction on the values the winding can assume [35]. How to compute the dynamical winding number is the subject of the next subsection.

[1] When we refer to the quasienergy π, it is implied that the quasienergy is in fact π/T. We multiply by T only to simplify the language. We make this abuse of language throughout this thesis.

3.2.1 Topological invariant for chiral classes (1D)

Complex logarithm and logarithm of a matrix

As only the quasi-energy gaps at 0 or π matter in chiral Floquet systems, we have two winding numbers, one for the gap at 0, ν_0, and the other for the gap at π, ν_π. The periodized time-evolution operator defined in (2.30) will be the key quantity to compute the chiral topological invariants. To obtain that operator we need to take the logarithm of the Floquet operator, and for that, we need to define the branch cut and logarithm of a matrix with care. The most common definition of the complex logarithmic function used is[2]

$$\log z \equiv \log|z| + i\arg(z)\,, \tag{3.19}$$

where $\arg(z)$ denotes the principal argument of the complex number z, i.e., the argument of z that belongs to the interval $]-\pi,\pi]$.

The logarithmic function for a general branch cut is defined such that

$$\log_\varepsilon(e^{i\phi}) = i\phi, \text{ for } \varepsilon < \phi \leq \varepsilon + 2\pi\,. \tag{3.20}$$

To relocate the branch cut to ε we use the formula

$$\arg_\varepsilon(z) = \arg(ze^{-i(\varepsilon+\pi)}) + \varepsilon + \pi\,, \tag{3.21}$$

where $\arg$ without reference to the branch cut denotes the principal argument. Then $\log_\varepsilon z$ is computed using the formula (3.19) but with $\arg$ replaced by $\arg_\varepsilon$. The complex logarithm for a given branch cut ε is thus given by

$$\log_\varepsilon(z) = \log|z| + i[\arg(ze^{-i(\varepsilon+\pi)}) + \varepsilon + \pi]\,. \tag{3.22}$$

In what follows we will need two identities:

- First identity: $$\log_{-\varepsilon}(e^{-i\phi}) = -\log_\varepsilon(e^{i\phi}) + 2\pi i\,. \tag{3.23}$$
  Proof:

$$\begin{aligned}\arg_{-\varepsilon}(e^{-i\phi}) + \arg_\varepsilon(e^{i\phi}) &= \arg(e^{-i\phi}e^{-i(-\varepsilon+\pi)}) - \varepsilon + \pi + \arg(e^{i\phi}e^{-i(\varepsilon+\pi)}) + \varepsilon + \pi = \\ &= \arg(e^{-i(\phi-\varepsilon)}e^{-i\pi}) + \arg(e^{-i(-\phi+\varepsilon)}e^{-i\pi}) + 2\pi = 2\pi\,.\end{aligned} \tag{3.24}$$

  To obtain the last equality we cancelled the first two terms appearing before the term $+2\pi$. To see that they indeed cancel check the figure below. Just replace $\phi - \varepsilon \to \alpha$.

[2] Recall that the origin of the ambiguity in the definition of the complex logarithmic function comes from the fact that the complex exponential function is not injective. For instance, $e^{i(\phi+2\pi n)}$ gives the same result for any integer n. So, to invert the exponential function e^z, i.e., to obtain the logarithmic function $\log z$, and for it to be well defined, we need to choose an interval $]\varepsilon, \varepsilon + 2\pi]$ in which $\arg(z)$ must belong to.

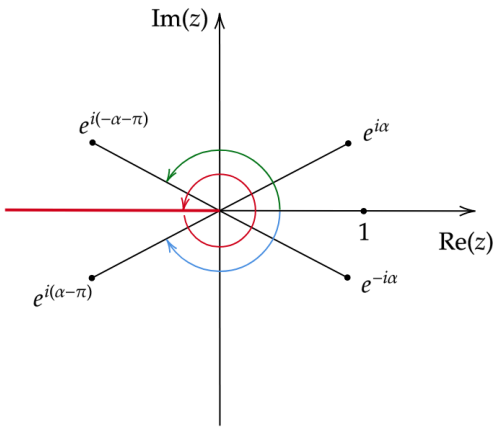

Figure 3.7: The thick red line is where the branch cut is located. The red arc is telling that the principal argument lies in the interval $]-\pi,\pi]$. The blue and green arcs have the same amplitude, but the angles (which are measured from the positive portion of the real axis) are symmetric. Thus identity (3.23) holds.

- Second identity: $$\log_{-(\varepsilon-2\pi)}(e^{i\phi}) = \log_{-\varepsilon}(e^{i\phi}) + 2\pi i\,. \tag{3.25}$$

  Proof:

$$\begin{aligned}\arg_{-(\varepsilon-2\pi)}(e^{i\phi}) &= \arg(e^{i\phi}e^{-i(-\varepsilon+2\pi+\pi)}) - \varepsilon + \pi + 2\pi = \\ &= \arg(e^{i\phi}e^{-i(-\varepsilon+\pi)}e^{-2\pi i}) - \varepsilon + 2\pi + \pi = \\ &= \arg(e^{i\phi}e^{-i(-\varepsilon+\pi)}) - \varepsilon + \pi + 2\pi = \arg_{-\varepsilon}(e^{i\phi}) + 2\pi\,.\end{aligned} \tag{3.26}$$

To take the logarithm of a matrix A we diagonalise it, obtaining thus the matrix of eigenvectors M and the eigenvalues $\lambda_1, ..., \lambda_n$. Then, the logarithm of A is

$$\log_\varepsilon A = M\text{diag}(\log_\varepsilon \lambda_1, \dots, \log_\varepsilon \lambda_n)M^{-1}\,. \tag{3.27}$$

One may ask, what if the matrix is non-diagonalizable? If that is the case, this procedure is not applicable. Fortunately, we do not need to worry about this, since we are taking the logarithm of a unitary matrix. There is a well known result from linear algebra that says that any normal matrix (i.e., a matrix such that $AA^\dagger = A^\dagger A$) is diagonalizable. In particular, unitary matrices are normal. So the Floquet operator is always diagonalizable. It might also concern the reader what happens if zero belongs to the spectrum of the matrix, since the logarithm has a singularity on that point. This problem will never arise in our case because we take the logarithm of a unitary matrix, whose spectrum is a subset of the unitary circle.

Chirality, Floquet theory and time evolution

To compute the topological invariant we will need the machinery of Floquet theory, so we will determine the constraints chirality imposes in the time-evolution, effective Hamiltonian and periodized time-evolution operators. Everything done in this section is valid for any time-periodic one dimensional chiral

Hamiltonian.

The Floquet operator is defined by

$$U(k,T) \equiv U(k;T,0) = \mathbb{T}\exp\left[-\frac{i}{\hbar}\int_0^T H(k,t')\,\mathrm{d}t'\right] \tag{3.28}$$

and is calculated numerically pointwise for $k \in [0, 2\pi]$ using a time-slice decomposition ($\hbar = 1$)

$$U_k(T) \approx \prod_{n=1}^{N} e^{-iH_k(t_n)\Delta t},\ t_n = (n-1/2)\Delta t,\ \Delta t = T/N\,, \tag{3.29}$$

N being the number of time slices.

The Floquet effective Hamiltonian is defined by

$$H_\varepsilon^{\text{eff}}(k) = \frac{i}{T}\log_{-\varepsilon} U\,, \tag{3.30}$$

where ε is the logarithm branch cut.

Finally, the periodized evolution operator (omitting the momentum dependence) is given by

$$V_\varepsilon(t) = U(t)e^{itH_\varepsilon^{\text{eff}}}\,. \tag{3.31}$$

Now we will see what symmetry constraints all these operators obey. Let's say our Hamiltonian has a chiral matrix Γ, that is,

$$\Gamma H(k,t)\Gamma^\dagger = -H(k,-t)\,. \tag{3.32}$$

The time-evolution operator satisfies

$$\Gamma U(k,t)\Gamma^\dagger = U(k,-t)\,. \tag{3.33}$$

In what follows we will omit the momentum dependency for simplicity. The proof we give for this result is present in [34]. Recall that the time-evolution operator verifies $i\partial_t U(t) = H(t)U(t)$, with $U(0) = \mathbb{1}$. On one hand, $i\partial_t \Gamma U(t)\Gamma^\dagger = \Gamma H(t)\Gamma^\dagger\Gamma U(t)\Gamma^\dagger$. So the operator $\Gamma U(t)\Gamma^\dagger \equiv R(t)$ satisfies $i\partial_t R(t) = -H(-t)R(t)$. On the other hand, $S(t) \equiv U(-t)$ satisfies $i\partial_t S(t) = -i\partial_t U(-t) = -H(-t)U(-t) = -H(-t)S(t)$. As R and S share the same initial condition ($R(0) = S(0) = U(0) = \mathbb{1}$) and same differential equation, by uniqueness of solution, we conclude $R(t) = S(t)$, that is, $\Gamma U(t)\Gamma^\dagger = U(-t)$. For a time-periodic Hamiltonian with period T we have

$$U(-t) = \mathbb{T}e^{-i\int_0^{-t} H(t')\,\mathrm{d}t'} = \mathbb{T}e^{-i\int_T^{T-t} H(t')\,\mathrm{d}t'}\,, \tag{3.34}$$

and in particular for $t = T$ we get

$$U(-T) = \mathbb{T}e^{-i\int_T^0 H(t')\,\mathrm{d}t'} = \mathbb{T}e^{i\int_0^T H(t')\,\mathrm{d}t'} = (U(T))^{-1} \equiv U^{-1}(T)\,. \tag{3.35}$$

Finally we arrived at the constraint for the Floquet operator, which is

$$\Gamma U(T)\Gamma^\dagger = U^{-1}(T)\,. \tag{3.36}$$

We can see that the chiral operator sends an eigenvalue λ of $U(T)$ to λ^{-1}. This means that if we have the spectral decomposition for the Floquet operator

$$U(T) = \sum_\alpha \lambda_\alpha |u_\alpha\rangle\langle u_\alpha|\,, \tag{3.37}$$

the chiral transformation sends it to

$$\Gamma U(T)\Gamma^\dagger = \sum_\alpha \lambda_\alpha^{-1} |u_\alpha\rangle\langle u_\alpha|\,. \tag{3.38}$$

For the effective Hamiltonian we will need the following identity:

$$\Gamma \log(A)\Gamma^\dagger = \log(\Gamma A \Gamma^\dagger)\,. \tag{3.39}$$

Then, the effective Hamiltonian verifies

$$\begin{aligned}\Gamma H_\varepsilon^{\text{eff}}\Gamma^\dagger = \frac{i}{T}\Gamma\left(\sum_\alpha \log_{-\varepsilon}(\lambda_\alpha)|u_\alpha\rangle\langle u_\alpha|\right)\Gamma^\dagger = \frac{i}{T}\sum_\alpha \log_{-\varepsilon}(\lambda_\alpha^{-1})|u_\alpha\rangle\langle u_\alpha| = \frac{i}{T}\sum_\alpha [2\pi i - \log_\varepsilon(\lambda_\alpha)]|u_\alpha\rangle\langle u_\alpha| = \\ = -\frac{2\pi}{T}\mathbb{1} - H_{-\varepsilon}^{\text{eff}}\,,\end{aligned} \tag{3.40}$$

where we used the identity (3.23) in the third equality. Additionally

$$\Gamma e^{itH_\varepsilon^{\text{eff}}}\Gamma^\dagger = e^{it\Gamma H_\varepsilon^{\text{eff}}\Gamma^\dagger} = e^{-itH_{-\varepsilon}^{\text{eff}}}e^{-2\pi it/T}\,. \tag{3.41}$$

Finally, for the periodized time-evolution operator we have

$$\begin{aligned}\Gamma V_\varepsilon(k,t)\Gamma^\dagger = \Gamma U(k,t)e^{itH_\varepsilon^{\text{eff}}}\Gamma^\dagger = \Gamma U(k,t)\Gamma^\dagger\Gamma e^{itH_\varepsilon^{\text{eff}}}\Gamma^\dagger = U(k,-t)e^{-itH_{-\varepsilon}^{\text{eff}}}e^{-2\pi it/T} = \\ = V_{-\varepsilon}(k,-t)e^{-2\pi it/T}\,.\end{aligned} \tag{3.42}$$

We summarize all the constraints obtained up to now:

- Hamiltonian (chirality):
$$\Gamma H(k,t)\Gamma^\dagger = -H(k,-t)\,; \tag{3.43}$$
- Time-evolution operator:
$$\Gamma U(k,t)\Gamma^\dagger = U(k,-t)\,; \tag{3.44}$$
- Floquet operator:
$$\Gamma U(T)\Gamma^\dagger = U^{-1}(T)\,; \tag{3.45}$$

- Effective Hamiltonian:

$$\Gamma H_{\varepsilon}^{\text{eff}}\Gamma^{\dagger} = -\frac{2\pi}{T}\mathbb{1} - H_{-\varepsilon}^{\text{eff}}\,; \tag{3.46}$$

- Periodized evolution operator:

$$\Gamma V_{\varepsilon}(k,t)\Gamma^{\dagger} = V_{-\varepsilon}(k,-t)e^{-2\pi i t/T}\,. \tag{3.47}$$

Chiral basis and change of basis

The chiral matrix Γ is unitary, so it can always be diagonalized. Furthermore, $\Gamma^2 = \mathbb{1}_N$, where the dimension of the matrix N is even. So it has eigenvalues ± 1. The chiral basis is by definition the basis in which the chiral matrix Γ has the diagonal form [3]

$$\Gamma \overset{*}{=} \begin{bmatrix} \mathbb{1}_{N/2} & 0 \\ 0 & -\mathbb{1}_{N/2} \end{bmatrix}, \tag{3.48}$$

where N is the dimension of the matrix and is even, and the asterisk above the equal sign means that the relation holds in the chiral basis. Note that Γ is hermitian. Now we will consider a matrix X by blocks $N/2 \times N/2$ such that $\{\Gamma, X\} = 0 \Leftrightarrow \Gamma X \Gamma^{\dagger} = -X$[4]. Let

$$X \overset{*}{=} \begin{bmatrix} A & B \\ C & D \end{bmatrix}. \tag{3.49}$$

We have

$$\Gamma X \Gamma^{\dagger} \overset{*}{=} \begin{bmatrix} A & -B \\ -C & D \end{bmatrix}. \tag{3.50}$$

The anti-commutation relation together with (3.49) and (3.50) yields $A = D = 0$, which means that X in the chiral basis is antidiagonal. Similarly, a matrix that commutes with the chiral matrix is diagonal in the chiral basis. To change to this basis we need to diagonalize Γ to obtain its matrix of eigenvectors M. For a matrix A in a certain basis, the same matrix in the chiral basis A' is obtained by

$$A' = M^{-1}AM\,. \tag{3.51}$$

Chiral invariant

The constraint (3.47) involves the periodized time-evolution operator at different times and different branch cuts, so it is not useful yet. Dealing with the time reversal, we note that $V_{\varepsilon}(k,-t) = V_{\varepsilon}(k,T-t)$ due to the periodicity of V. For $t = T/2$, Eq. (3.47) leads to

$$\Gamma V_{\varepsilon}(k,T/2)\Gamma^{\dagger} = -V_{-\varepsilon}(k,T/2)\,. \tag{3.52}$$

[3] In general the number of plus ones can be different from the number of minus ones, but we will not deal with those cases here.
[4] Note that the anti-commutation/commutation relation holds in any basis.

For the branch cut (or gap) at $\varepsilon = 0$ the last equation gives us the constraint

$$\Gamma V_0(k, T/2)\Gamma^\dagger = -V_0(k, T/2)\,. \tag{3.53}$$

For the branch cut (or gap) at $\varepsilon = \pi$, we will need to compute $V_{\varepsilon-2\pi}(k,t) = U(k,t)\exp(itH^{\text{eff}}_{\varepsilon-2\pi})$. The effective Hamiltonian with branch cut at $\varepsilon - 2\pi$ is

$$H^{\text{eff}}_{\varepsilon-2\pi} = \frac{i}{T}\sum_\alpha \log_{-\varepsilon+2\pi}(\lambda_\alpha)|u_\alpha\rangle\langle u_\alpha| = \frac{i}{T}\sum_\alpha [2\pi i + \log_{-\varepsilon}(\lambda_\alpha)]|u_\alpha\rangle\langle u_\alpha| = -\frac{2\pi}{T}\mathbb{1} + H^{\text{eff}}_\varepsilon\,, \tag{3.54}$$

where the second equality comes from property (3.25). So, for the periodized time-evolution operator we have

$$V_{\varepsilon-2\pi}(k,t) = U(k,t)e^{itH^{\text{eff}}_\varepsilon}e^{-2\pi it/T}\,. \tag{3.55}$$

In particular, for the case $\varepsilon = \pi$ at $t = T/2$ it follows

$$V_{-\pi}(k, T/2) = U(k, T/2)e^{iTH^{\text{eff}}_\pi/2}e^{-2\pi iT/2T} = -V_\pi(k, T/2)\,. \tag{3.56}$$

Finally, the constraint (3.52) for the $\varepsilon = \pi$ case is

$$\Gamma V_\pi(k, T/2)\Gamma^\dagger = -V_{-\pi}(k, T/2) = V_\pi\,. \tag{3.57}$$

As $V_0(T/2)$ (ommiting the k dependence) anti-commutes with the chiral matrix, it is off-diagonal in the chiral basis. We write

$$V_0(T/2) \overset{*}{=} \begin{bmatrix} 0 & V_0^+ \\ V_0^- & 0 \end{bmatrix}, \tag{3.58}$$

where $V_0^\pm$ are unitary matrices.

As $V_\pi(T/2)$ commutes with the chiral matrix, it is diagonal in the chiral basis. We write

$$V_\pi(T/2) \overset{*}{=} \begin{bmatrix} V_\pi^+ & 0 \\ 0 & V_\pi^- \end{bmatrix}, \tag{3.59}$$

with the matrices $V_\pi^\pm$ being unitary too. In the end, the winding ν_ε is calculated through[5]

$$\nu_\varepsilon = \frac{i}{2\pi}\int_{\text{BZ}} \text{Tr}[(V_\varepsilon^+)^{-1}\partial_k V_\varepsilon^+]\,\mathrm{d}k\,. \tag{3.60}$$

As our models have two bands, the V^+'s that appear in the integrand are complex numbers, thus the inverse that appears inside the trace is just the inverse of a complex number and consequently there is no need to take the trace.

[5]The result is basis independent, so we can choose the chiral one in particular. The given formula assumes that the V^+ matrices are in the chiral basis.

3.3 zx model

We already gave an example of a static topological system. In this section we give an example of a dynamic model that we will use later for studying transport. Consider the Hamiltonian

$$H(k,t) = (\sin k, 0, \cos k + A\cos(\Omega t) + \mu) \cdot \boldsymbol{\sigma}\,, \tag{3.61}$$

where A and Ω are the amplitude and frequency of the driving, respectively, μ is a real constant and $\boldsymbol{\sigma} = (\sigma_x, \sigma_y, \sigma_z)$ is the vector of the Pauli matrices. This model has no σ_y, so we call it the zx model. It is easy to see that it belongs to the BDI symmetry class of Table 3.2, with $T = \sigma_z$, $C = \sigma_x$ and $\Gamma = \sigma_y$. Before addressing the topology of this model, it would be instructive to make some remarks on the static counterpart.

3.3.1 Static zx model

The static model with $A = 0$ in (3.61) belongs to BDI symmetry class of Table 3.1. So this model, being 1D, admits a non-trivial winding number. Let us at first rotate the Hamiltonian to an off-diagonal form. Let

$$U = \begin{bmatrix} -\frac{i}{\sqrt{2}} & -\frac{i}{\sqrt{2}} \\ \frac{1}{\sqrt{2}} & \frac{1}{\sqrt{2}} \end{bmatrix}\,, \tag{3.62}$$

then

$$U^\dagger H(k) U = \begin{bmatrix} 0 & ie^{-ik} + i\mu \\ -ie^{ik} - i\mu & 0 \end{bmatrix}\,. \tag{3.63}$$

We can see that this Hamiltonian has a non-zero winding number for $|\mu| < 1$. The cases $\mu < 1$ and $\mu > 1$ are depicted in Fig. 3.8, similarly to Fig. 3.6.

As we did for the SSH model, we will now see that edge-states appear in a (long) finite chain, according to the bulk-edge correspondence. For that, we will need the Hamiltonian in real space which is

$$H = \sum_{j,j'}^{\text{cells}} \begin{pmatrix} a_j^\dagger & b_j^\dagger \end{pmatrix} \mathbf{h}_{j,j'}.\boldsymbol{\sigma} \begin{pmatrix} a_{j'} \\ b_{j'} \end{pmatrix} = \sum_{j,j'}^{\text{cells}} \mathbf{h}_{j,j'}.\boldsymbol{\sigma}^{\mu\nu} c_{j,\mu}^\dagger c_{j',\nu}\,, \tag{3.64}$$

where $\mu, \nu = A, B$ indicate the atom type of the site in the unit cell, and

$$\mathbf{h}_{j,j'} = \left[\frac{1}{2i}(\delta_{j+1,j'} - \delta_{j-1,j'}), 0, \mu\delta_{j,j'} + \frac{1}{2}(\delta_{j,j'+1} + \delta_{j,j'-1})\right]\,. \tag{3.65}$$

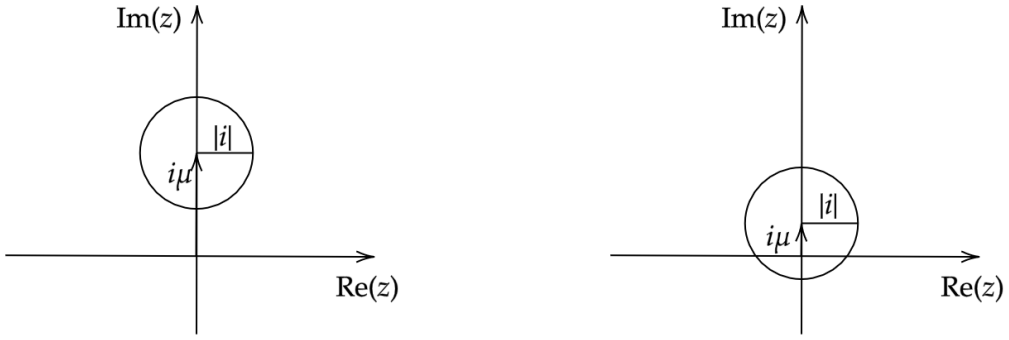

(a) Non topological case

(b) Topological case

Figure 3.8: Geometrical interpretation of the winding number in the complex plane for the static zx model.

The driven Hamiltonian in real space is obtained by replacing $\mu \to \mu + A\cos(\Omega t)$ in Eq. (3.65). The derivation is carried out in Appendix A. Fig. 3.9 illustrates a tight-binding chain described by the Hamiltonian at hand.

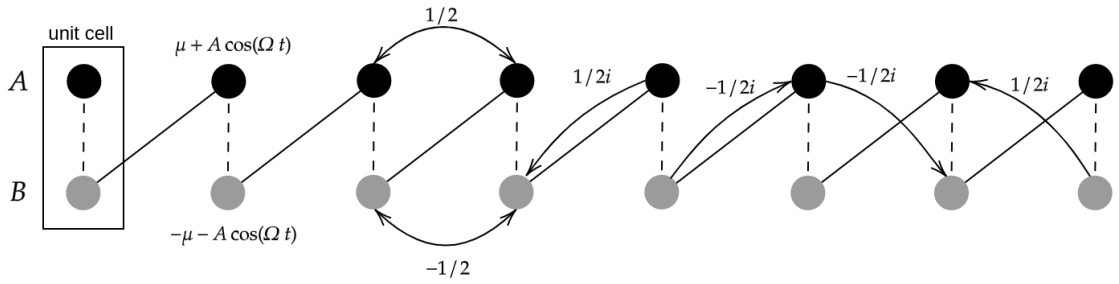

Figure 3.9: Tight-binding chain of eight unit cells, described by the Hamiltonian (3.61).

We can see in Fig. 3.10 that for $\mu = 1.5$ there are no zero-energy modes ($\nu = 0$), while for $\mu = 0.5$ ($\nu = 1$) two zero-energy states appear, as expected. For $\mu = 1$ the gap closes (ν undefined). The probability density of the bound states are represented in Fig. 3.11, side by side with a bulk-state.

We verified the bulk-edge correspondence for the SSH model and the static zx model. In the next section we will see that the bulk-edge correspondence still holds in the driven case.

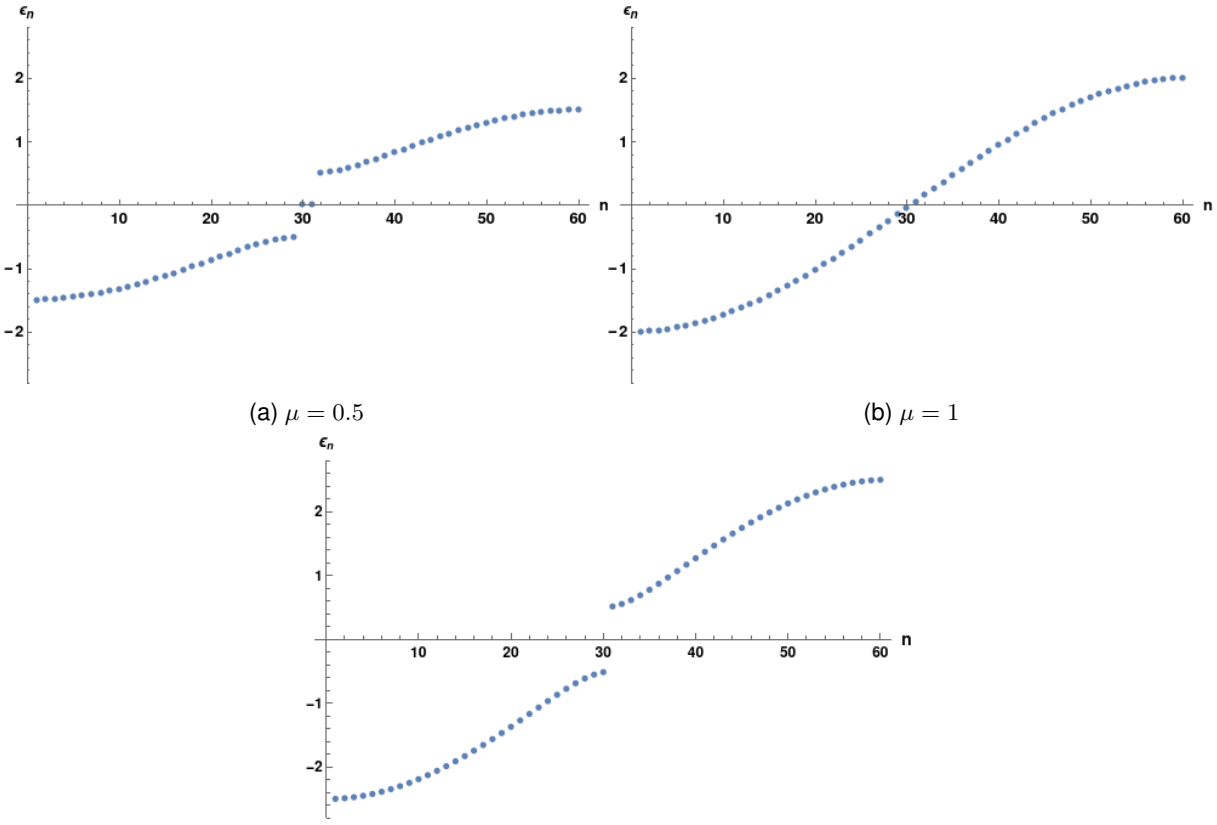

(a) $\mu = 0.5$

(b) $\mu = 1$

(c) $\mu = 1.5$

Figure 3.10: Band structure of the static zx model in real space for different values of the parameter μ. 60 sites.

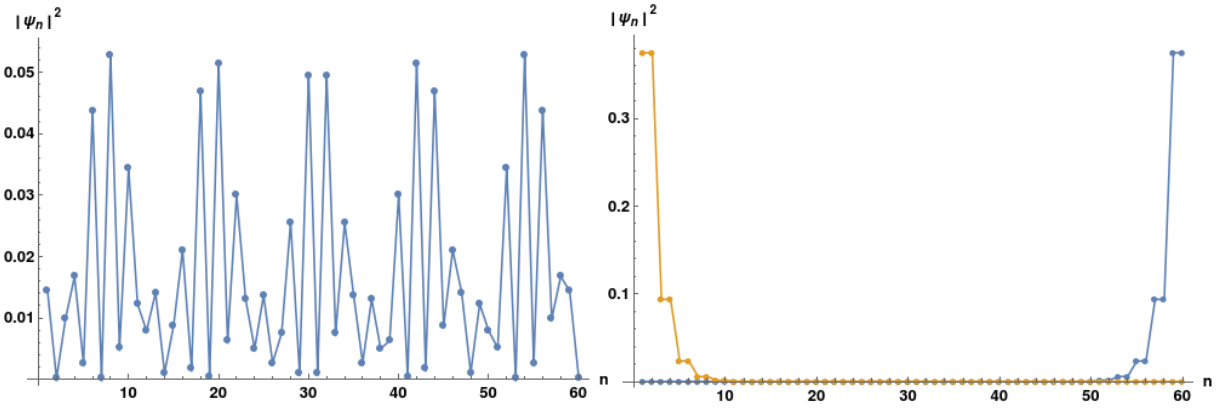

(a) $E = 0.625373$

(b) $E = 0$

Figure 3.11: (a) Probability density of a bulk state. (b) Probability density of the zero-energy states. $\mu = 0.5$. 60 sites.

3.3.2 Dynamic zx model

You can see in Table 3.2 that the BDI symmetry class, in one dimension, has the topological classification of $\mathbb{Z}^2$, which means we have two topological invariants, one for the gap at 0, ν_0, and the other for the gap at π, ν_π. In the static case, there is only one gap. In the case of Floquet systems, many gaps arise since the quasienergies are defined modulo 2π, and thus the bands replicate *ad infinitum*. When PHS or CS is present (or both), the only non-equivalent gaps are the gap at 0 and the gap at π [35]. Fig. 3.12 illustrates both gaps.

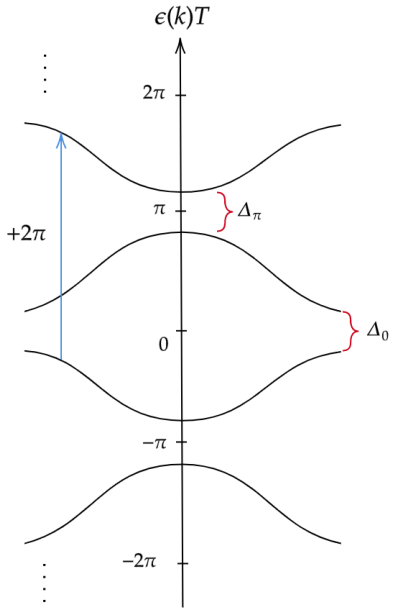

Figure 3.12: Illustration of the Floquet bands. The blue arrow points out the gauge invariance discussed in subsection 2.2.1. The gap at zero-energy is indicated by Δ_0, while the gap at π is indicated by Δ_π.

So when the gap at 0 closes, we expect the winding ν_0 to experience a transition. The same for the gap at π and ν_π. This idea is visualized in Appendix B. Now we will verify the bulk-edge correspondence in the driven case for the present model. Consider Fig. 3.13. In Fig. 3.13a the quasienergy bands in the Floquet zone of the closed system are shown. These were obtained from the spectrum of the Floquet operator computed numerically through (2.20) using the Floquet-Bloch Hamiltonian (3.61). Fig. 3.13b shows the Floquet zone of the open system. It was computed through diagonalization of the matrix representing the Floquet Hamiltonian $\mathbb{K}$ as in (2.41). We see that two zero-energy bound states appear. We will call them 0-modes. States with (adimensional) quasienergies $\pm\pi$ do not appear. We will call them π-modes. This is in accordance with the winding invariants computed as explained in subsection 3.2.1, which are $(\nu_0, \nu_\pi) = (1, 0)$. Fig. 3.13c shows the time averaged probability density of a selected bulk state, which can be seen to be non-localized. Fig. 3.13d shows the time averaged probability density of the bound states, which can be seen to be localized on the edges of the chain.

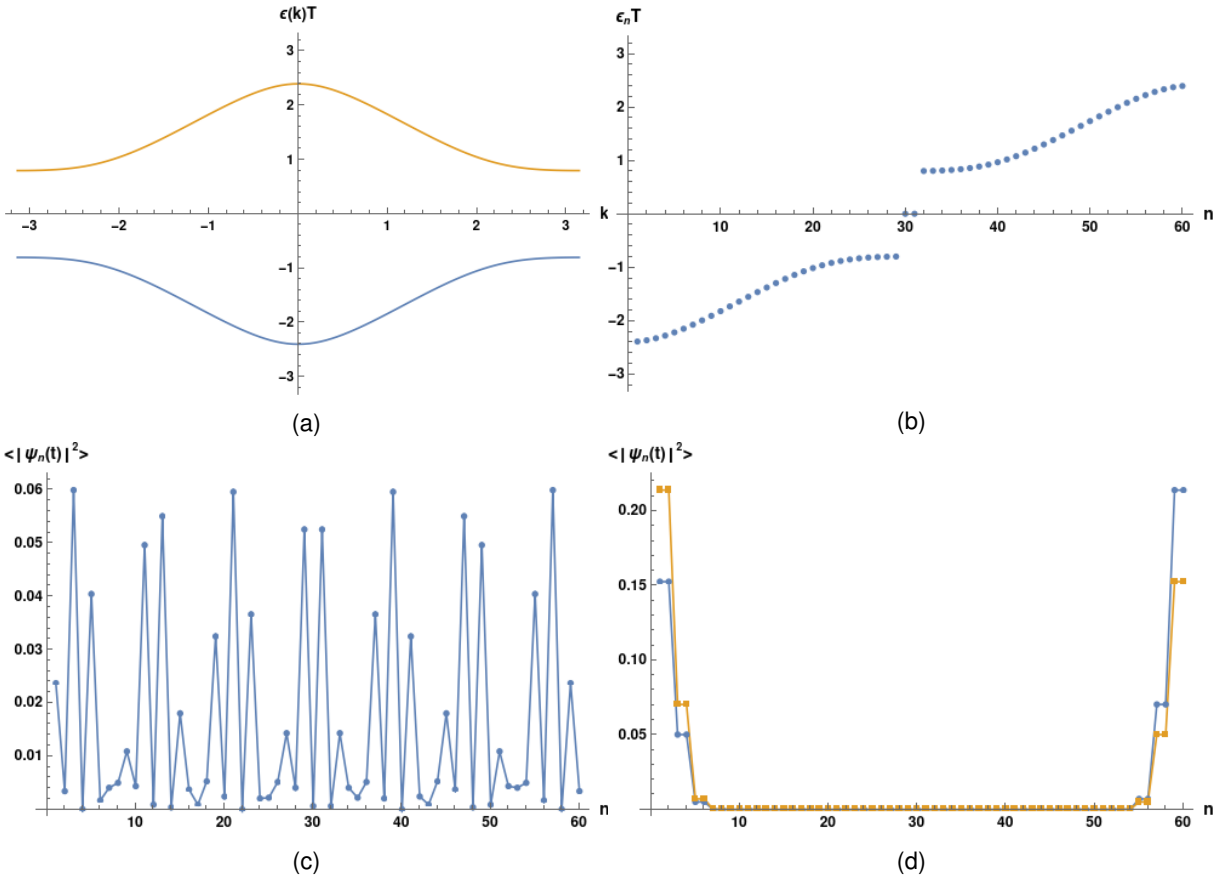

Figure 3.13: (a): Floquet zone of the closed system; (b): Floquet zone of the open system.; (c): Bulk state. $\epsilon T = 2.07714$; (d): 0-modes. $\mu = 0.5$, $A = 2$, $T = 1.6$. $(\nu_0, \nu_\pi) = (1, 0)$. 60 sites

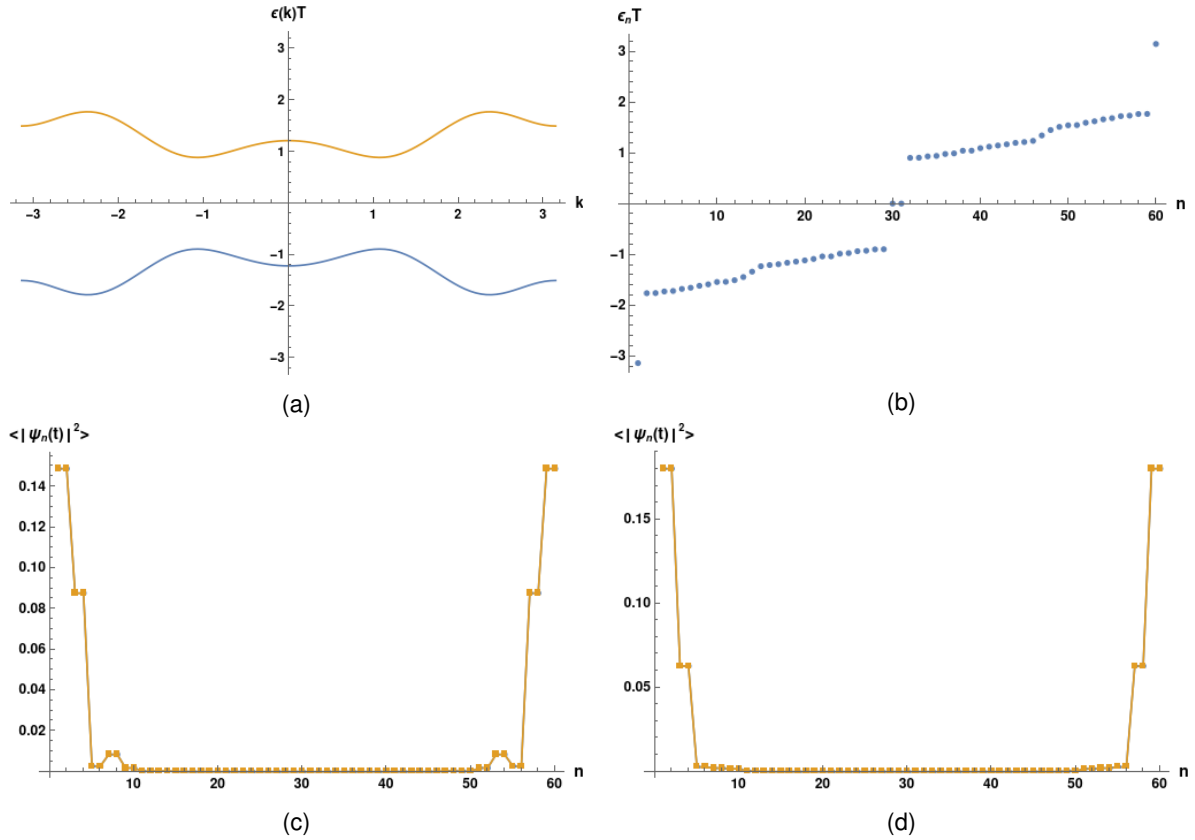

Figure 3.14: (a): Floquet zone of the closed system; (b): Floquet zone of the open system. ; (c): 0-modes; (d): π-modes. $\mu = 1.5$, $A = 2$, $T = 3$. 60 sites. $(\nu_0, \nu_\pi) = (-1, -1)$.

The time-averaged probability density is computed in the following way. Let $|\psi_\epsilon\rangle$ be a Floquet state solution of the TDSE such that

$$|\psi_\epsilon(t)\rangle = e^{-i\epsilon t}|u_\epsilon(t)\rangle\,, \tag{3.66}$$

where ϵ is the quasienergy and $|u_\epsilon(t)\rangle$ the Floquet function, which verifies the Floquet equation (2.24). The Floquet function admits a Fourier series just as in (2.38a). The Fourier components are obtained through diagonalization of $\mathbb{K}$. Then, the time-averaged probability density at the i-th site is

$$\langle|\psi_{\epsilon,i}(t)|^2\rangle = \frac{1}{T}\int_0^T |\langle i|\psi_\epsilon(t)\rangle|^2\,\mathrm{d}t = \frac{1}{T}\int_0^T \left(\sum_n e^{-in\omega t}\langle i|u_{\epsilon,n}\rangle\right)\left(\sum_m e^{im\omega t}\langle i|u_{\epsilon,m}\rangle^*\right)\,\mathrm{d}t = \tag{3.67}$$

$$= \sum_{n,m}\underbrace{\frac{1}{T}\int_0^T e^{i(m-n)\Omega t}\,\mathrm{d}t}_{\delta_{n,m}}\langle i|u_{\epsilon,n}\rangle\langle i|u_{\epsilon,m}\rangle^* = \sum_n |\langle i|u_{\epsilon,n}\rangle|^2\,. \tag{3.68}$$

The example of Fig. 3.14 has both 0-modes and π-modes. Notice that in this example $|\mu| > 1$. In this case, the static system hosts no edge modes, since $\nu = 0$. This confirms the idea that the external drive can induce non-trivial topological phases from trivial ones. In the next figure we present the phase diagram of this model, which reveals how rich the topology of Floquet systems can be.

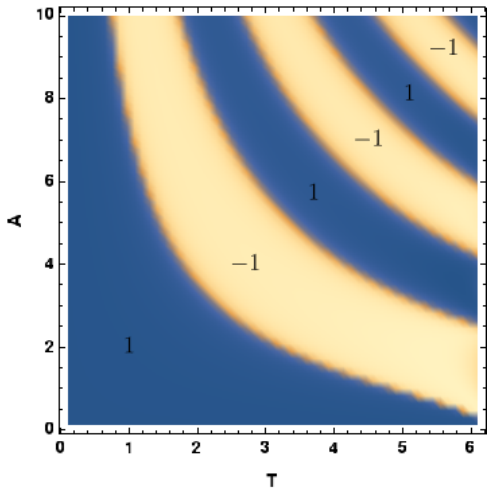

(a) Plot of ν_0, for $\mu = 0$.

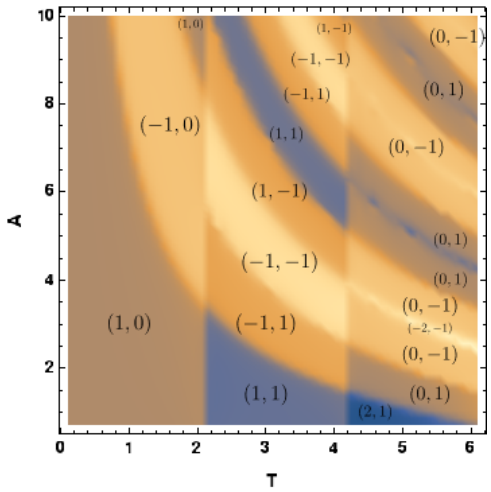

(b) Plot of (ν_0, ν_π) for $\mu = 0.5$.

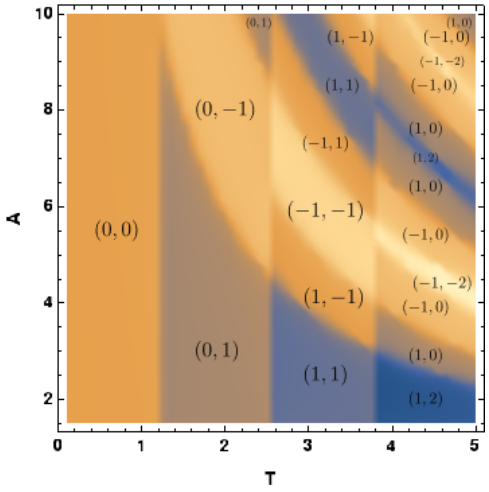

(c) Plot of (ν_0, ν_π) for $\mu = 1.5$.

Figure 3.15: Phase diagram of the zx model for two values of μ. A and T are the amplitude and period of the drive, respectively. In (b) each topological phase is characterized by the pair (ν_0, ν_π).

Fig. 3.15a only shows the winding at zero because we obtained that the winding at π is trivial for $\mu = 0$.

Up to now we have only considered homogeneous chains. Introducing a boundary between two distinct phases in the chain will provide interesting features to the transport properties of the system. In the next section we will see what happens to the bound states in inhomogeneous chains.

3.4 Inhomogeneous chains

We have already confirmed the bulk-edge correspondence when the interface was the edge of the chain, separating it from the vacuum. Let us see what happens when we have two portions of the chain in different phases, with their boundary at the center of the chain. We consider a static SSH chain that starts with hopping amplitudes $t_1,\ t_2 = t$ and ends with hopping amplitudes $t_1,\ t_2 = t'$. This can be achieved through an hyperbolic tangent profile

$$t_2(n) = \frac{t+t'}{2} - \frac{t'-t}{2} \tanh \frac{N/4-n}{l}\,, \tag{3.69}$$

where n is the unit cell, N is the number of sites, and l the length of the transition. We choose the interface to be located at the cell $N/4$ and $l = 1$ throughout this work. The spectrum of the inhomogeneous SSH chain for four cases is depicted in Fig. 3.16, while the bound states, when present, are shown in

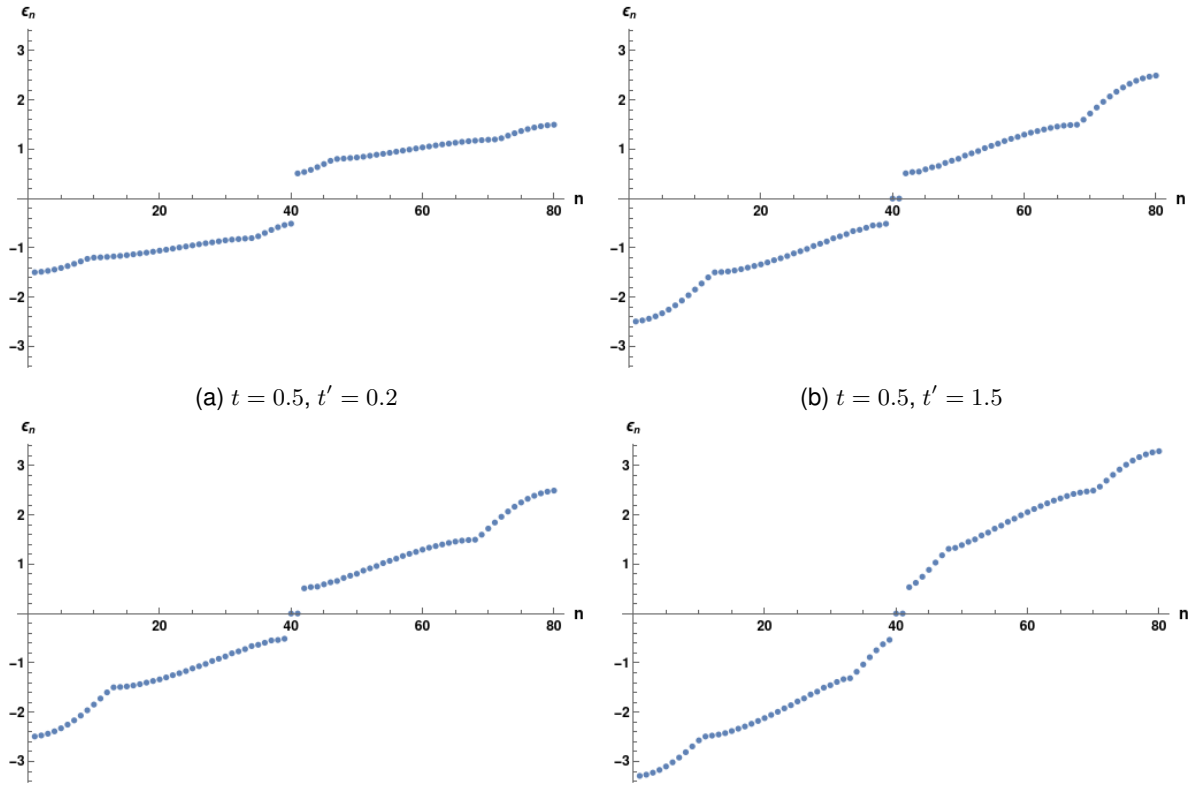

(a) $t = 0.5$, $t' = 0.2$ (b) $t = 0.5$, $t' = 1.5$

(c) $t = 1.5$, $t' = 0.5$ (d) $t = 1.5$, $t' = 2.3$

Figure 3.16: Spectrum of inhomogeneous chains of the SSH model. $t_1 = 1$, 80 sites, $M = 20$, $l = 0.5$.

We can see that the case of Fig. 3.16a has no bound states. This happens because both left and right portions of the chain are in the non-topological phase. The second case has two bound states. As the right portion of the chain is in the topological phase ($t' > t_1$), we expect a bound state located at the right edge, and a localized state in the middle of the chain, since the left portion is in the trivial phase. See Fig. 3.17a. The third case, respective to Figs. 3.16c and 3.17b, is similar to the second case, except that the edge-state is now localized in the left edge. In the last case, the chain hosts two bound states. However, these states are localized in edges. No state localized in the center appears since both left and right portion of the chain are in the same topological phase.

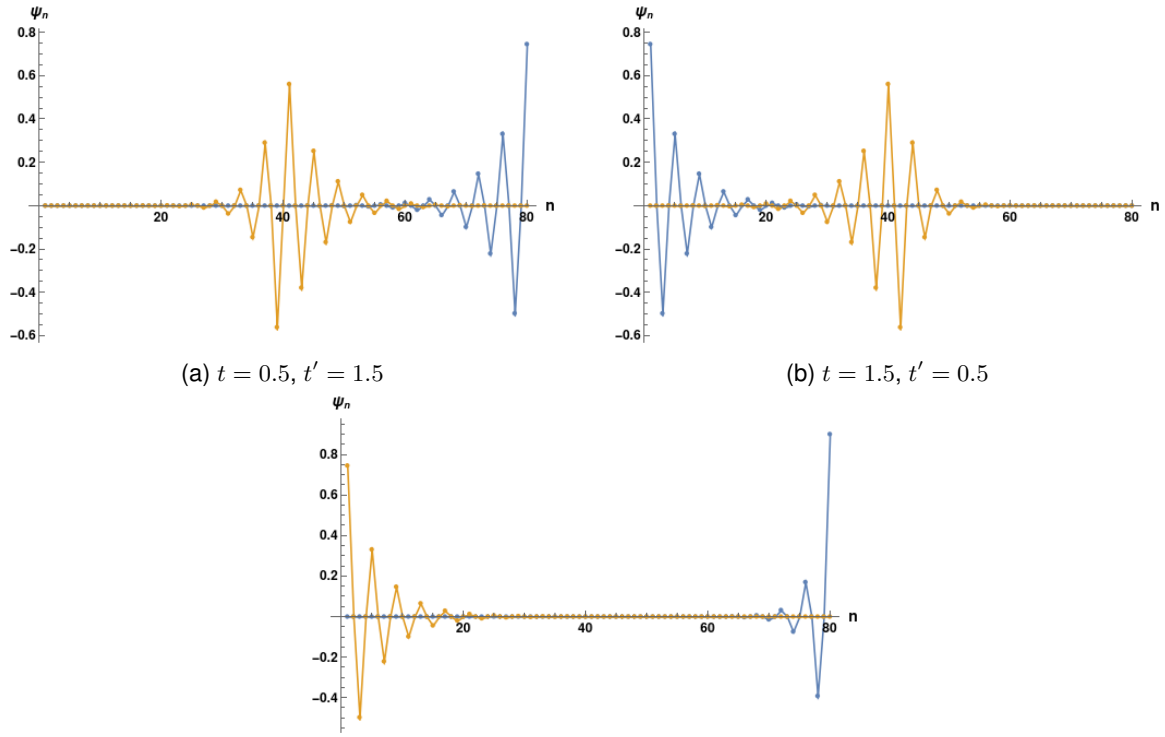

(a) $t = 0.5$, $t' = 1.5$

(b) $t = 1.5$, $t' = 0.5$

(c) $t = 1.5$, $t' = 2.3$

Figure 3.17: Bound states of inhomogeneous chains of the SSH model. $t_1 = 1$, 80 sites, $M = 20$, $l = 0.5$.

Now we consider the driven case, in particular our zx model, and see that the bulk-edge correspondence applies in the driven case as well. As first example, we consider two phases, one with $(\nu_0, \nu_\pi) = (1, 0)$ and other with $(\nu_0, \nu_\pi) = (-1, 0)$, fixing all parameters but the amplitude of the driving. We choose $T = 1.6$, $\mu = 0.5$, $A_L = 2$ for the amplitude in the left portion of the chain and $A_R = 6$ for the right one. So the left portion of the chain is in the phase $(\nu_0^L, \nu_\pi^L) = (1, 0)$ and the right one in the phase $(\nu_0^R, \nu_\pi^R) = (-1, 0)$. As $|\nu_0^L - \nu_0^R| = 2$, in Fig. 3.18a it can be seen that four bound states appear, two localized at edges, and two localized at the center, as Fig.3.18b shows (the plot in green overlaps with the yellow one). As $\nu_\pi = 0$ in both phases, no π-modes appear.

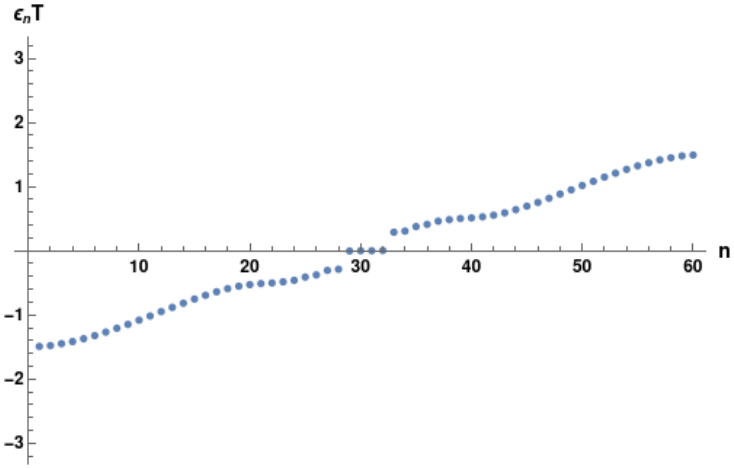

(a)

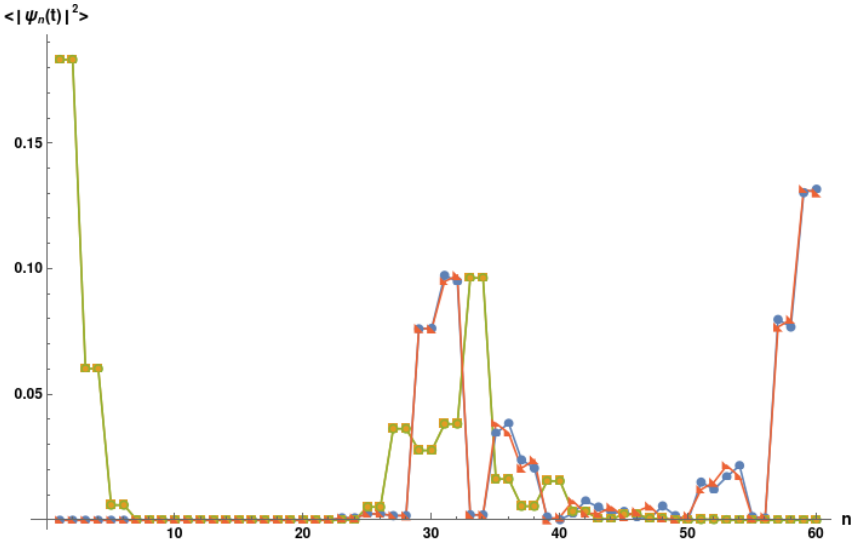

(b)

Figure 3.18: (a) Floquet zone of an inhomogeneous chain of the zx mode; (b) Bound states. $\mu = 0.5$, $T = 1.6$, $A_L = 2\,(1, 0)$, $A_R = 6\,(-1, 0)$. 60 sites.

The figure below shows an example where both phases have a vanishing winding at 0, but a non-vanishing winding at π, with $\nu_\pi^L = -\nu_\pi^R = 1$. As such, we will have four bound states, two at $\varepsilon = -\pi$ and two at $\varepsilon = \pi$.

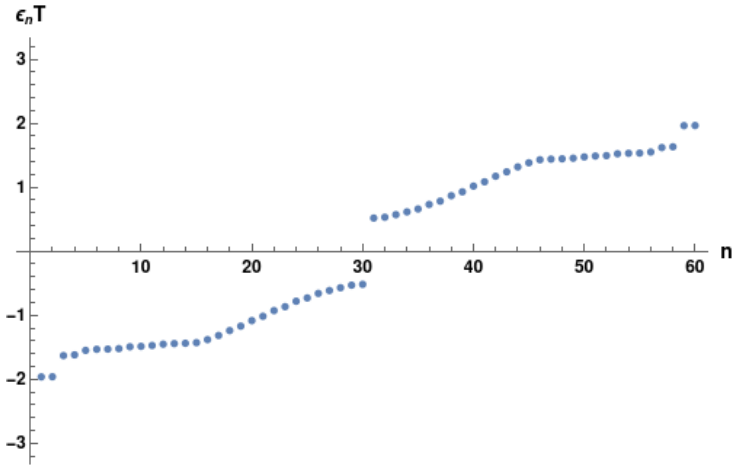

(a)

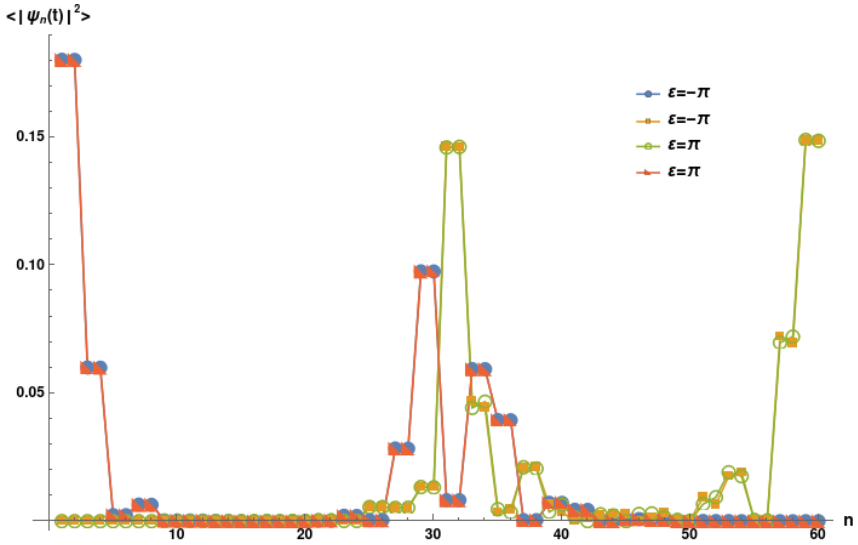

(b)

Figure 3.19: (a) Floquet zone of an inhomogeneous chain of the zx model; (b) respective bound states. $\mu = 1.5$, $T = 1.6$, $A_L = 2\ (0, 1)$, $A_R = 10\ (0, -1)$. 60 sites. $M = 15$, $l = 1$.

We can conclude that the bulk-edge correspondence applies to the driven case as well, for both the gap at zero and the gap at π.

Chapter 4

Electrical transport in periodically driven systems

Recent technological achievements allow the manipulation of matter at ever smaller scales. This contributes for the progress of nanosciences, which open routes to promising applications in the industry, healthcare and research. Electrical transport at the nanoscale in particular has been receiving lots of attention from the industry since there is a demand for better performing electronics. The scientific community has payed attention to electrical transport in the past decades, but transport at nanoscale is since the late 80's the focus of the subject, since many phenomena that occur at the nanoscale are not observed at bigger scales and are yet to be understood.

Electrical transport is a broad subject and brings together many fields of physics. It has several approaches, depending on the system one wants to describe and physical limits we are considering. One possible approach is Kubo's formalism, where the current is computed via quantum mechanics as a response to an external electromagnetic field. A classical approach to transport is Drude's model, which is an application of Boltzmann's kinetic theory of gases to electrons in solids. Drude's conductivity can be obtained as a particular case of Kubo's conductivity as well. Although Boltzmann's kinetic theory is classical, it can be extended to electrons by accounting for Fermi statistics, so that we end up with a semiclassical approach to transport. The approach followed in this work is an extension of the Landauer-Büttiker formalism [24, 36], which is fully quantum, to systems with periodic time-dependence, and is based on Ref. [12]. Nonetheless, it is instructive to first mention the static case.

4.1 Static conductors

The Landauer-Büttiker formalism is a scattering approach to the problem of transport, where the current is a manifestation of electronic tunneling across a junction, induced by an applied voltage. The configuration of the system we have in mind is sketched in Fig. 4.1. The system is composed by a junction, a nanotube or a molecular wire for exampe, coupled to two electrodes. The electrodes are metallic leads connected to a battery which applies a voltage between them.

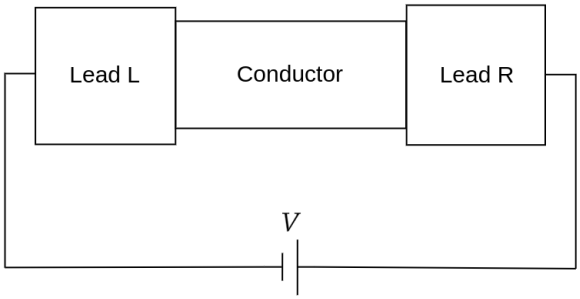

Figure 4.1: Electrode-junction-electrode structure.

To find a closed formula for the electrical current, five approximations must be made. The first one consists in replacing the battery by two reservoirs, one coupled to the left lead and the other coupled to the right lead. Each reservoir is at a fixed chemical potential $\mu_l, l = L, R$, so that the applied bias is $V = (\mu_R - \mu_L)/e$, $e > 0$. In the second approximation we expect the system to reach a stationary state, so that the current computed is the same at all times. In the third approximation the open system is replaced by a closed infinite one, with scattering boundary conditions, where the role of the reservoirs is simply to continually prepare electrons in the distant past, and far away from the nanojunction, into wave-packets which scatter on the junction, that may be transmitted or reflected, and move far away from it without further scattering, traveling deep into the lead in the distant future. In the fourth approximation electrons do not experience mutual interactions, so we work only with one particle Hamiltonians. The fifth approximation assumes that both reservoirs are at thermal equilibrium, so that the energy states of lead l are populated according to the Fermi-Dirac distribution

$$f_l(E) = \frac{1}{e^{(E-\mu_l)/k_B T} + 1}\,, \tag{4.1}$$

where k_B is the Boltzmann constant and T is the temperature. Under this set of approximations, the average current is given by [24]

$$I = \frac{e}{\pi\hbar}\int_{-\infty}^{+\infty} \mathrm{d}E\,[f_L(E) - f_R(E)]T(E)\,, \tag{4.2}$$

where $T(E)$ is the electron transmission probability at energy E and is given by

$$T(E) = \mathrm{Tr}[\mathcal{G}^\dagger(E)\Gamma_R(E)\mathcal{G}(E)\Gamma_L(E)]\,, \tag{4.3}$$

where $\mathcal{G}$ is the electron's Green function and Γ_l is related to the self-energy Σ_l appearing in (2.45) through $\Gamma_l = -2\Im\{\Sigma_l\}$.

The current as written in equation (4.2) is a very complicated function of the system parameters. However, we can linearize the expression with respect to the bias $V = (\mu_R - \mu_L)/e$ whenever the chemical potentials are very near to the Fermi energy E_F. For $\mu_R = E_F + eV/2$ and $\mu_L = E_F - eV/2$ with $|V| \ll E_F$ the average current is

$$I = GV\,, \tag{4.4}$$

where

$$G = \frac{e^2}{h} T(E_F) \tag{4.5}$$

is the differential conductance and $T(E_F)$ the transmission probability computed at the Fermi energy. For ohmic conductors relation (4.4) holds for any bias, and the differential conductance coincides with the linear conductance.

4.2 Driven transport

In this section we analyze the problem of electrical transport in periodically driven systems. As the time-dependence is periodic, Floquet's formalism sets a good background to work on. In alternative to the Floquet's approach one could use non-equilibrium Green functions techniques [24]. However, those would be advantageous if we considered electron-electron interactions, which is not our case. First we describe the setup of our model, which is sketched in Fig. 4.2.

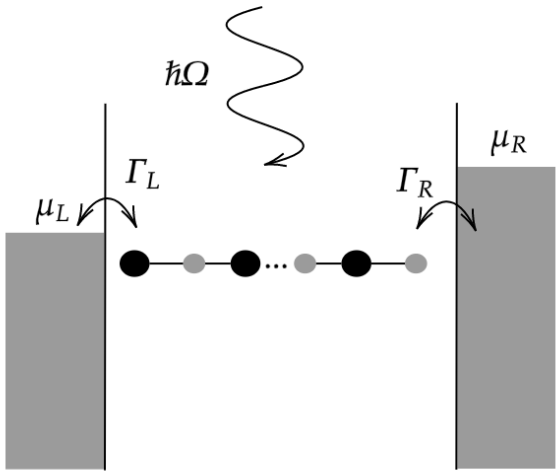

Figure 4.2: Driven tight-binding chain (conductor) coupled to two leads (electrodes), with chemical potentials μ_L and $\mu_R = \mu_L + eV$.

The structure of the system in mind is similar to the one of Fig. 4.1, except for the fact that the conductor is now subject to an external drive with frequency Ω. The conductor in our case is a tight-binding chain with N sites coupled to the leads only through the end sites. The Hamiltonian of the system is given by

$$H(t) = H_{\text{wire}}(t) + H_{\text{leads}} + H_{\text{contacts}} \,, \tag{4.6}$$

with the different terms corresponding to the wire, the leads and the coupling between the wire and the

leads, respectively.

The Hamiltonian of the wire is of the form

$$H_{\text{wire}}(t) = \sum_{n,n'} H_{nn'}(t) c_n^\dagger c_{n'} \,, \tag{4.7}$$

where $c_n^\dagger / c_n$ creates/annihilates an electron at the orbital $|n\rangle$, and $H_{nn'}(t+T) = H_{nn'}(t)$, where $T = 2\pi/\Omega$ is the driving period.

The leads are modeled by free electron gases, with Hamiltonian

$$H_{\text{leads}} = \sum_q \epsilon_q (c_{Lq}^\dagger c_{Lq} + c_{Rq}^\dagger c_{Rq}) \,, \tag{4.8}$$

where $c_{lq}^\dagger$ creates an electron in the state $|lq\rangle$ in lead l. The Hamiltonian of the coupling between the wire and the leads is

$$H_{\text{contacts}} = \sum_q (V_{Lq} c_{Lq}^\dagger c_1 + V_{Rq} c_{Rq}^\dagger c_N) + \text{h.c.} \,. \tag{4.9}$$

We define the tunneling spectral density $\Gamma_l(\epsilon)$, for $l = R, L$, given by

$$\Gamma_l(\epsilon) = 2\pi \sum_q |V_{lq}|^2 \delta(\epsilon - \epsilon_q) \,. \tag{4.10}$$

As we are only interested in the effect the driving has on the conductor and not in the details of the coupling to the leads, we work under the wide-band limit, where $\Gamma_l(\epsilon)$ is energy independent.

The net current flowing across the contact of lead l into the conductor is determined by the negative derivative of the electron number in lead l multiplied by the electron charge $-e$. Thus, the current operator reads

$$I_l(t) = e \frac{i}{\hbar} [H(t), N_l] \,, \tag{4.11}$$

where $N_l = \sum_q c_{lq}^\dagger c_{lq}$.

The first step is to solve the equation of motion for the fermionic operators of the leads $c_{lq}(t)$. We pick the left lead, which for the equation of motion of $c_{Lq}(t)$ is written as

$$\dot{c}_{Lq} = -\frac{i}{\hbar} \epsilon_q c_{Lq} - \frac{i}{\hbar} V_{Lq} c_1 \,. \tag{4.12}$$

Integrating this equation we obtain

$$c_{Lq}(t) = e^{-i\epsilon(t-t_0)/\hbar} c_{Lq}(t_0) - \frac{i}{\hbar} V_{Lq} \int_0^{t-t_0} \mathrm{d}\tau \; e^{-i\epsilon\tau/\hbar} c_1(t-\tau) \,. \tag{4.13}$$

The case for the right lead is analogous, just replace L by R and c_1 by c_N. Using this result, one can show that the equation of motion for the operator c_1 is given by

$$\dot{c}_1 = -\frac{i}{\hbar}\sum_{n'} H_{1n'}c_{n'}(t) - \frac{1}{\hbar}\int_0^{t-t_0} \mathrm{d}\tau\ \Gamma_L(\tau)c_L(t-\tau) + \xi_L(t)\,, \tag{4.14}$$

where $\Gamma_L(t)$ is the Fourier transform of the spectral density (4.10) and

$$\xi_l(t) \equiv -\frac{i}{\hbar}\sum_q V_{lq}^* e^{-i\epsilon_q(t-t_0)/\hbar} c_{lq}(t_0) \tag{4.15}$$

is the Gaussian noise operator, with expectation values

$$\langle \xi_l(t)\rangle = 0\,, \tag{4.16}$$

$$\langle \xi_{l'}^\dagger(t')\xi_l(t)\rangle = \delta_{ll'}\int \frac{\mathrm{d}\epsilon}{2\pi\hbar^2}\ e^{-\frac{i}{\hbar}\epsilon(t-t')}\Gamma_l(\epsilon)f_l(\epsilon)\,, \tag{4.17}$$

while in the Fourier representation of the gaussian noise operator

$$\xi_l(\epsilon) = \int \mathrm{d}t\ e^{i\epsilon t/\hbar}\xi_l(t) \tag{4.18}$$

the correlation function is

$$\langle \xi_{l'}^\dagger(\epsilon')\xi_l(\epsilon)\rangle = 2\pi\Gamma_l(\epsilon)f_l(\epsilon)\delta_{ll'}\,. \tag{4.19}$$

The solution of (4.14) can be written in terms of the retarded Green function defined by

$$\mathcal{G}(t,t') = -\frac{i}{\hbar}\Theta(t-t')U(t,t') \tag{4.20}$$

which obeys

$$\left[i\hbar\frac{\mathrm{d}}{\mathrm{d}t} - H(t)\right]\mathcal{G}(t,t') + i\int_0^{+\infty}\mathrm{d}\tau\ \Gamma(\tau)\mathcal{G}(t-\tau,t') = \delta(t-t')\,, \tag{4.21}$$

with $\Gamma(t) = |1\rangle\Gamma_L\delta(t)\langle 1| + |N\rangle\Gamma_R\delta(t)\langle N|$ in the wide-band limit. Taking the asymptotic limit $t_0 \to -\infty$ the fermionic operator c_1 for a generic time is given by

$$c_1(t) = i\hbar\sum_l\int_0^{+\infty}\mathrm{d}\tau\ \mathcal{G}_{1,n_l}(t,t-\tau)\xi_l(t-\tau) = \frac{i}{2\pi}\sum_l\int \mathrm{d}\epsilon\ e^{-i\epsilon t/\hbar}\mathcal{G}_{1,n_l}(t,\epsilon)\xi_l(\epsilon)\,, \tag{4.22}$$

where we used the representation

$$\mathcal{G}(t,\epsilon) = -\frac{i}{\hbar}\int_0^{+\infty}\mathrm{d}\tau\ e^{i\epsilon\tau/\hbar}U(t,t-\tau)\,, \tag{4.23}$$

and $n_L = 1, n_R = N$. Due to time-periodicity of the Hamiltonian the previous Green function is periodic in time with period T, so it admits the Fourier series

$$\mathcal{G}(t,\epsilon) = \sum_n e^{-in\Omega t}\mathcal{G}^{(n)}(\epsilon)\,, \tag{4.24}$$

with the coefficients given by

$$\mathcal{G}^{(n)}(\epsilon) = \frac{1}{T}\int_0^T \mathrm{d}t\; e^{in\Omega t}\mathcal{G}(t,\epsilon)\,. \tag{4.25}$$

From the definition of the current operator, we compute the current operator at the left lead by doing the commutator between the number operator $N_L = \sum_q c_{Lq}^\dagger c_{Lq}$ and the Hamiltonian (4.6). From the definition (4.11) and using Eqs. (4.13) and (4.15) one obtains

$$I_L(t) = \frac{e}{\hbar}\int_0^{+\infty} \mathrm{d}\tau\;\left[\Gamma_L(\tau)c_1^\dagger(t)c_1(t-\tau) + \Gamma_l^*(\tau)c_1^\dagger(t-\tau)c_1(t)\right] - e\left[c_1^\dagger(t)\xi_L(t) + \xi_L^\dagger(t)c_1(t)\right]\,. \tag{4.26}$$

From this operator we can compute expectation values to extract the dc current and the noise, but we are only interested in the former. To compute the quantum average of the current we need to insert (4.22) into (4.26), and use the correlation function (4.19) to arrive at

$$\langle I_L(t)\rangle = \frac{e}{h}\int \mathrm{d}\epsilon\,\left[T_{LR}(t,\epsilon)f_R(\epsilon) - T_{RL}(t,\epsilon)f_L(\epsilon)\right] - \frac{\mathrm{d}}{\mathrm{d}t}q_L(t)\,, \tag{4.27}$$

where

$$q_L(t) = \frac{e}{2\pi}\int \mathrm{d}\epsilon \sum_n |\mathcal{G}_{n1}(t,\epsilon)|^2\Gamma_L(\epsilon)f_L(\epsilon) \tag{4.28}$$

and

$$T_{LR}(t,\epsilon) = 2\Re\left\{\int_0^\infty \mathrm{d}\tau\; e^{i\tau\epsilon/\hbar}\Gamma_L(\tau)\mathcal{G}_{1N}^*(t,\epsilon)\mathcal{G}_{1N}(t-\tau,\epsilon)\Gamma_R(\epsilon)\right\}\,, \tag{4.29}$$

which represents the probability that an electron coming from the right lead with energy ϵ is located at the left lead at the final instant t. The expression and interpretation for $T_{RL}(t,\epsilon)$ is analogous.

The dc current is obtained from doing the time-average of (4.27). The second term does not contribute since it is time-periodic and bounded, so we only need to worry about the first one. By replacing the Green function in (4.29) with its Fourier expansion and doing the average in time we obtain

$$T_{LR}(\epsilon) \equiv \frac{1}{T}\int_0^T \mathrm{d}t\; T_{LR}(t,\epsilon) = \sum_n \Gamma_L(\epsilon+\hbar n\Omega)\Gamma_R(\epsilon)|\mathcal{G}_{1N}^{(n)}(\epsilon)|^2 \equiv \sum_n T_{LR}^{(n)}(\epsilon)\,. \tag{4.30}$$

At last, the expression for the time-average current is

$$\bar{I} = \frac{e}{h}\sum_{n\in\mathbb{Z}}\int \mathrm{d}\epsilon\,\left[T_{LR}^{(n)}(\epsilon)f_R(\epsilon) - T_{RL}^{(n)}(\epsilon)f_L(\epsilon)\right]\,, \tag{4.31}$$

where $T_{RL}^{(n)}(\epsilon)$ is the probability that an electron coming from the left lead with initial energy ϵ absorbs(emits) $n(-n)$ photons and ends up with energy $\epsilon + \hbar n\Omega$ in the right lead. $T_{LR}^{(n)}(\epsilon)$ has a similar interpretation.

The current (4.31) in the form

$$\bar{I} = \frac{e}{h} \int \mathrm{d}\epsilon \, [T_{LR}(\epsilon) f_R(\epsilon) - T_{RL}(\epsilon) f_L(\epsilon)] \tag{4.32}$$

resembles expression (4.2). The striking difference is that in the static case processes involving emission and absorption of photons have zero probability, so that T_{LR} equals T_{RL}. One direct consequence is that when the bias is zero the left and right distribution function match, and the average current is identically null. This is in general not true in the driven case, where for zero bias we can have non-zero current if $T_{RL} \neq T_{LR}$. This kind of pumping effect is allowed under breaking of certain symmetries of the system that will be discussed thoroughly later in this work.

Recall we are dealing with an open system, with TDSE

$$i\hbar\partial_t |\psi(t)\rangle = [H(t) + \Sigma] |\psi(t)\rangle \,, \tag{4.33}$$

just like in Eq. (2.45), where

$$\Sigma = -i \left[|1\rangle \frac{\Gamma_L}{2} \langle 1| + |N\rangle \frac{\Gamma_R}{2} \langle N| \right] = \begin{bmatrix} -i\frac{\Gamma_L}{2} & 0 & \dots & 0 \\ 0 & 0 & & \vdots \\ \vdots & \ddots & \ddots & 0 \\ 0 & \dots & 0 & -i\frac{\Gamma_R}{2} \end{bmatrix} \tag{4.34}$$

is the self energy $\Sigma_R + \Sigma_L$ from Eq. (2.45), which comes from the coupling of the chain to the leads, and

$$H(t) = H_0 + H_1 e^{i\Omega t} + H_1^\dagger e^{-i\Omega t} \tag{4.35}$$

is the Hamiltonian of the chain plus driving. Here all operators are in real space, being thus $N \times N$ matrices. In this way the Floquet equation for both right eigenvectors (2.46) and for left eigenvectors (2.47) holds. The spectral representation of the non-unitary time-evolution operator (2.49) is valid as well.

From the representation of the Green function as in (4.23), the spectral representation of the time-evolution operator (2.49) and the Fourier expansion of the left and right eigenvectors appearing in (2.49), the Fourier components of the Green function as per (4.25) are given by

$$\mathcal{G}^{(n)}(\epsilon) = \sum_{\alpha \in \mathsf{FZ}} \sum_{m \in \mathbb{Z}} \frac{|u_{\alpha,n+m}\rangle \langle u^+_{\alpha,m}|}{\epsilon - (\bar{\epsilon}_\alpha + \hbar m \Omega)} \,, \tag{4.36}$$

where the sum in α is over the quasi-energies in the Floquet zone, that is, those which satisfy $-\hbar\Omega/2 < \Re(\bar{\epsilon}_\alpha) < \hbar\Omega/2$. To determine the vectors $|u_{\alpha,n}\rangle$ we need to diagonalize the matrix representing the Floquet Hamiltonian in the frequency domain, which according to (2.41) is

$$\mathbb{K} = \begin{bmatrix} \ddots & H_1 & 0 & 0 & 0 & 0 & \dots \\ H_1^\dagger & H_0+\Sigma+2\Omega\mathbb{1} & H_1 & 0 & 0 & 0 & \dots \\ 0 & H_1^\dagger & H_0+\Sigma+\Omega\mathbb{1} & H_1 & 0 & 0 & \dots \\ 0 & 0 & H_1^\dagger & H_0+\Sigma & H_1 & 0 & \dots \\ 0 & 0 & 0 & H_1^\dagger & H_0+\Sigma-\Omega\mathbb{1} & H_1 & \dots \\ 0 & 0 & 0 & 0 & H_1^\dagger & H_0+\Sigma-2\Omega\mathbb{1} & H_1 \\ \vdots & \vdots & \vdots & \vdots & \vdots & H_1^\dagger & \ddots \end{bmatrix} . \quad (4.37)$$

The vectors $\langle u^+_{\alpha,n}|$ are obtained through diagonalization of the transpose of $\mathbb{K}$, as discussed in subsection 2.2.6.

Now we have all the information to be able to compute the average current (4.31). From now on we assume zero temperature, so that the distribution functions in the expression for the current are step-functions. Since we are working in the wide-band limit the coupling functions appearing in the transmission coefficients $T^{(n)}_{LR}$ and $T^{(n)}_{RL}$ are constants and factor out of the integral. In this way the integral in (4.31) can be done analitically, so that the final expression for the current is

$$\begin{aligned} \bar{I} = \frac{e}{h}\Gamma_L\Gamma_R \sum_{n\in\mathbb{Z}} \sum_{\alpha,\beta\in \mathsf{FZ}} \sum_{m,m'\in\mathbb{Z}} \frac{\langle 1|u_{\alpha,m+n}\rangle\langle u^+_{\alpha,m}|N\rangle\langle 1|u_{\beta,m'+n}\rangle^*\langle u^+_{\beta,m'}|N\rangle^*}{\bar{\epsilon}_\alpha - \bar{\epsilon}^*_\beta + (m-m')\hbar\Omega} \times \\ \times \left\{ \ln\left[\frac{\mu_R - (\bar{\epsilon}_\alpha + m\hbar\Omega)}{-\infty - (\bar{\epsilon}_\alpha + m\hbar\Omega)}\right] - \ln\left[\frac{\mu_R - (\bar{\epsilon}^*_\beta + m'\hbar\Omega)}{-\infty - (\bar{\epsilon}^*_\beta + m'\hbar\Omega)}\right] \right\} - 1 \leftrightarrow N, L \leftrightarrow R\,. \end{aligned} \quad (4.38)$$

As we did in the static case, the current as a function of the chemical potentials $\bar{I}(\mu_R, \mu_L)$, given by (4.31), can be linearized to give place to the differential conductance, which must be defined with care. For instance, consider the situation where we keep the chemical potential of the left lead at E[1], and raise the chemical potential of the right lead to $E + dE$, where $0 < dE \ll |E|$. The bias is thus $\delta V = dE/e$. In the zero temperature approximation the differential conductance, denoted by G_{LR}, is given by

$$\begin{aligned} G_{LR}(E) = \frac{\delta\bar{I}}{\delta V} = \frac{\bar{I}(E+dE,E) - \bar{I}(E,E)}{\delta V} = \\ = \frac{e}{h}\frac{1}{dE/e}\sum_{n\in\mathbb{Z}}\int \mathrm{d}\epsilon\, [T^{(n)}_{LR}(\epsilon)\Theta(E+dE-\epsilon) - T^{(n)}_{RL}(\epsilon)\Theta(E-\epsilon) - T^{(n)}_{LR}(\epsilon)\Theta(E-\epsilon) + T^{(n)}_{RL}(\epsilon)\Theta(E-\epsilon)] = \\ = \frac{e^2}{h}\frac{1}{dE}\sum_{n\in\mathbb{Z}}\int \mathrm{d}\epsilon\, T^{(n)}_{LR}(\epsilon)\underbrace{[\Theta(E+dE-\epsilon) - \Theta(E-\epsilon)]}_{\Theta'(E-\epsilon)dE} = \\ = \frac{e^2}{h}\sum_{n\in\mathbb{Z}} T^{(n)}_{LR}(E) = \frac{e^2}{h}\Gamma_L\Gamma_R\sum_{n\in\mathbb{Z}}|\mathcal{G}^{(n)}_{1N}(E)|^2 = \frac{e^2}{h}T_{LR}(E)\,. \end{aligned} \quad (4.39)$$

[1]The chemical potential is mostly denoted by the greek letter μ. However, it appears in the definition of the zx model, so we choose to denote the chemical potential by E.

If we keep the chemical potential of the right lead at $\mu_R = E$ and lower the one of the left lead to $\mu_L = E - dE$, then the differential conductance, now denoted by G_{RL}, is

$$G_{RL}(E) = \frac{\delta \bar{I}}{\delta V} = \frac{\bar{I}(E, E - dE) - \bar{I}(E, E)}{dE/e} = \frac{e^2}{h} \sum_{n \in \mathbb{Z}} T_{RL}^{(n)}(E) = \frac{e^2}{h} \Gamma_L \Gamma_R \sum_{n \in \mathbb{Z}} |\mathcal{G}_{N1}^{(n)}(E)|^2 = \frac{e^2}{h} T_{RL}(E) \,. \tag{4.40}$$

If instead we apply a bias around a given chemical potential E, where $\mu_L = E - dE/2$ and $\mu_R = E + dE/2$, then the differential conductance, now denoted by G, is

$$G(E) = \frac{e^2}{2h} [T_{LR}(E) + T_{RL}(E)] = \frac{G_{LR}(E) + G_{RL}(E)}{2} \,. \tag{4.41}$$

Contrary to the static case, we have more than one differential conductance, since $T_{LR}(E) \neq T_{RL}(E)$ in general. As it will be useful later, we define the derivative of the current at zero bias, where the leads are at the same chemical potential μ_l, with respect to μ_l as

$$\bar{I}'(\mu_l) = \frac{\bar{I}(\mu_l + \delta\mu_l, \mu_l + \delta\mu_l) - \bar{I}(\mu_l, \mu_l)}{\delta\mu_l} \,, \tag{4.42}$$

which after a simple algebra yields

$$\bar{I}'(\mu_l) = \frac{e}{h} \sum_{n \in \mathbb{Z}} \left[T_{RL}^{(n)}(\mu_l) - T_{LR}^{(n)}(\mu_l) \right] = \frac{e^2}{h} \Gamma_L \Gamma_R \sum_{n \in \mathbb{Z}} \left[|\mathcal{G}_{N1}^{(n)}(\mu_l)|^2 - |\mathcal{G}_{1N}^{(n)}(\mu_l)|^2 \right] \,. \tag{4.43}$$

Chapter 5

Transport through driven systems

In this chapter we present the main results of this work.

In the first section, we establish what are the topology signatures in the transport properties of one dimensional Floquet systems. We look at the average current through a driven SSH chain, taking into account the phase diagram of the system based in the topology of the first order Magnus Hamiltonian. Then, we move to the zx model, whose phase diagram was already obtained in section 3.3.2. We see what happens with the transmission properties when two halves of the chain are illuminated with different driving field amplitudes.

Additionally, we wish to know how symmetries influence the charge and heat pumping. In the second section we explain the even/odd behavior of the charge pumping with the chemical potential based on the symmetries present in the system in homogeneous and inhomogeneous chains of the zx model. We also make considerations on the xy model yet to be defined.

At last, in the third section we explain the even/odd behavior of the heat pumping based on the symmetries present, just as we did for the charge pumping. We consider homogeneous and inhomogeneous chains of both zx and xy models.

5.1 Topology and Transport

5.1.1 Driven SSH model

In this section we will study a model which is a driven version of the SSH model. The Floquet-Bloch Hamiltonian is

$$H(k,t) = H_0(k) + H_1(k)e^{i\Omega t} + H_1^\dagger(k)e^{-i\Omega t}\,, \tag{5.1}$$

where

$$H_0(k) = \begin{bmatrix} 0 & t_1 + t_2 e^{-ik} \\ t_1 + t_2 e^{ik} & 0 \end{bmatrix} = (t_1 + t_2\cos k)\ \sigma_x + t_2 \sin k\ \sigma_y \tag{5.2}$$

is the SSH model Hamiltonian, $H_1(k) = A(i\sigma_y + \sigma_z)$ and the hopping amplitudes are real. This Hamiltonian enjoys only TRS, with $T = \mathbb{1}$ and $T^*T = \mathbb{1}$. Consulting Table 3.2, we see it belongs to the AI symmetry class, which in one dimension has no winding number. However, the effective Magnus Hamiltonian in first order ($\hbar = 1$) given by

$$H_{\text{eff}}(k) = H_0(k) + \frac{1}{\Omega}[H_1(k), H_1^{\dagger}(k)] = H_0(k) - \frac{4A^2}{\Omega}\sigma_1 = (t_1^{\text{eff}} + t_2 \cos k)\, \sigma_x + t_2 \sin k\, \sigma_y \tag{5.3}$$

is a static SSH Hamiltonian, with hopping parameters $t_1^{\text{eff}} = t_1 - 4A^2/\Omega$ and t_2. Thus, we have a winding number for the Magnus Hamiltonian which is zero if $|t_1^{\text{eff}}| > |t_2|$ and one if $|t_1^{\text{eff}}| < |t_2|$. In Fig. 5.1 we have the phase diagram of this model, according to the Magnus Hamiltonian. We can see that the driving may induce non-trivial topology even when the static system is trivial. The contrary also happens, that is, the driving can take the system from a topological phase to a non-topological one.

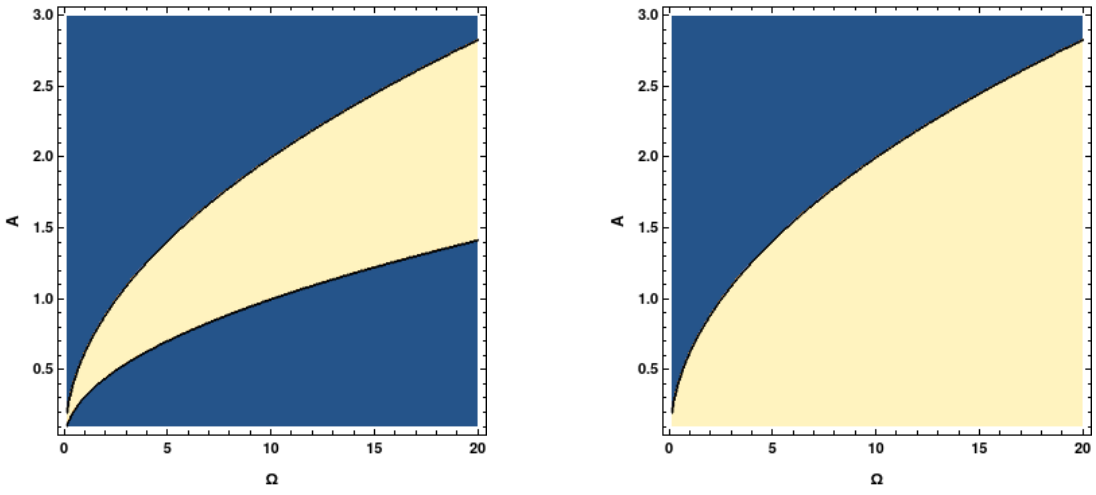

(a) $t_1 = 1, t_2 = 0.6$ (b) $t_1 = 0.6, t_2 = 1$

Figure 5.1: Phase diagram of the effective first order Magnus Hamiltonian of the driven SSH model. Blue: $\nu = 0$; White: $\nu = 1$.

In Fig. 5.2 the average current is plotted against the driving amplitude while fixing all the other parameters. Note that the hopping amplitudes were chosen according to the choosed ones for the phase diagrams in Fig. 5.1

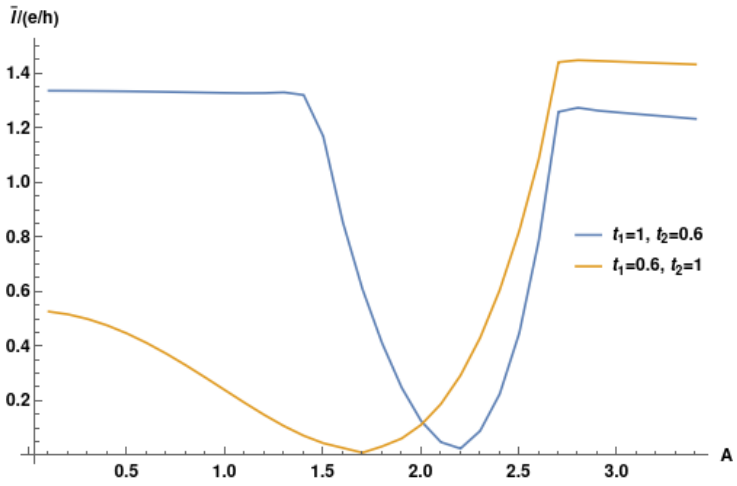

Figure 5.2: Average current through the driven SSH chain as a function of A. $\Omega = 20$, $\Gamma_L = \Gamma_R = 0.5$, $\mu_R = -\mu_L = 25$. 80 sites.

We can see in these plots transitions between topological phases. For the case of Fig. 5.1a (plot in blue of Fig. 5.2) the average current behaves monotonically for $A \lesssim 1.4$ and for $A \gtrsim 2.7$, while for $1.4 \lesssim A \lesssim 2.7$ the current decreases and then increases. In the case of Fig. 5.1b (plot in yellow of Fig. 5.2) we see only one transition around $A \approx 2.7$. For $A \lesssim 2.7$ the average current first decreases and then increases until it reaches the transition point. From that point on the current behaves monotonically. Looking at Fig. 5.1 we see that these transitions occur when the value of the winding number changes. We can look at the quasienergy spectrum to search for zero-energy edge modes. In Fig. 5.3a we have two zero-energy states in the spectrum, while in Fig. 5.3b we have no zero-energy states. This is in accordance with the phase diagram of Fig. 5.1a. The zero-energy modes of Fig. 5.3a are represented in Fig. 5.4a, which are localized on the edges of the chain. Nonetheless, one must take care when reading the phase diagrams of Fig. 5.1, since the Magnus expansion only makes sense for high frequencies. For mid-range and low frequencies the phase diagrams have no meaning. Furthermore, we are using a winding number best suited for static systems. So the winding number of the effective Hamiltonian does not capture the full picture. Additionally, this winding does not predict the existence of π-modes. As this model has no (dynamic) winding number, in the next section we move on to a model which does.

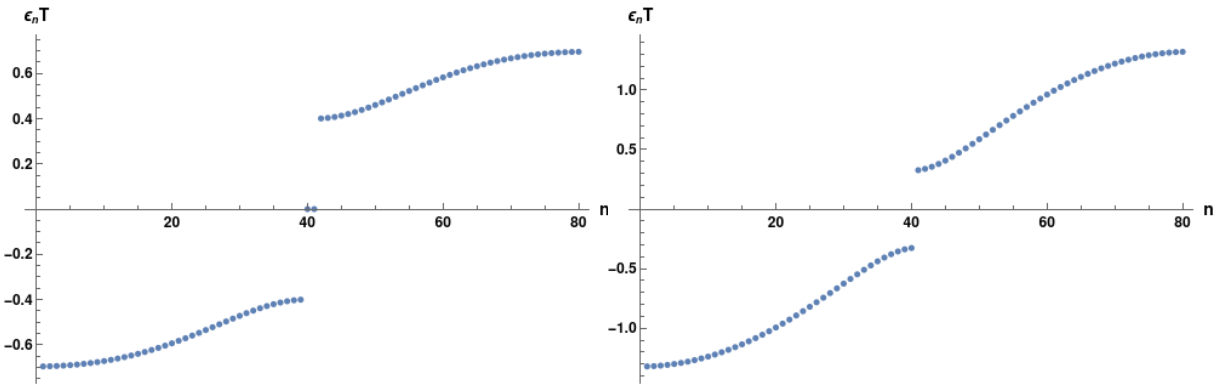

(a) $A = 2$ (b) $A = 3$

Figure 5.3: Quasienergies in the Floquet zone. $t_1 = 1$, $t_2 = 0.6$, $\Omega = 20$. 80 sites.

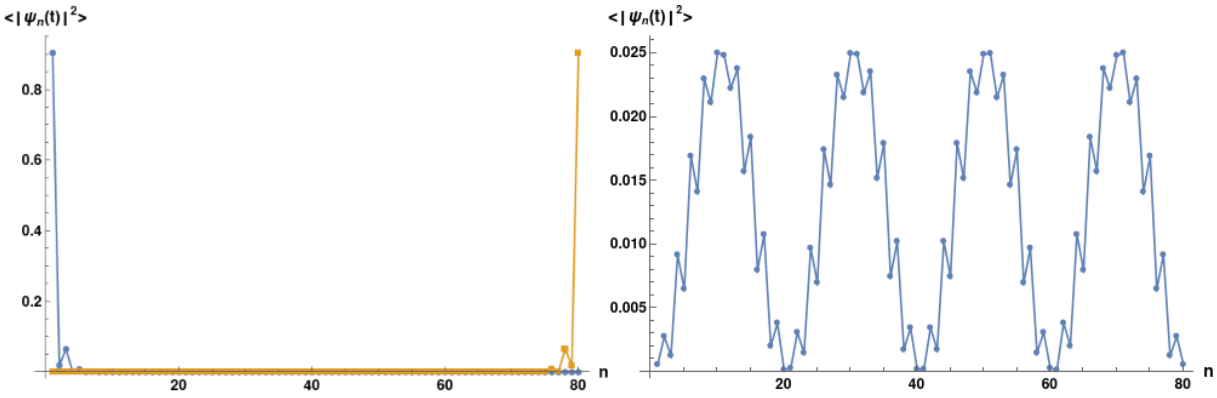

(a) $\epsilon = 0$ (b) $\epsilon = 0.413487$

Figure 5.4: Time-averaged probability density of states picked from the Floquet zone of Fig. 5.3a. (a) Localized modes. (b)One bulk mode, to compare with the localized ones.

5.1.2 zx model

We have seen in Chapter 3 that in the thermodynamic limit non-trivial topological phases, according to the bulk-edge correspondence, are characterized by the presence of robust states localized at the interfaces separating different phases. The quasienergy of those states lies at either $\varepsilon = 0$ or $\varepsilon = \pi$ for chiral systems. As explained by O. Balabanov and H. Johannesson in [13], when the length of the topological insulator is finite, the topological states hybridize with bulk states and create additional transport channels across the structure. Thus a fingerprint of those states we expect to see is the existence of transmission peaks at the chemical potentials 0 whenever $\nu_0 \neq 0$ or at $\pm\pi/T$ whenever $\nu_\pi \neq 0$ for homogeneous chains. Given the modulo 2π ambiguity of the quasienergies, besides the peak at 0 when $\nu_0 \neq 0$, we expect to see additional peaks at chemical potentials $2n\pi$, $n \in \mathbb{Z}$. When $\nu_\pi \neq 0$ we expect to have peaks at $(2n+1)\pi$, $n \in \mathbb{Z}$. We have access to the transmission peaks since in experiments we can measure the differential conductance, which is related to the transmission coefficients through Eqs. (4.39), (4.40) and (4.41). Similarly to [13], we plot the transmission coefficients against the chemical potential for distinct topological phases of the zx model defined in (3.61).

We can see from Fig. 5.5 that peaks appear within the gaps, whenever the chiral invariant is non-zero for that gap. We chose a small number of sites since according to Johannesson and Balabanov [13] the transmission peaks within the gaps are more prominent for smaller chains. Nonetheless, the work of Johannesson and Balabanov shows that the growth of the peaks is not monotonic with the chain size.

In this work we see what happens when the chain is inhomogeneous. First we consider the case of Fig. 3.18, where the left side of the chain is in the phase $(1, 0)$ and the the right one is in the phase $(-1, 0)$, such that we have four zero-energy bound states in total. We can see in Fig. 5.6 that the transmission peak of the inhomogeneous chain survives for bigger chain sizes than the ones of the homogeneous chains.

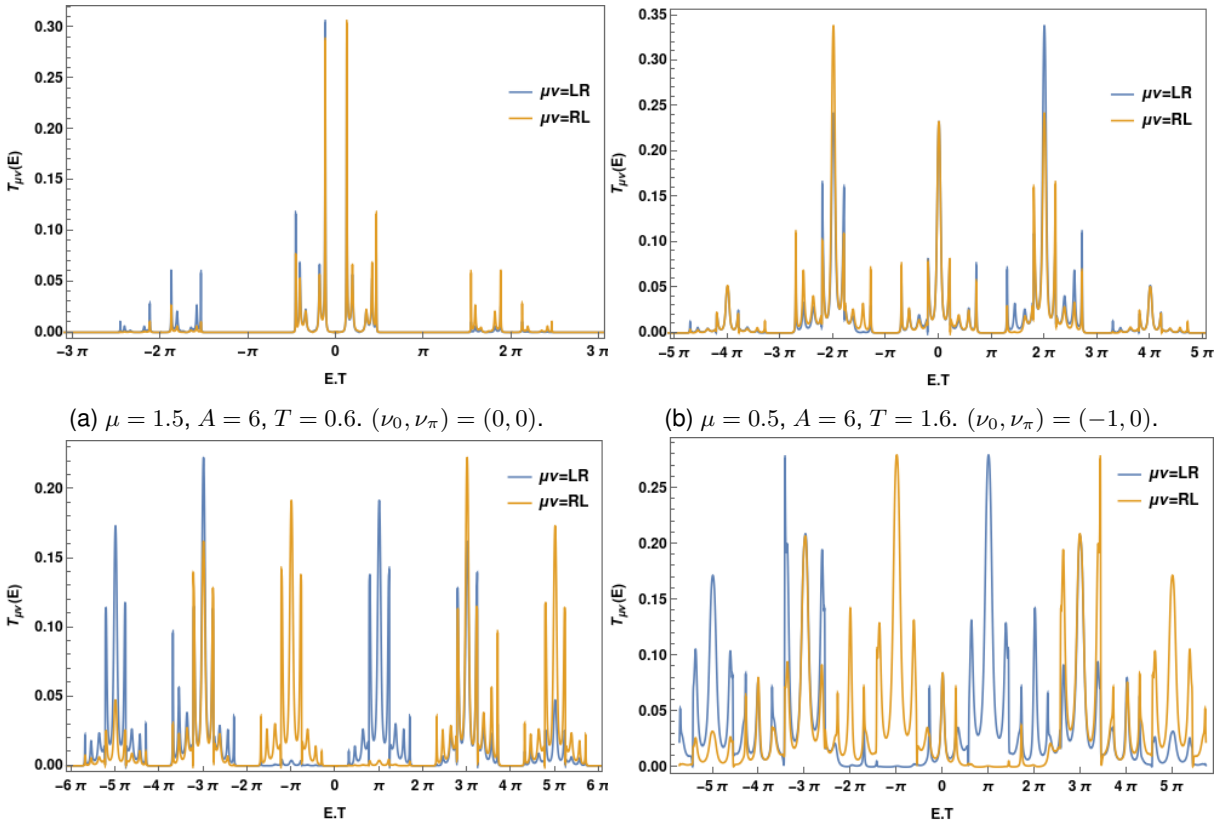

(a) $\mu = 1.5$, $A = 6$, $T = 0.6$. $(\nu_0, \nu_\pi) = (0, 0)$.

(b) $\mu = 0.5$, $A = 6$, $T = 1.6$. $(\nu_0, \nu_\pi) = (-1, 0)$.

(c) $\mu = 1.5$, $A = 10$, $T = 1.6$. $(\nu_0, \nu_\pi) = (0, -1)$.

(d) $\mu = 1.5$, $A = 5$, $T = 3$. $(\nu_0, \nu_\pi) = (1, -1)$.

Figure 5.5: Transmission coefficients for different phases of the zx model. $\Gamma_L = \Gamma_R = 0.5$. 12 sites.

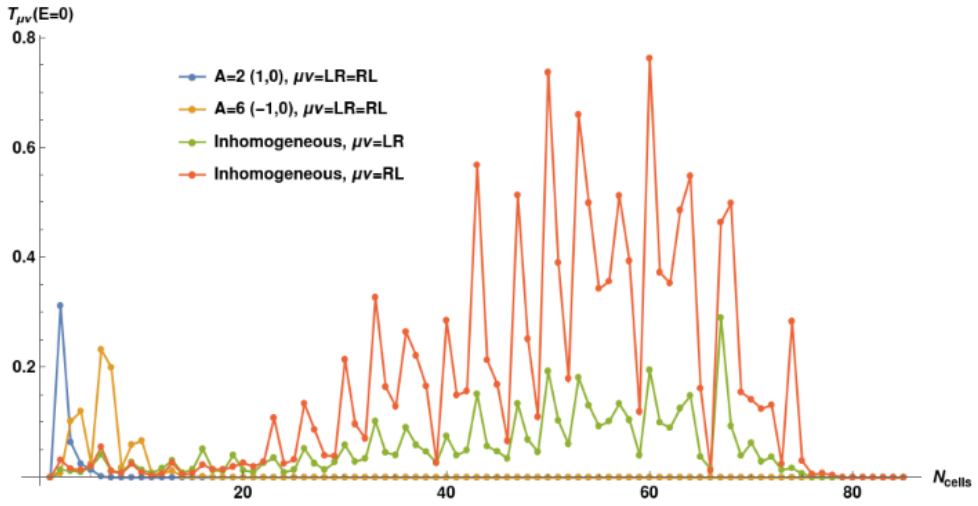

Figure 5.6: Transmission peaks at zero chemical potential as a function of the number of unit cells, for homogeneous and inhomogeneous chains. Note that for the homogeneous chains $T_{LR}(0) = T_{RL}(0)$. $\mu = 0.5$, $T = 1.6$, $\Gamma_L = \Gamma_R = 0.5$, $A_L = 2$, $A_R = 6$.

To see what happens to the transmission peaks at $\pm\pi$ energies we will use the example from Fig. 3.19 of section 3.4, which has four π-modes. Now we have to look for peaks at the chemical potentials $-\pi$ and π. We see from Fig. 5.7 that the peaks at $\pm\pi$ of the inhomogeneous chain survive for bigger chain sizes compared to the homogeneous cases, except for $T_{LR}(-\pi/T)$ of Fig. 5.7c. Nonetheless, we note that for inhomogeneous chains the peaks at zero chemical potential survive for bigger

chain sizes compared to the peaks at $\pm\pi$.

The conclusion to make is that additional bound states enhance the conductivity, since there are more states which through tunnel effect occurs.

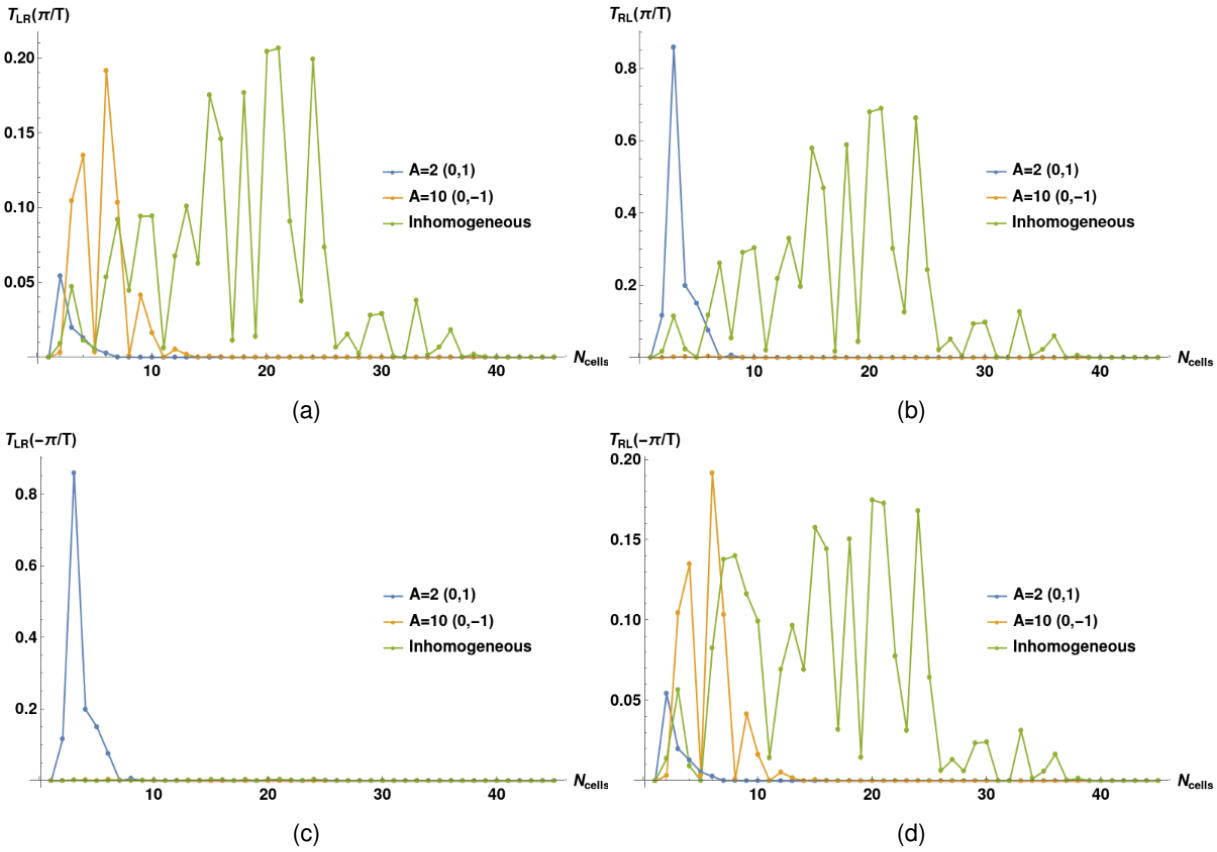

Figure 5.7: Transmission peaks at chemical potentials $\pm\pi$ as a function of the number of unit cells, for homogeneous and inhomogeneous chains. (a) Left-right transmission coefficient at π. (b) Right-left transmission coefficient at π. (c) Left-right transmission coefficient at $-\pi$. (d) Right-left transmission coefficient at $-\pi$. $\mu = 1.5$, $T = 1.6$, $\Gamma_L = \Gamma_R = 0.5$, $A_L = 2$, $A_R = 10$.

5.2 Symmetries and Transport

A dc current is usually associated to a dissipative flow of the electrons in response to an applied bias voltage. Nonetheless, electrical transport at nanoscopic and mesoscopic scales can occur with no dissipation, as discussed in the beginning of Chapter 3. Other interesting feature of transport at those scales is having net flow of charge at zero bias. This is a quantum coherent effect called quantum charge pumping and is the subject of this section. Quantum charge pumping, or simply charge pumping, is of both theoretical [16, 20, 37, 38] and experimental [39] interest.

The necessary condition to have charge pumping is the breaking of the left-right symmetry (LRS) of the system, which can be done by breaking either parity (or spatial) symmetry (PS) or TRS [19, 20], this in the driven case. The static case is insensitive to symmetry breaking. The net charge current is always zero for zero bias.

We define PS in one dimension as: there exists an unitary matrix P such that

$$H(k,t) = PH(-k,t)P^\dagger\,, \text{ in momentum space,} \tag{5.4}$$

$$H(-x,t) = PH(x,t)P^\dagger\,, \text{ in real space.} \tag{5.5}$$

It acts on the wave-function as follows. At the unit cell x the wave-function ψ is the spinor $\psi(x)$. If for example $x = (|1\rangle, |2\rangle)$, then $-x = (|N-1\rangle, |N\rangle)$, N being the number of atom sites. Then the matrix P is such that $P\psi(-x) = \psi(x)$. This makes $\langle 1|\psi\rangle = \langle N-1|P\psi\rangle$, with P acting in real space. We will use the same symbol whenever the matrix is operating in momentum space or real space. We apply this to other matrices as well.

For the zx model given by (3.61), $P = \sigma_z$. Note however that the Hamiltonian now includes the self-energy

$$\Sigma = -\frac{i}{2}[\Gamma_L|1\rangle\langle 1| + \Gamma_R|N\rangle\langle N|]\,, \tag{5.6}$$

so when we check if the Hamiltonian satisfies a given symmetry we have to account for the chain Hamiltonian and the self-energy. The self-energy breaks PS because

$$P\Sigma(-x)P^\dagger = -\frac{i}{2}\sigma_z[\Gamma_L|N-1\rangle\langle N-1| + \Gamma_R|2\rangle\langle 2|]\sigma_z = -\frac{i}{2}[\Gamma_L|N-1\rangle\langle N-1| + \Gamma_R|2\rangle\langle 2|] \neq \Sigma(x)\,. \tag{5.7}$$

So we expect to have charge pumping for the homogeneous zx chain. If the chain is inhomogeneous, then it is certain that PS is broken. To see that in both cases we have charge pumping, we show in Fig. 5.8 a plot of the average net charge pumped in one cycle, Q (in units of $e/\hbar\Omega$), at zero bias, as a function of the chemical potential of the leads, μ_l. Q is simply the average current $\bar{I}(\mu_l, \mu_l)$ given by (4.31) multiplied by the period T.

One interesting feature of the plots from Fig. 5.8 is that the pumped charge is an even function of the chemical potential for the homogeneous case. We can look at the transmission probabilities $|\mathcal{G}^{(m)}_{\alpha\beta}(E)|^2 \equiv |\mathcal{G}_{\alpha\beta}(m,E)|^2$ to search for symmetries that explain the results of Fig. 5.8.

In Fig. 5.9 the transmission probability $|\mathcal{G}^{(m)}_{\alpha\beta}(E)|^2$ is plotted against the chemical potential, for different values of m, and $\alpha\beta = 1N, N1$. $|\mathcal{G}^{(m)}_{\alpha\beta}(E)|^2$ represents the probability for an electron to leave lead β with energy E and absorb($m > 0$)/emit($m < 0$) $|m|$ photons and enter lead α with energy $E + m\hbar\Omega$. From the panels of Fig. 5.9 we can infer that

$$|\mathcal{G}^{(m)}_{1N}(E)|^2 = |\mathcal{G}^{(-m)}_{N1}(E + m\hbar\Omega)|^2\,. \tag{5.8}$$

This relation is implied by TRS [12], which is present in our model, since the self-energy verifies $\sigma_x\Sigma^{\mathsf{T}}\sigma_z = \Sigma$. To prove (5.8) we look at the Floquet equation which reads

$$i\hbar\partial_t|u_\epsilon(t)\rangle = [H(t) + \Sigma - \epsilon]|u_\epsilon(t)\rangle\,, \tag{5.9}$$

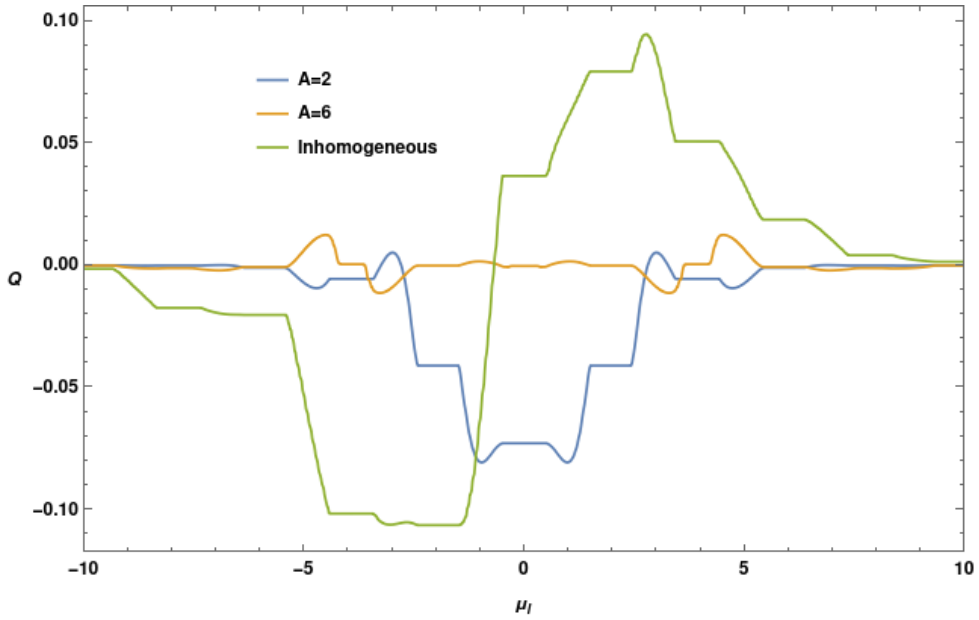

Figure 5.8: Pumped charge over a period as a function of the chemical potential, for homogeneous and inhomogeneous chains of the zx model. $\mu = 0.5$, $T = 1.6$, $\Gamma_L = \Gamma_R = 0.5$, $A_L = 2$, $A_R = 6$. 60 sites.

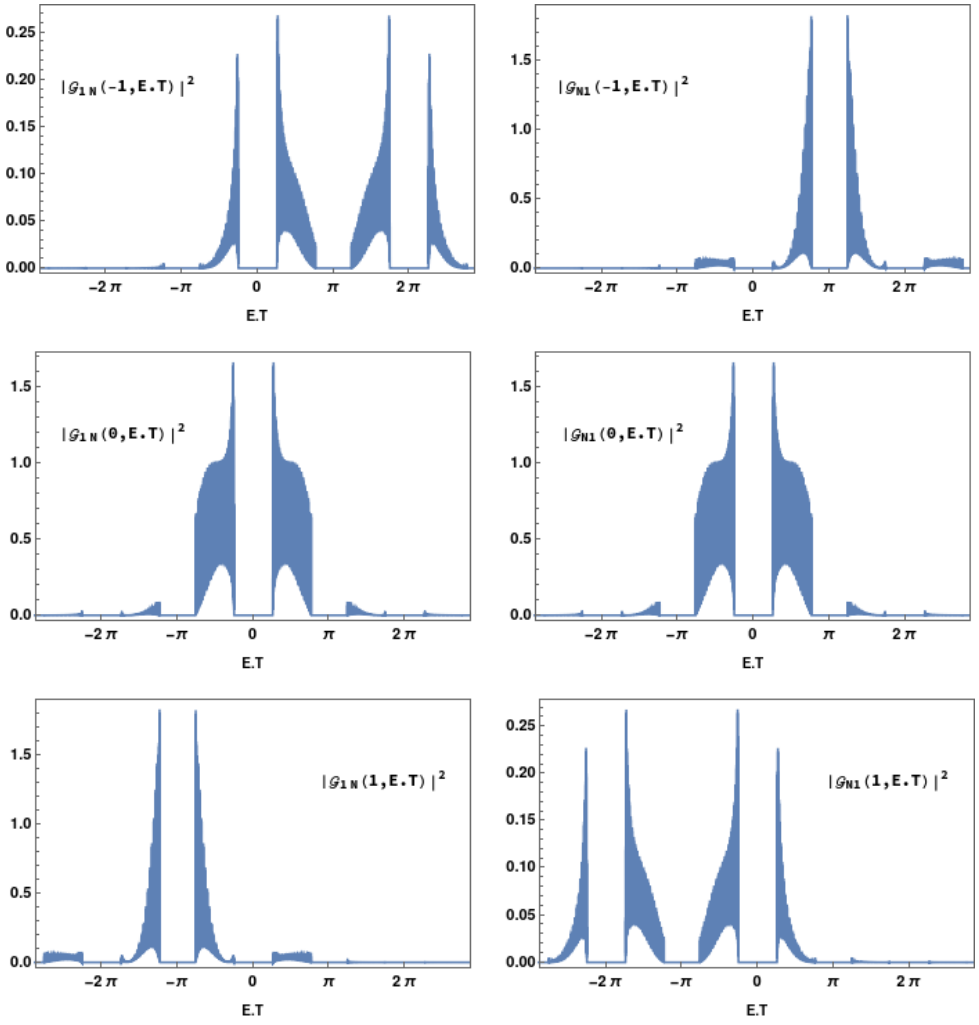

Figure 5.9: Plot of $|\mathcal{G}_{\alpha\beta}(m, E.T)|^2$ against the (adimensional) chemical potential $E.T$, for $m = -1, 0, 1$, $\alpha\beta = 1N, N1$. $\mu = 0.5$,$A = 2$, $T = 1.6$, $\Gamma_L = \Gamma_R = 0.5$. 60 sites.

where we changed the notation used in (2.46) by replacing $u_\alpha \to u_\epsilon$, $\bar{\epsilon}_\alpha \to \epsilon$. By transposing and replacing $t \to -t$ we obtain

$$
\begin{aligned}
i\hbar\left[\partial_t\langle u_\epsilon(t)|^*\right]_{-t} &= \langle u_\epsilon(-t)|^*[H^{\mathsf{T}}(-t)+\Sigma^{\mathsf{T}}-\epsilon] \Leftrightarrow \\
\Leftrightarrow i\hbar\left[\partial_t\langle u_\epsilon(t)|^*\right]_{-t} T^\dagger &= \langle u_\epsilon(-t)|^* T^\dagger T[H^{\mathsf{T}}(-t)+\Sigma^{\mathsf{T}}-\epsilon]T^\dagger \Leftrightarrow \\
\Leftrightarrow -i\hbar\partial_t\langle u_\epsilon(-t)|^* T^\dagger &= \langle u_\epsilon(-t)|^* T^\dagger[H(t)+\Sigma-\epsilon]\,. \qquad (5.10)
\end{aligned}
$$

For the left eigenvector we have

$$
\langle u_\epsilon(-t)|^* T^\dagger = \langle u_\epsilon^+(t)| \Leftrightarrow |u_\epsilon^+(t)\rangle = T|u_\epsilon(-t)\rangle^*\,. \qquad (5.11)
$$

The Fourier series expansion in (2.38a) replacing $u_{\alpha,n} \to u_n(\epsilon)$, reads

$$
|u_\epsilon(t)\rangle = \sum_{n\in\mathbb{Z}} e^{-in\Omega t}|u_n(\epsilon)\rangle\,, \qquad (5.12)
$$

$$
|u_\epsilon^+(t)\rangle = \sum_{n\in\mathbb{Z}} e^{-in\Omega t}|u_n^+(\epsilon)\rangle\,, \qquad (5.13)
$$

that together with relation (5.11) results in

$$
T|u_n(\epsilon)\rangle = |u_n^+(\epsilon)\rangle\,. \qquad (5.14)
$$

As a consequence, we have for the Green function

$$
\begin{aligned}
\mathcal{G}_{1N}^{(m)}(E) &= \sum_{\epsilon\in\mathsf{FZ}}\sum_{n\in\mathbb{Z}} \frac{\langle 1|u_{m+n}(\epsilon)\rangle\langle u_n^+(\epsilon)|N\rangle}{E-\epsilon-\hbar n\Omega} = \sum_{\epsilon\in\mathsf{FZ}}\sum_{n\in\mathbb{Z}} \frac{\langle 1|T^\dagger u_{m+n}^+(\epsilon)\rangle^*\langle T^\dagger u_n(\epsilon)|N\rangle^*}{E-\epsilon-\hbar n\Omega} = \\
&= \sum_{\epsilon\in\mathsf{FZ}}\sum_{n\in\mathbb{Z}} \frac{\langle 1|\sigma_z|u_{m+n}^+(\epsilon)\rangle^*\langle u_n(\epsilon)|\sigma_z|N\rangle^*}{E-\epsilon-\hbar n\Omega} = -\sum_{\epsilon\in\mathsf{FZ}}\sum_{n\in\mathbb{Z}} \frac{\langle N|u_n(\epsilon)\rangle\langle u_{m+n}^+(\epsilon)|1\rangle}{E-\epsilon-\hbar n\Omega} = \\
n+m=p, &= -\sum_{\epsilon\in\mathsf{FZ}}\sum_{p\in\mathbb{Z}} \frac{\langle N|u_{p-m}(\epsilon)\rangle\langle u_p^+(\epsilon)|1\rangle}{E-\epsilon-\hbar p\Omega-\hbar m\Omega} = -\mathcal{G}_{1N}^{(-m)}(E+m\hbar\Omega)\,, \qquad (5.15)
\end{aligned}
$$

which implies (5.8). From Fig. 5.9, we can see that besides (5.8) the relation

$$
|\mathcal{G}_{1N}^{(m)}(E)|^2 = |\mathcal{G}_{N1}^{(-m)}(-E)|^2 \qquad (5.16)
$$

holds as well. From (4.43), the derivative of the charge pumping with respect to the chemical potential is given by

$$
Q'(\mu_l) = \frac{e}{\hbar\Omega}\Gamma_L\Gamma_R\sum_{n\in\mathbb{Z}}\left[|\mathcal{G}_{N1}^{(n)}(\mu_l)|^2 - |\mathcal{G}_{1N}^{(n)}(\mu_l)|^2\right]\,. \qquad (5.17)
$$

If (5.16) holds, then the function (5.17) is odd in the chemical potential:

$$Q'(\mu_l) = \frac{e}{\hbar\Omega}\Gamma_L\Gamma_R \sum_{n\in\mathbb{Z}} \left[|\mathcal{G}^{(n)}_{N1}(\mu_l)|^2 - |\mathcal{G}^{(n)}_{1N}(\mu_l)|^2\right] = \frac{e}{\hbar\Omega}\Gamma_L\Gamma_R \sum_{n\in\mathbb{Z}} \left[|\mathcal{G}^{(-n)}_{1N}(-\mu_l)|^2 - |\mathcal{G}^{(-n)}_{N1}(-\mu_l)|^2\right] = -Q'(-\mu_l)\,. \tag{5.18}$$

This implies that the pumped charge is an even function of the chemical potential, which justifies the symmetry of the curves of Fig. 5.8, in the homogeneous case. We now show that this is a result of the $\mathcal{PC}$ symmetry, the product of the parity ($\mathcal{P}$) and particle-hole ($\mathcal{C}$) symmetries. We have already seen that the zx model has no PS, which is broken by the coupling to the leads. The leads break PHS as well since

$$C\Sigma C^\dagger = -\frac{i}{2}\sigma_x[\Gamma_L|1\rangle\langle 1| + \Gamma_R|N\rangle\langle N|]\sigma_x = -\frac{i}{2}[\Gamma_L|2\rangle\langle 2| + \Gamma_R|N-1\rangle\langle N-1|] \neq -\Sigma\,. \tag{5.19}$$

However, the zx model enjoys the product of PS and PHS because

$$\begin{aligned} PC\Sigma(-x)C^\dagger P^\dagger &= -\frac{i}{2}\sigma_z\sigma_x[\Gamma_L|N-1\rangle\langle N-1| + \Gamma_R|2\rangle\langle 2|]\sigma_x\sigma_z = \\ &= -\frac{i}{2}\sigma_z[\Gamma_L|N\rangle\langle N| + \Gamma_R|1\rangle\langle 1|]\sigma_z = \\ &= -\frac{i}{2}[\Gamma_L|N\rangle\langle N| + \Gamma_R|1\rangle\langle 1|] = \Sigma = -\Sigma^\dagger\,, \end{aligned} \tag{5.20}$$

where the penultimate equality holds for $\Gamma_R = \Gamma_L$, and we used for PHS the hermitian conjugate of (3.17). Transposing the Floquet equation and right multiplying by $C^\dagger$ yields

$$\begin{aligned} i\hbar\partial_t|u_\epsilon(t)\rangle &= [H(t) + \Sigma - \epsilon]|u_\epsilon(t)\rangle \Leftrightarrow \\ \Leftrightarrow i\hbar\partial_t\langle u_\epsilon(t)|^* C^\dagger &= \langle u_\epsilon(t)|^* C^\dagger C[H^{\mathsf{T}}(t) + \Sigma^{\mathsf{T}} - \epsilon]C^\dagger = \langle u_\epsilon(t)|^* C^\dagger[-H^\dagger(t) + C\Sigma^{\mathsf{T}}C^\dagger - \epsilon] \Leftrightarrow \\ \Leftrightarrow -i\hbar\partial_t\langle u_\epsilon(t)|^* C^\dagger &= \langle u_\epsilon(t)|^* C^\dagger[H(t) - C\Sigma^{\mathsf{T}}C^\dagger + \epsilon]\,. \end{aligned} \tag{5.21}$$

Now we apply the parity transformation. Adding an extra label x to the Floquet function ($|u_\epsilon(x,t)\rangle$ is a spinor at the unit cell x)

$$\begin{aligned} -i\hbar\partial_t\langle u_\epsilon(-x,t)|^* C^\dagger P^\dagger &= \langle u_\epsilon(-x,t)|^* C^\dagger P^\dagger P[H(-x,t) - C\Sigma^{\mathsf{T}}(-x)C^\dagger + \epsilon]P^\dagger = \\ &= \langle u_\epsilon(-x,t)|^* C^\dagger P^\dagger[PH(-x,t)P^\dagger - PC\Sigma^{\mathsf{T}}(-x)C^\dagger P^\dagger + \epsilon] = \\ &= \langle u_\epsilon(-x,t)|^* C^\dagger P^\dagger[H(x,t) + \Sigma^\dagger(x) + \epsilon] \Leftrightarrow \\ \Leftrightarrow i\hbar\partial_t PC|u_\epsilon(-x,t)\rangle^* &= [H(x,t) + \Sigma + \epsilon^*]PC|u_\epsilon(-x,t)\rangle^*\,. \end{aligned} \tag{5.22}$$

The Floquet function $PC|u_\epsilon(-x,t)\rangle^*$ has quasienergy $-\epsilon^*$. So we have

$$PC|u_\epsilon(-x,t)\rangle^* = |u_{-\epsilon^*}(x,t)\rangle\,, \tag{5.23}$$

resulting for the Fourier components in

$$PC|u_{-n}(-x,\epsilon)\rangle^* = |u_n(x,-\epsilon^*)\rangle\,. \tag{5.24}$$

Since $PC = i\sigma_y$, we have in particular

$$\langle N|u_{-n}(\epsilon)\rangle^* = \langle N-1|PC|u_{-n}(\epsilon)\rangle^* = \langle 1|u_n(-\epsilon^*)\rangle^*, \tag{5.25}$$

$$\langle 1|u_{-n}(\epsilon)\rangle^* = -\langle 2|PC|u_{-n}(\epsilon)\rangle^* = -\langle N|u_n(-\epsilon^*)\rangle^*\,. \tag{5.26}$$

For the Green function we have

$$\begin{aligned}\mathcal{G}^{(m)}_{1N}(E) &= \sum_{\epsilon\in \mathsf{FZ}}\sum_{n\in\mathbb{Z}} \frac{\langle 1|u_{m+n}(\epsilon)\rangle\langle u^+_n(\epsilon)|N\rangle}{E-\epsilon-\hbar n\Omega} = \sum_{\epsilon\in \mathsf{FZ}}\sum_{n\in\mathbb{Z}} \frac{\langle 1|u_{m+n}(-\epsilon^*)\rangle\langle u^+_n(-\epsilon^*)|N\rangle}{E+\epsilon^*-\hbar n\Omega} = \\ &= -\sum_{\epsilon\in \mathsf{FZ}}\sum_{n\in\mathbb{Z}} \frac{\langle N|u_{-m-n}(\epsilon)\rangle^*\langle u^+_{-n}(\epsilon)|1\rangle^*}{E+\epsilon^*-\hbar n\Omega} = \sum_{\epsilon\in \mathsf{FZ}}\sum_{n\in\mathbb{Z}} \frac{\langle N|u_{-m+n}(\epsilon)\rangle^*\langle u^+_n(\epsilon)|1\rangle^*}{-E-\epsilon^*-\hbar n\Omega} = \left(\mathcal{G}^{(-m)}_{N1}(-E)\right)^*,\end{aligned} \tag{5.27}$$

where we used (5.25) and did the replacements $n \to -n$ and $\epsilon \to -\epsilon^*$. The second replacement is justified since the $\mathcal{PC}$ symmetry divides the spectrum in two parts, if ϵ belongs to the spectrum then $-\epsilon^*$ belongs to the spectrum as well. Thus it is proved that the symmetry $\mathcal{PC}$ renders the charge pumping an even function of the chemical potential. We can point out one more interesting feature from Fig. 5.8. The pumped charge through the inhomogeneous chain looks like a distorted odd function. We ask if there are any conditions for which the pumped charge is an odd function of the chemical potential. The answer is yes.

We reproduce in Fig. 5.10 the pumped charge for an inhomogeneous chain with $\mu = 0$, which can be seen to be an odd function of the chemical potential. The pumped charge for the homogeneous chains is not shown because it is identically zero. This happens because the homogeneous chain has both $\mathcal{PC}$ symmetry and another symmetry that we will discuss next that renders the pumped charge an odd function. This last symmetry to be introduced is a special kind of PHS, that we will call PHS', that is only present when $\mu = 0$. The pumped charge is then both an even and odd function of the chemical potential, so it is identically null. As we did in the previous case, we will look at the transmission probabilities to search for a constraint on the Green function, and later prove it from the symmetry PHS'.

From Fig. 5.11 we can extract the relation

$$|\mathcal{G}^{(m)}_{\alpha\beta}(E)|^2 = |\mathcal{G}^{(-m)}_{\alpha\beta}(-E)|^2\,,\ \alpha\neq\beta\,. \tag{5.28}$$

This results in

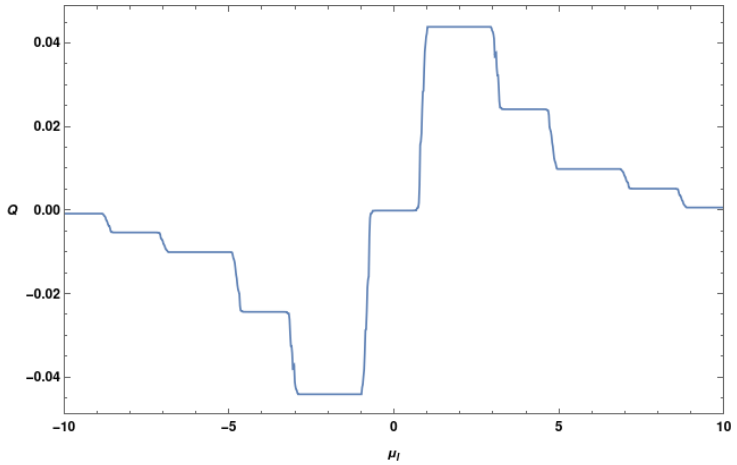

Figure 5.10: Pumped charge over a period as a function of the chemical potential, for an inhomogeneous chain of the zx model. $\mu = 0$, $T = 1.6$, $\Gamma_L = \Gamma_R = 0.5$, $A_L = 2$, $A_R = 6$. 60 sites.

$$Q'(\mu_l) = \frac{eT}{h}\Gamma_L\Gamma_R \sum_{n\in\mathbb{Z}} \left[|\mathcal{G}^{(n)}_{N1}(\mu_l)|^2 - |\mathcal{G}^{(n)}_{1N}(\mu_l)|^2\right] = \\ = \frac{eT}{h}\Gamma_L\Gamma_R \sum_{n\in\mathbb{Z}} \left[|\mathcal{G}^{(-n)}_{N1}(-\mu_l)|^2 - |\mathcal{G}^{(-n)}_{1N}(-\mu_l)|^2\right] = Q'(-\mu_l)\,, \tag{5.29}$$

which implies $Q(-\mu_l) = -Q(\mu_l)$. Here the $\mathcal{PC}$ symmetry is explicitly broken by the non-uniform amplitude of the driving, so we need to resort to the PHS' symmetry. We introduce the operator $\mathcal{O}$, which acting on the Floquet function does the translation $(k,t) \to (k+\pi, t+T/2)$. In the space-time domain $\mathcal{O}$ acts according to

$$\mathcal{O}|u(x,t)\rangle = (-1)^x |u\,(x, t+T/2)\rangle\,. \tag{5.30}$$

Here $x \in \mathbb{Z}$ is the unit cell.

The PHS' symmetry is implemented by the operator $\sigma_z\mathcal{O}\mathcal{K}$, where $\mathcal{K}$ denotes complex conjugation. It is easy to see that

$$\sigma_z\mathcal{O}H^*_\mu(-k,t)\mathcal{O}^{-1}\sigma_z = -H_{-\mu}(-k,t)\,, \tag{5.31}$$

while for the self-energy

$$\sigma_z\mathcal{O}\Sigma^*\mathcal{O}^{-1}\sigma_z = -\Sigma. \tag{5.32}$$

Applying the symmetry transformation to the Floquet equation we write

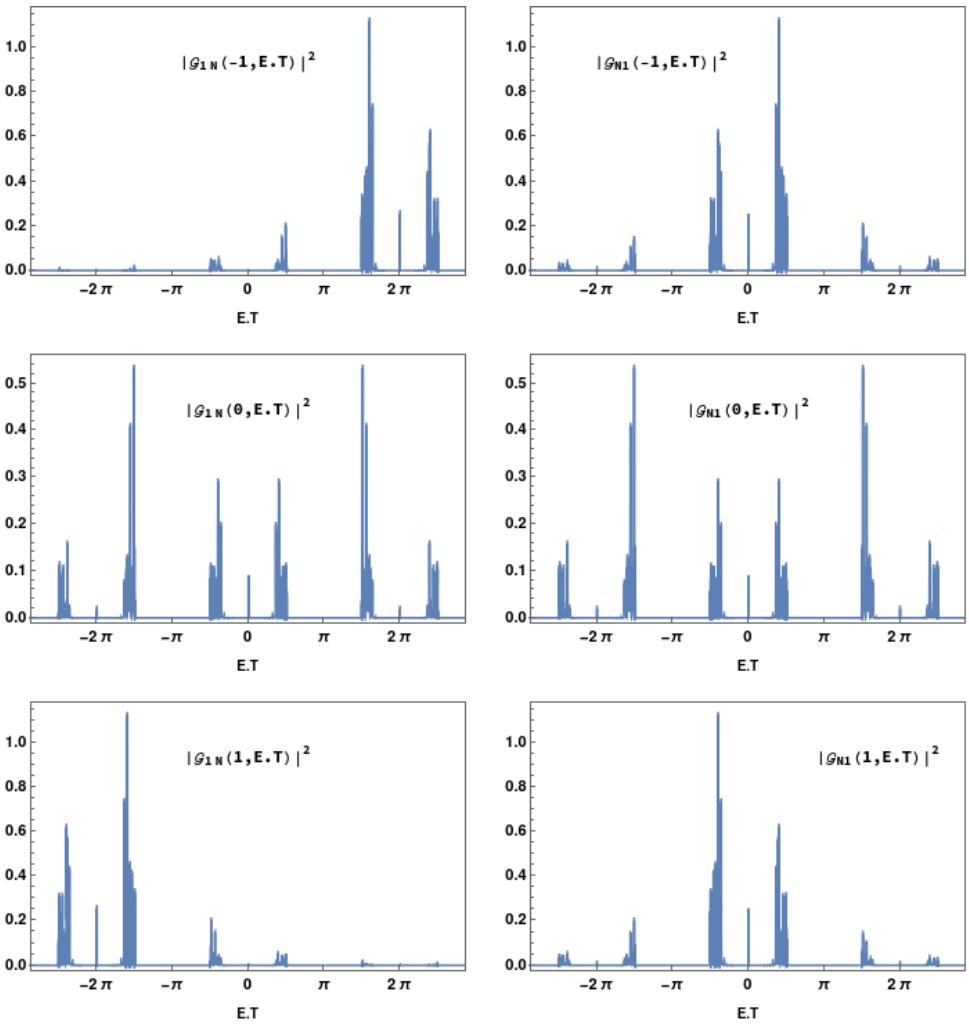

Figure 5.11: Plot of $|\mathcal{G}_{\alpha\beta}(m, E.T)|^2$ against the (adimensional) chemical potential $E.T$, for $m = -1, 0, 1$, $\alpha\beta = 1N, N1$. $\mu = 0$ $T = 1.6$, $\Gamma_L = \Gamma_R = 0.5$, $A_L = 2$, $A_R = 7$. 60 sites.

$$
\begin{aligned}
& i\hbar\partial|u_\epsilon(t)\rangle = [H(t)+\Sigma-\epsilon]\,|u_\epsilon(t)\rangle \\
\Leftrightarrow\ & -i\hbar\sigma_z\mathcal{O}i\hbar\partial|u_\epsilon(t)\rangle^* = \sigma_z\mathcal{O}\,[H^*(t)+\Sigma^*-\epsilon^*]\,|u_\epsilon(t)\rangle^* \Leftrightarrow \\
\Leftrightarrow\ & -i\hbar\sigma_z\mathcal{O}i\hbar\partial|u_\epsilon(t)\rangle^* = [-H_{-\mu}(t)-\Sigma-\epsilon^*]\,\sigma_z\mathcal{O}|u_\epsilon(t)\rangle^* \Leftrightarrow \\
\Leftrightarrow\ & i\hbar\sigma_z\mathcal{O}\partial|u_\epsilon(t)\rangle^* = [H_{-\mu}(t)+\Sigma+\epsilon^*]\,\sigma_z\mathcal{O}|u_\epsilon(t)\rangle^* .
\end{aligned}
\tag{5.33}
$$

Therefore, the state $\sigma_z\mathcal{O}|u_\epsilon(t)\rangle^*$ has quasienergy $-\epsilon^*$ in the Hamiltonian $H_{-\mu}(t)+\Sigma$. In terms of the Fourier components of the Floquet state

$$
\sigma_z\mathcal{O}|u_\epsilon(x,t)\rangle^* = \sum_n \sigma_z|u_n(x,\epsilon)\rangle^*(-1)^{x+n}e^{in\Omega t} = \sum_n \sigma_z|u_{-n}(x,\epsilon)\rangle^*(-1)^{x+n}e^{-in\Omega t} . \tag{5.34}
$$

We are now able to compute the Green function's matrix elements when μ is replaced by $-\mu$:

$$
\begin{aligned}
\left[\mathcal{G}^{(m)}_{1N}(E)\right]_{-\mu} &= \sum_{\epsilon\in\mathsf{FZ}}\sum_{n\in\mathbb{Z}} \frac{\langle 1|u_{m+n}(-\epsilon^*)\rangle\langle u^+_n(-\epsilon^*)|N\rangle}{E+\epsilon^*-n\hbar\Omega} = \sum_{\epsilon\in\mathsf{FZ}}\sum_{n\in\mathbb{Z}} \frac{\langle 1|\sigma_z\mathcal{O}u_{-m-n}(\epsilon)\rangle^*\langle\sigma_z\mathcal{O}u^+_{-n}(\epsilon)|N\rangle^*}{E+\epsilon^*-n\hbar\Omega} \\
&= \sum_{\epsilon\in\mathsf{FZ}}\sum_{n\in\mathbb{Z}} \frac{(-1)^{m+N/2}\langle 1|u_{-m-n}(\epsilon)\rangle^*\langle u^+_{-n}(\epsilon)|N\rangle^*}{E+\epsilon^*-n\hbar\Omega} = \sum_{\epsilon\in\mathsf{FZ}}\sum_{n\in\mathbb{Z}} \frac{(-1)^{m+N/2}\langle 1|u_{-m+n}(\epsilon)\rangle^*\langle u^+_{n}(\epsilon)|N\rangle^*}{E+\epsilon^*+n\hbar\Omega} = \\
&= \sum_{\epsilon\in\mathsf{FZ}}\sum_{n\in\mathbb{Z}} \frac{(-1)^{1+m+N/2}\langle 1|u_{-m+n}(\epsilon)\rangle^*\langle u^+_{n}(\epsilon)|N\rangle^*}{-E-\epsilon^*-n\hbar\Omega} = (-1)^{1+m+N/2}\left[\mathcal{G}^{(-m)}_{1N}(-E)\right]^*_{\mu} ,
\end{aligned}
\tag{5.35}
$$

which implies (5.28) holds when $\mu = 0$.

Now we turn to the xy model, where the Hamiltonian of the chain in momentum space is given by

$$
H_{xy}(k,t) = (\cos k + A\cos(\Omega t)+\mu, \sin k, 0)\cdot\boldsymbol{\sigma} . \tag{5.36}
$$

It enjoys PS with $P=\sigma_x$. Testing the symmetry of the coupling to the leads we write

$$
P\Sigma(-x)P^\dagger = -\frac{i}{2}\sigma_x[\Gamma_L|N-1\rangle\langle N-1| + \Gamma_R|2\rangle\langle 2|]\sigma_x = -\frac{i}{2}[\Gamma_L|N\rangle\langle N| + \Gamma_R|1\rangle\langle 1|] = \Sigma(x),\ \text{if}\ \Gamma_L=\Gamma_R , \tag{5.37}
$$

which means that the system enjoys PS, so we have no charge pumping for homogeneous chains. In fact, due to the presence of PS we have $P|u_\epsilon(-x,t)\rangle = |u_\epsilon(x,t)\rangle$. This results in

$$
\begin{aligned}
\mathcal{G}^{(m)}_{1N}(E) &= \sum_{\epsilon\in\mathsf{FZ}}\sum_{n\in\mathbb{Z}} \frac{\langle 1|u_{m+n}(\epsilon)\rangle\langle u^+_n(\epsilon)|N\rangle}{E-\epsilon-\hbar n\Omega} = \sum_{\epsilon\in\mathsf{FZ}}\sum_{n\in\mathbb{Z}} \frac{\langle N-1|\sigma_x u_{m+n}(\epsilon)\rangle\langle\sigma_x u^+_n(\epsilon)|2\rangle}{E-\epsilon-\hbar n\Omega} = \\
&= \sum_{\epsilon\in\mathsf{FZ}}\sum_{n\in\mathbb{Z}} \frac{\langle N|u_{m+n}(\epsilon)\rangle\langle u^+_n(\epsilon)|1\rangle}{E-\epsilon-\hbar n\Omega} = \mathcal{G}^{(m)}_{N1}(E) ,
\end{aligned}
\tag{5.38}
$$

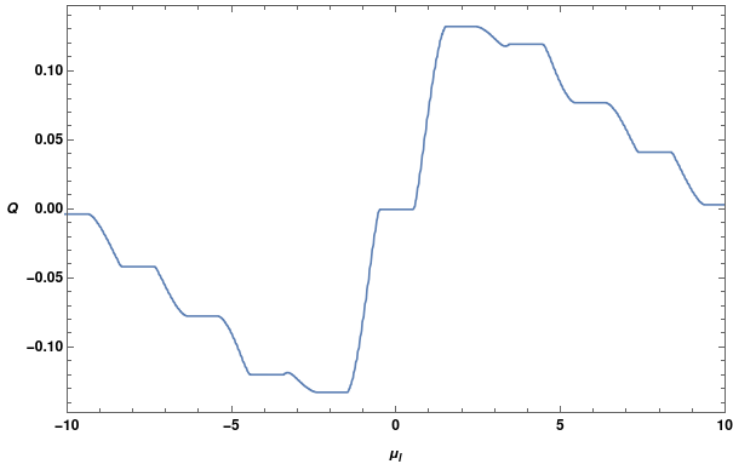

Figure 5.12: Pumped charge over a period as a function of the chemical potential, for an inhomogeneous xy model chain. $\mu = 0.5$, $T = 1.6$, $\Gamma_L = \Gamma_R = 0.5$, $A_L = 2$, $A_R = 6$. 60 sites.

so the pumped charge is null. However, we have charge pumping for inhomogeneous chains. Fig. 5.12 shows that the pumped charge over a cycle is an odd function of the chemical potential when the chain is inhomogeneous. In this case it is the PHS symmetry that explains the result.

For the Hamiltonian of the chain we have

$$\sigma_z H^*_{xy}(-k,t)\sigma_z = -H_{xy}(k,t)\,, \tag{5.39}$$

while for the coupling to the leads

$$\sigma_z \Sigma^* \sigma_z = \frac{i}{2}\sigma_z[\Gamma_L|1\rangle\langle 1| + \Gamma_R|N\rangle\langle N|]\sigma_z = \frac{i}{2}[\Gamma_L|1\rangle\langle 1| + \Gamma_R|N\rangle\langle N|] = -\Sigma\,, \tag{5.40}$$

so the system enjoys PHS. Now recall equation (5.21), which is equivalent to

$$i\hbar\partial_t C|u_\epsilon(t)\rangle^* = [H_{xy}(t) - C\Sigma^* C^\dagger + \epsilon^*]C|u_\epsilon(t)\rangle^*\,. \tag{5.41}$$

This implies that the state $C|u_\epsilon(t)\rangle^*$ has quasienergy $-\epsilon^*$ in the same Hamiltonian $H_{xy}(t) - C\Sigma^* C^\dagger = H_{xy}(t) + \Sigma$, which means that

$$C|u_\epsilon(t)\rangle^* = |u_{-\epsilon^*}(t)\rangle\,. \tag{5.42}$$

For the Fourier components it reads

$$\sigma_z|u_{-n}(\epsilon)\rangle = |u_n(-\epsilon^*)\rangle \Leftrightarrow |u_n(\epsilon)\rangle = \sigma_z|u_{-n}(-\epsilon^*)\rangle\,. \tag{5.43}$$

so that for the Green function we have

$$
\begin{aligned}
\mathcal{G}_{1N}^{(m)}(E) &= \sum_{\epsilon\in \mathsf{FZ}}\sum_{n\in\mathbb{Z}} \frac{\langle 1|u_{m+n}(\epsilon)\rangle\langle u_n^+(\epsilon)|N\rangle}{E-\epsilon-\hbar n\Omega} = \\
&= \sum_{\epsilon\in \mathsf{FZ}}\sum_{n\in\mathbb{Z}} \frac{\langle 1|\sigma_z u_{-m-n}(-\epsilon^*)\rangle^*\langle \sigma_z u_{-n}^+(-\epsilon^*)|N\rangle^*}{E-\epsilon-\hbar n\Omega} = \\
&= \sum_{\epsilon\in \mathsf{FZ}}\sum_{n\in\mathbb{Z}} \frac{\langle 1|\sigma_z u_{-m-n}(-\epsilon^*)\rangle^*\langle \sigma_z u_{-n}^+(-\epsilon^*)|N\rangle^*}{E-\epsilon-\hbar n\Omega} = \\
&= \sum_{\epsilon\in \mathsf{FZ}}\sum_{n\in\mathbb{Z}} \frac{\langle 1|\sigma_z|u_{-m-n}(-\epsilon^*)\rangle^*\langle u_{-n}^+(-\epsilon^*)|\sigma_z|N\rangle^*}{E-\epsilon-\hbar n\Omega} = \\
&= \sum_{\epsilon\in \mathsf{FZ}}\sum_{n\in\mathbb{Z}} -\frac{\langle 1|u_{-m+n}(\epsilon)\rangle^*\langle u_n^+(\epsilon)|N\rangle^*}{E+\epsilon^*+\hbar n\Omega} = \\
&= \sum_{\epsilon\in \mathsf{FZ}}\sum_{n\in\mathbb{Z}} \left(\frac{\langle 1|u_{-m+n}(\epsilon)\rangle\langle u_n^+(\epsilon)|N\rangle}{-E-\epsilon-\hbar n\Omega}\right)^* = \left(\mathcal{G}_{1N}^{(-m)}(-E)\right)^*,
\end{aligned}
\tag{5.44}
$$

which implies $Q(\mu_l) = -Q(-\mu_l)$.

5.3 Heat current

With the tools we have acquired, we can also study the heat flow besides the charge flow, also studied by M. Büttiker in [20], where the Floquet scattering matrix $S_{\alpha\beta}(n, E)$ is used. $S_{\alpha\beta}(n, E)$ is the quantum-mechanical amplitude for an electron with energy E entering the scatterer through lead β to leave the scatterer through lead α having absorbed ($n > 0$) or emitted ($n < 0$) energy quanta $|n|\hbar\Omega$. The scatterer here is the driven chain.

We can define the Floquet scattering matrix as follows. Consider a state

$$
\psi(x,t) = e^{-iEt/\hbar}\sum_n \phi_n(x)e^{-in\Omega t}\,. \tag{5.45}
$$

E is the quasienergy, and the state is a superposition of states with energies $E + n\hbar\Omega$. For scattering states, very far from the central region, the states $\phi_n(x)$ are superpositions of plane waves entering and leaving the central region:

$$
\phi_n(x \to -\infty) = A_n e^{ikx} + C_n e^{-ikx}\,, \tag{5.46}
$$

$$
\phi_n(x \to +\infty) = D_n e^{ikx} + B_n e^{-ikx}\,. \tag{5.47}
$$

Then, the matrix $S(E + n'\hbar\Omega, E + n\hbar\Omega)$ relates the incoming fluxes with the out going fluxes through

$$
\begin{bmatrix} C_{n'} \\ D_{n'} \end{bmatrix} = S(E + n'\hbar\Omega, E + n\hbar\Omega) \begin{bmatrix} A_n \\ B_n \end{bmatrix}. \tag{5.48}
$$

The Floquet scattering matrix includes all $n \in \mathbb{Z}$, so it is a block matrix with four blocks:

$$S = \begin{bmatrix} S_{LL}(n',n) & S_{LR}(n',n) \\ S_{RL}(n',n) & S_{RR}(n',n) \end{bmatrix} . \tag{5.49}$$

The conservation of current implies $SS^\dagger = S^\dagger S = \mathbb{1}$. From now on we will refer to it as scattering matrix only. In what we will do in this section the n appearing in the second argument will be zero, so we simplify the notation by establishing $S(E + n'\hbar\Omega, E) \equiv S(n', E)$. The following relation also holds due to the current conservation

$$\sum_\beta \sum_{n\in\mathbb{Z}} |S_{\beta\alpha}(n,E)|^2 = 1 \,. \tag{5.50}$$

The expression for the directed charge current (4.31) in the lead α using the scattering matrix is [20]

$$\bar{I}_\alpha = \frac{e}{h} \int \mathrm{d}E \left[f_\alpha^{(\mathsf{out})}(E) - f_\alpha^{(\mathsf{in})}(E) \right] , \tag{5.51}$$

where $f_\alpha^{(\mathsf{out})}(E)$ is the distribution function for electrons leaving the scatterer through the lead α and $f_\alpha^{(\mathsf{in})}(E)$ is the distribution function for electrons entering the scatterer through lead α. They are related through

$$f_\alpha^{(\mathsf{out})}(E) = \sum_\beta \sum_{n\in\mathbb{Z}} |S_{\alpha\beta}(-n, E + n\hbar\Omega)|^2 f^{(\mathsf{in})}(E + n\hbar\Omega) \,, \tag{5.52}$$

which alongside (5.50) allows us to rewrite (5.51) in the form

$$\bar{I}_\alpha = \frac{e}{h} \int \mathrm{d}E \sum_{\beta\neq\alpha} \sum_{n\in\mathbb{Z}} \left[|S_{\alpha\beta}(n,E)|^2 f_\beta^{(\mathsf{in})}(E) - |S_{\beta\alpha}(n,E)|^2 f_\alpha^{(\mathsf{in})}(E) \right] . \tag{5.53}$$

For our case of only two leads and choosing $\alpha = L$, the expression above coincides with (4.31) with the identification

$$|S_{LR}(n,E)|^2 = \Gamma_L \Gamma_R |\mathcal{G}_{1N}^{(n)}(E)|^2 \,, \tag{5.54}$$

$$|S_{RL}(n,E)|^2 = \Gamma_L \Gamma_R |\mathcal{G}_{N1}^{(n)}(E)|^2 \,. \tag{5.55}$$

The heat $\mathcal{Q}_\alpha$ entering the lead α per unit time is given by [20]

$$\dot{\mathcal{Q}}_\alpha = \frac{1}{h} \int \mathrm{d}E \, (E - \mu_l) \left[f_\alpha^{(\mathsf{out})}(E) - f_\alpha^{(\mathsf{in})}(E) \right] , \tag{5.56}$$

with all reservoirs at the same chemical potential μ_l. Replacing $f_\alpha^{(\mathsf{out})}(E)$ by (5.52) and multiplying (5.50) by $f_\alpha^{(\mathsf{in})}(E)$ in the second term yields

$$\dot{\mathcal{Q}}_\alpha = \frac{1}{h}\int \mathrm{d}E\ (E-\mu_l)\left\{\sum_\beta\sum_{n\in\mathbb{Z}}|S_{\alpha\beta}(-n,E+n\hbar\Omega)|^2 f_\beta^{(\mathsf{in})}(E+n\hbar\Omega) - \sum_\beta\sum_{n\in\mathbb{Z}}|S_{\beta\alpha}(n,E)|^2 f_\alpha^{(\mathsf{in})}(E)\right\} =$$
$$= \frac{1}{h}\int \mathrm{d}E \sum_\beta\sum_{n\in\mathbb{Z}}(E-\mu_l-n\hbar\Omega)\left\{|S_{\alpha\beta}(-n,E)|^2 f_\beta^{(\mathsf{in})}(E) - (E-\mu_l)|S_{\beta\alpha}(n,E)|^2 f_\alpha^{(\mathsf{in})}(E)\right\} =$$
$$= \frac{1}{h}\int \mathrm{d}E \sum_\beta\sum_{n\in\mathbb{Z}}(E-\mu_l+n\hbar\Omega)\left\{|S_{\alpha\beta}(n,E)|^2 f_\beta^{(\mathsf{in})}(E) - (E-\mu_l)|S_{\beta\alpha}(n,E)|^2 f_\alpha^{(\mathsf{in})}(E)\right\}, \qquad (5.57)$$

where we replaced $E \to E - n\hbar\Omega$ and $n \to -n$ in the first term inside braces. For $\alpha = L$

$$\begin{aligned}\dot{\mathcal{Q}}_L &= \frac{1}{h}\sum_{n\in\mathbb{Z}}\int \mathrm{d}E\ \Big\{(E-\mu_l+n\hbar\Omega)|S_{LL}(n,E)|^2 f_L^{(\mathsf{in})}(E) - (E-\mu_l)|S_{LL}(n,E)|^2 f_L^{(\mathsf{in})}(E) + \\ &\qquad (E-\mu_l+n\hbar\Omega)|S_{LR}(n,E)|^2 f_R^{(\mathsf{in})}(E) - (E-\mu_l)|S_{RL}(n,E)|^2 f_L^{(\mathsf{in})}(E)\Big\} = \\ &= \frac{1}{h}\sum_{n\in\mathbb{Z}}\int \mathrm{d}E\ f(E)\Big\{(E-\mu_l+n\hbar\Omega)|S_{LL}(n,E)|^2 - (E-\mu_l)|S_{LL}(n,E)|^2 + \\ &\qquad (E-\mu_l+n\hbar\Omega)|S_{LR}(n,E)|^2 - (E-\mu_l)|S_{RL}(n,E)|^2\Big\} = \\ &= \frac{1}{h}\sum_{n\in\mathbb{Z}}\int \mathrm{d}E\ f(E)\Big\{n\hbar\Omega|S_{LL}(n,E)|^2 + (E-\mu_l+n\hbar\Omega)|S_{LR}(n,E)|^2 - (E-\mu_l)|S_{RL}(n,E)|^2\Big\},\end{aligned} \qquad (5.58)$$

where we replaced all the distribution functions by the same one $f(E)$, since both reservoirs are at the same temperature and chemical potential. For $\alpha = R$ it is analogous, so

$$\dot{\mathcal{Q}}_R = \frac{1}{h}\sum_{n\in\mathbb{Z}}\int \mathrm{d}E\ f(E)\Big\{n\hbar\Omega|S_{RR}(n,E)|^2 + (E-\mu_l+n\hbar\Omega)|S_{RL}(n,E)|^2 - (E-\mu_l)|S_{LR}(n,E)|^2\Big\}. \qquad (5.59)$$

The terms in LL and RR are reflection terms not present in the charge current, which describe a heating effect caused by the radiation field on each lead when the fermions enter the chain through one lead, exchange photons with the radiation field, and return to same lead. The reflection terms are related to the Green function the same way as the transmission terms, i.e., $|S_{LL}(n,E)|^2 = \Gamma_L^2|\mathcal{G}_{11}^{(n)}(E)|^2$ and $|S_{RR}(n,E)|^2 = \Gamma_R^2|\mathcal{G}_{NN}^{(n)}(E)|^2$. This can be proved using the Keldysh Green function formalism. Now we can either look at the total heating in one cycle $(\dot{\mathcal{Q}}_R + \dot{\mathcal{Q}}_L)2\pi/\Omega \equiv \mathcal{Q}_R + \mathcal{Q}_L$ or at the pumped heat between the leads in one cycle $(\dot{\mathcal{Q}}_R - \dot{\mathcal{Q}}_L)2\pi/\Omega \equiv \mathcal{Q}_R - \mathcal{Q}_L$. From (5.58) and (5.59) we have for the total heat

$$\mathcal{Q}_R + \mathcal{Q}_L = \sum_{n\in\mathbb{Z}}\int \mathrm{d}E\ f(E)\Big\{n\left[|S_{RR}(n,E)|^2 + |S_{LL}(n,E)|^2 + |S_{RL}(n,E)|^2 + |S_{LR}(n,E)|^2\right]\Big\} = \mathcal{Q}_{1,+}, \qquad (5.60)$$

while for the pumped heat

$$\mathcal{Q}_R - \mathcal{Q}_L = \sum_{n\in\mathbb{Z}} \int \mathrm{d}E\; f(E)\Big\{ n\left[|S_{RR}(n,E)|^2\; - |S_{LL}(n,E)|^2 + |S_{RL}(n,E)|^2 - |S_{LR}(n,E)|^2\right] + \left(\frac{2E-2\mu_l}{\hbar\Omega}\right)\left[|S_{RL}(n,E)|^2 - |S_{LR}(n,E)|^2\right]\Big\} = \mathcal{Q}_{1,-} + \mathcal{Q}_2\,, \tag{5.61}$$

where we defined for convenience

$$\mathcal{Q}_{1,\pm} = \sum_{n\in\mathbb{Z}} \int \mathrm{d}E\; f(E) n\left[|S_{RR}(n,E)|^2\; \pm |S_{LL}(n,E)|^2 + |S_{RL}(n,E)|^2 \pm |S_{LR}(n,E)|^2\right], \tag{5.62}$$

$$\mathcal{Q}_2 = \sum_{n\in\mathbb{Z}} \int \mathrm{d}E\; f(E) \left(\frac{2E-2\mu_l}{\hbar\Omega}\right)\left[|S_{RL}(n,E)|^2 - |S_{LR}(n,E)|^2\right]\,. \tag{5.63}$$

The integrals in the previous expressions can be done analitically just as was done for the dc charge current. However, the integral of the term in $\mathcal{Q}_2$ with the energy in the numerator diverges logarithmically. Nonetheless, at zero temperature we can break the integral in two, one from $-\infty$ to 0 and the other from 0 to μ_l. The former diverges with the bandwidth of the electrodes, and does not depend on the chemical potential, so we can discard it. Only the latter integral remains. The expression for (5.62) at zero temperature, with the notation introduced in section 5.2, is given by

$$\mathcal{Q}_{1,\pm} = \Gamma^2 \sum_{n\in\mathbb{Z}} \sum_{\epsilon,\epsilon'\in \mathsf{FZ}} \sum_{m,m'\in\mathbb{Z}} n\left\{ \ln\left[\frac{\mu_l - \epsilon - m\hbar\Omega}{-\infty - \epsilon - m\hbar\Omega}\right] - \ln\left[\frac{\mu_l - \epsilon'^* - m'\hbar\Omega}{-\infty - \epsilon'^* - m'\hbar\Omega}\right]\right\}\times \frac{\langle N|u_{m+n}(\epsilon)\rangle\langle u^+_m(\epsilon)|1\rangle\langle N|u_{m'+n}(\epsilon')\rangle^*\langle u^+_{m'}(\epsilon')|1\rangle^* \pm 1N + NN \pm 11}{\epsilon - \epsilon'^* + (m-m')\hbar\Omega} \tag{5.64}$$

with $\Gamma_L = \Gamma_R = \Gamma$, where $1N$ symbolizes the second term in the numerator obtained by replacing in the first term N by 1 and 1 by N. Similarly for the remaining terms. The expression for (5.63) is given by

$$\mathcal{Q}_2 = 2\Gamma^2 \sum_{n\in\mathbb{Z}} \sum_{\epsilon,\epsilon'\in \mathsf{FZ}} \sum_{m,m'\in\mathbb{Z}} \frac{\langle N|u_{m+n}(\epsilon)\rangle\langle u^+_m(\epsilon)|1\rangle\langle N|u_{m'+n}(\epsilon')\rangle^*\langle u^+_{m'}(\epsilon')|1\rangle^* - N\leftrightarrow 1}{\epsilon - \epsilon'^* + (m-m')\hbar\Omega}\times \left\{\left(\frac{\epsilon-\mu_l}{\hbar\Omega} + m\right)\ln\left[\frac{\mu_l - \epsilon - m\hbar\Omega}{-\epsilon - m\hbar\Omega}\right] - \left(\frac{\epsilon'^* - \mu_l}{\hbar\Omega} + m'\right)\ln\left[\frac{\mu_l - \epsilon'^* - m'\hbar\Omega)}{-\epsilon'^* - m'\hbar\Omega}\right]\right\} \tag{5.65}$$

with $\Gamma_L = \Gamma_R$, where $N\leftrightarrow 1$ symbolizes the second term in the numerator obtained by replacing in the first term N by 1 and 1 by N. To help the study of the odd/even dependence of $\mathcal{Q}_R \pm \mathcal{Q}_L$ on the chemical potential we compute the derivative of $\mathcal{Q}_{1,\pm}$ as in (5.62) and $\mathcal{Q}_2$ as in (5.63) separately, which at zero temperature yields

$$\mathcal{Q}'_{1,\pm}(\mu_l) = \sum_{n\in\mathbb{Z}} n\left[|S_{RR}(n,\mu_l)|^2 \pm |S_{LL}(n,\mu_l)|^2 + |S_{RL}(n,\mu_l)|^2 \pm |S_{LR}(n,\mu_l)|^2\right] \tag{5.66}$$

and

$$\mathcal{Q}_2'(\mu_l) = -2\sum_{n\in\mathbb{Z}}\int_0^{\mu_l}\frac{\mathrm{d}E}{\hbar\Omega}\left[|S_{RL}(n,E)|^2 - |S_{LR}(n,E)|^2\right]. \tag{5.67}$$

First we study the case of the homogeneous zx chain, which has $\mathcal{PC}$ symmetry. Similarly to (5.25) we have

$$\langle 1|u_n(-\epsilon^*)\rangle = \langle N-1|PC|u_{-n}(\epsilon)\rangle^* = -\langle N|u_{-n}(\epsilon)\rangle^*, \tag{5.68}$$

$$\langle u_n^+(-\epsilon^*)|1\rangle = \langle PCu_{-n}^+(\epsilon)|N-1\rangle^* = -\langle u_{-n}^+(\epsilon)|N\rangle^*. \tag{5.69}$$

Using the relations above in the Green function yields

$$\begin{aligned}\mathcal{G}_{11}^{(m)}(E) &= \sum_{\epsilon\in\mathsf{FZ}}\sum_{n\in\mathbb{Z}}\frac{\langle 1|u_{m+n}(\epsilon)\rangle\langle u_n^+(\epsilon)|1\rangle}{E-\epsilon-\hbar n\Omega} = \sum_{\epsilon\in\mathsf{FZ}}\sum_{n\in\mathbb{Z}}\frac{\langle 1|u_{m+n}(-\epsilon^*)\rangle\langle u_n^+(-\epsilon^*)|1\rangle}{E+\epsilon^*-\hbar n\Omega} = \\ &= \sum_{\epsilon\in\mathsf{FZ}}\sum_{n\in\mathbb{Z}}\frac{\left(-\langle N|u_{-m-n}(\epsilon)\rangle^*\right)\left(-\langle u_{-n}^+(\epsilon)|N\rangle^*\right)}{E+\epsilon^*-\hbar n\Omega} = -\sum_{\epsilon\in\mathsf{FZ}}\sum_{n\in\mathbb{Z}}\frac{\langle N|u_{-m+n}(\epsilon)\rangle^*\langle u_n^+(\epsilon)|N\rangle^*}{-E-\epsilon^*-\hbar n\Omega} = \\ &= -\mathcal{G}_{NN}^{(-m)}(-E).\end{aligned} \tag{5.70}$$

Besides having $|S_{LR}(n,E)|^2 = |S_{RL}(-n,-E)|^2$ we now have also $|S_{LL}(n,E)|^2 = |S_{RR}(-n,-E)|^2$, assuming $\Gamma_L = \Gamma_R$.

The derivative of $\mathcal{Q}_{1,\pm}$ choosing the plus sign reads

$$\begin{aligned}\mathcal{Q}_{1,+}'(\mu_l) &= \sum_{n\in\mathbb{Z}} n\left[|S_{LL}(n,\mu_l)|^2 + |S_{RR}(n,\mu_l)|^2 + |S_{LR}(n,\mu_l)|^2 + |S_{RL}(n,\mu_l)|^2\right] = \\ &= \sum_{n\in\mathbb{Z}} n\left[|S_{RR}(-n,-\mu_l)|^2 + |S_{LL}(-n,-\mu_l)|^2 + |S_{RL}(-n,-\mu_l)|^2 + |S_{LR}(-n,-\mu_l)|^2\right] = \\ &= \sum_{n\in\mathbb{Z}} -n\left[|S_{LL}(n,-\mu_l)|^2 + |S_{RR}(n,-\mu_l)|^2 + |S_{LR}(n,-\mu_l)|^2 + |S_{RL}(n,-\mu_l)|^2\right] = \\ &= -\mathcal{Q}_{1,+}'(-\mu_l),\end{aligned} \tag{5.71}$$

which means $\mathcal{Q}_R + \mathcal{Q}_L$ is an even function of the chemical potential. This is illustrated in Fig. 5.13a. To know what happens to the heat pumped over a cycle we look at $\mathcal{Q}_{1,-}'(\mu_l)$ and $\mathcal{Q}_2'(\mu_l)$. We have

$$\begin{aligned}\mathcal{Q}'_{1,-}(\mu_l) &= \sum_{n\in\mathbb{Z}} n\left[|S_{LL}(n,\mu_l)|^2 - |S_{RR}(n,\mu_l)|^2 + |S_{LR}(n,\mu_l)|^2 - |S_{RL}(n,\mu_l)|^2\right] = \\ &= \sum_{n\in\mathbb{Z}} n\left[|S_{RR}(-n,-\mu_l)|^2 - |S_{LL}(-n,-\mu_l)|^2 + |S_{RL}(-n,-\mu_l)|^2 - |S_{LR}(-n,-\mu_l)|^2\right] = \\ &= \sum_{n\in\mathbb{Z}} n\left[|S_{LL}(n,-\mu_l)|^2 - |S_{RR}(n,-\mu_l)|^2 + |S_{LR}(n,-\mu_l)|^2 - |S_{RL}(n,-\mu_l)|^2\right] = \\ &= \mathcal{Q}'_{1,-}(-\mu_l) \end{aligned} \tag{5.72}$$

and

$$\begin{aligned}\mathcal{Q}'_2(\mu_l) &= -2\sum_{n\in\mathbb{Z}} \int_0^{\mu_l} \frac{\mathrm{d}E}{\hbar\Omega}\left[|S_{RL}(n,E)|^2 - |S_{LR}(n,E)|^2\right] = \\ &= -2\sum_{n\in\mathbb{Z}} \int_0^{\mu_l} \frac{\mathrm{d}E}{\hbar\Omega}\left[|S_{LR}(-n,-E)|^2 - |S_{RL}(-n,-E)|^2\right] = \\ &= 2\sum_{n\in\mathbb{Z}} \int_0^{-\mu_l} \frac{\mathrm{d}E}{\hbar\Omega}\left[|S_{LR}(n,E)|^2 - |S_{RL}(n,E)|^2\right] = \\ &= -2\sum_{n\in\mathbb{Z}} \int_0^{-\mu_l} \frac{\mathrm{d}E}{\hbar\Omega}\left[|S_{RL}(n,E)|^2 - |S_{LR}(n,E)|^2\right] = \mathcal{Q}'_2(-\mu_l)\,, \end{aligned} \tag{5.73}$$

which means $\mathcal{Q}_R - \mathcal{Q}_L$ is an odd function of the chemical potential apart from an additive constant. This is in agreement with the result of Fig. 5.13b. For $\mu = 0$ in particular, PHS' is also present, which implies that the heat pumping is even (as will be explained right next), so there is no heat pumping. The total heat remains an even function.

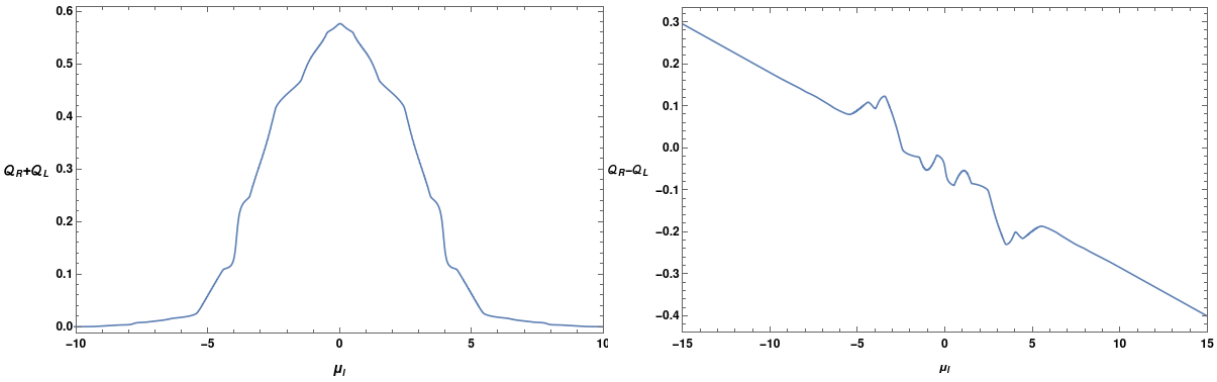

(a) (b)

Figure 5.13: Total (a) and pumped (b) heat over a cycle as functions of the chemical potential, for a homogeneous zx model chain. $A = 2$, $T = 1.6$, $\mu = 0.5$, $\Gamma_L = \Gamma_R = 0.5$. 60 sites.

Now we consider the inhomogeneous chain, which does not have $\mathcal{PC}$ symmetry, but has PHS'. Just as we did in (5.35)

$$\left[\mathcal{G}_{11}^{(m)}(E)\right]_{-\mu} = \sum_{\epsilon\in \mathsf{FZ}}\sum_{n\in\mathbb{Z}} \frac{\langle 1|\sigma_z \mathcal{O} u_{-m-n}(\epsilon)\rangle^* \langle \sigma_z \mathcal{O} u^+_{-n}(\epsilon)|1\rangle^*}{E+\epsilon^*-n\hbar\Omega} = \sum_{\epsilon\in \mathsf{FZ}}\sum_{n\in\mathbb{Z}} \frac{(-1)^{2+m}\langle 1|u_{-m-n}(\epsilon)\rangle^* \langle u^+_{-n}(\epsilon)|1\rangle^*}{E+\epsilon^*-n\hbar\Omega} =$$
$$= (-1)^m \sum_{\epsilon\in \mathsf{FZ}}\sum_{n\in\mathbb{Z}} \frac{\langle 1|u_{-m+n}(\epsilon)\rangle^* \langle u^+_{n}(\epsilon)|1\rangle^*}{E+\epsilon^*+n\hbar\Omega} = (-1)^{m+1} \sum_{\epsilon\in \mathsf{FZ}}\sum_{n\in\mathbb{Z}} \frac{\langle 1|u_{-m+n}(\epsilon)\rangle^* \langle u^+_{n}(\epsilon)|1\rangle^*}{-E-\epsilon^*-n\hbar\Omega} =$$
$$= (-1)^{m+1}\left[\mathcal{G}_{11}^{(-m)}(-E)\right]^*_{\mu}\,. \tag{5.74}$$

The case for $\mathcal{G}_{NN}^{(m)}(E)$ is analogous. This means $|S_{\alpha\beta}(n,\mu_l)|^2 = |S_{\alpha\beta}(-n,-\mu_l)|^2$ holds when $\mu = 0$. Going to expression (5.66)

$$\mathcal{Q}'_{1,\pm}(\mu_l) = \sum_{n\in\mathbb{Z}} n\left[|S_{RR}(n,\mu_l)|^2 \pm |S_{LL}(n,\mu_l)|^2 + |S_{RL}(n,\mu_l)|^2 \pm |S_{LR}(n,\mu_l)|^2\right] =$$
$$= \sum_{n\in\mathbb{Z}} n\left[|S_{RR}(-n,-\mu_l)|^2 \pm |S_{LL}(-n,-\mu_l)|^2 + |S_{RL}(-n,-\mu_l)|^2 \pm |S_{LR}(-n,-\mu_l)|^2\right] =$$
$$= \sum_{n\in\mathbb{Z}} -n\left[|S_{RR}(n,-\mu_l)|^2 \pm |S_{LL}(n,-\mu_l)|^2 + |S_{RL}(n,-\mu_l)|^2 \pm |S_{LR}(n,-\mu_l)|^2\right] =$$
$$= -\mathcal{Q}'_{1,\pm}(-\mu_l)\,, \tag{5.75}$$

and now going to (5.67)

$$\mathcal{Q}'_{2}(\mu_l) = -2\sum_{n\in\mathbb{Z}} \int_0^{\mu_l} \frac{\mathrm{d}E}{\hbar\Omega}\left[|S_{RL}(n,E)|^2 - |S_{LR}(n,E)|^2\right] = -2\sum_{n\in\mathbb{Z}} \int_0^{\mu_l} \frac{\mathrm{d}E}{\hbar\Omega}\left[|S_{RL}(-n,-E)|^2 - |S_{LR}(-n,-E)|^2\right] =$$
$$= 2\sum_{n\in\mathbb{Z}} \int_0^{-\mu_l} \frac{\mathrm{d}E}{\hbar\Omega}\left[|S_{RL}(n,E)|^2 - |S_{LR}(n,E)|^2\right] = -\mathcal{Q}'_{2}(-\mu_l)\,, \tag{5.76}$$

which means $\mathcal{Q}_R \pm \mathcal{Q}_L$ is an even function of the chemical potential. If $\mu \neq 0$, $\mathcal{Q}_R \pm \mathcal{Q}_L$ is neither even nor odd. This is in agreement with the plots of Fig. 5.14.

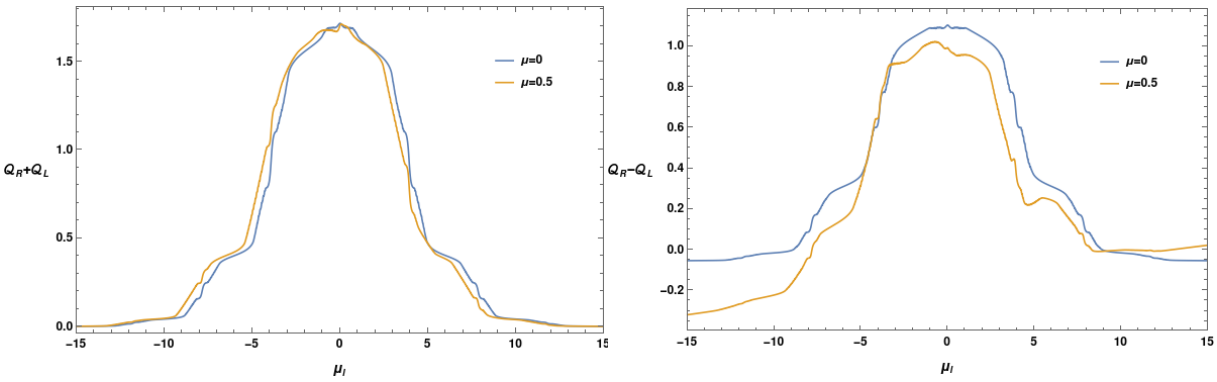

(a) (b)

Figure 5.14: Total (a) and pumped (b) heat over a cycle as functions of the chemical potential, for an inhomogeneous zx model chain. $A_L = 2$, $A_R = 6$, $T = 1.6$, $\Gamma_L = \Gamma_R = 0.5$. 60 sites.

If $\Gamma_L \neq \Gamma_R$, in the homogeneous case with $\mu \neq 0$ the pumped charge and the total heat are no longer even functions of the chemical potential, and the pumped heat is no longer and odd function of the chemical potential (up to a constant), because in this way $\mathcal{PC}$ is broken. Nonetheless, if $\mu = 0$ the pumped charge is an odd function, while both total and pumped heat are even functions, since PHS' is present. If $\mu = 0$ and $\Gamma_L = \Gamma_R$ there is neither charge nor heat pumping, but the total heat is an even function. In the inhomogeneous case, as functions of the chemical potential, the pumped charge is an odd function and $\mathcal{Q}_R \pm \mathcal{Q}_L$ even functions even if $\Gamma_L \neq \Gamma_R$, as long as $\mu = 0$.

In the xy model it was the PHS symmetry that explained relation (5.44) which implies that the pumped charge in a cycle for an inhomogeneous chain is an odd function of the chemical potential. A similar reasoning that led to (5.44) yields

$$\mathcal{G}_{11}^{(m)}(E) = -\left(\mathcal{G}_{11}^{(-m)}(-E)\right)^*, \tag{5.77}$$

$$\mathcal{G}_{NN}^{(m)}(E) = -\left(\mathcal{G}_{NN}^{(-m)}(-E)\right)^*, \tag{5.78}$$

which implies $|S_{\alpha\beta}(n,E)|^2 = |S_{\alpha\beta}(-n,-E)|^2$, so $\mathcal{Q}_R \pm \mathcal{Q}_L$ are even functions of the chemical potential. For a homogeneous chain with $\Gamma_L = \Gamma_R$ PS symmetry is present, so there is neither charge nor heat pumping. However, we have even total heating, as can be seen in Fig. 5.15. If $\Gamma_L \neq \Gamma_R$, then PS is broken, so there is charge and heat pumping. As PHS is still present, the pumped charge is an odd function of the chemical potential and both total heat and pumped heat are even functions of the chemical potential. For an inhomogeneous chain PS is broken, so there is always heat pumping. The PHS is present in this situation as well, so both total heat and pumped heat are even functions of the chemical potential, as can be seen in Fig. 5.16. The fact that $(\mathcal{Q}_R \pm \mathcal{Q}_L)(\mu_l)$ are even functions does not change if $\Gamma_L \neq \Gamma_R$.

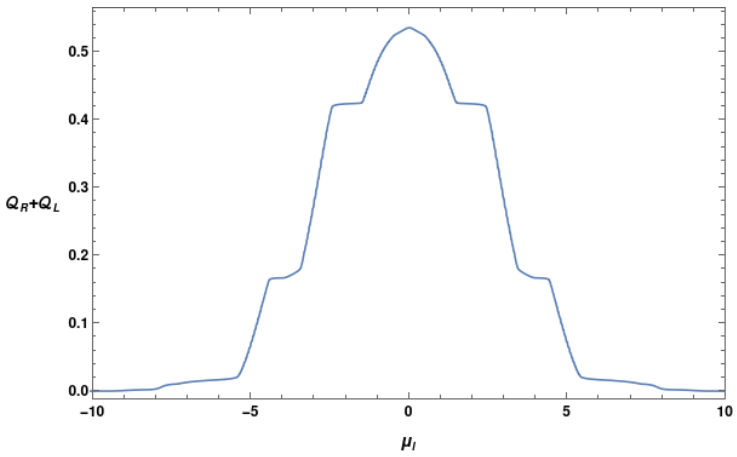

Figure 5.15: Total heat over a cycle a a function of the chemical potential, for a homogeneous xy model chain. $A = 2$, $T = 1.6$, $\mu = 0.5$, $\Gamma_L = \Gamma_R = 0.5$. 60 sites.

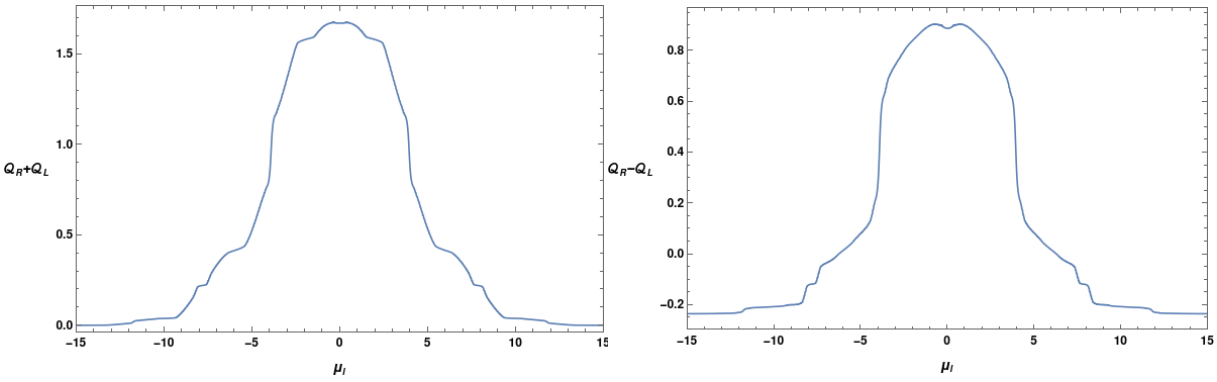

(a) (b)

Figure 5.16: Total (a) and pumped (b) heat over a cycle as functions of the chemical potential, for an inhomogeneous xy model chain. $A_L = 2$, $A_R = 6$, $T = 1.6$, $\Gamma_L = \Gamma_R = 0.5$. 60 sites.

In Table 5.1 we summarize the results obtained for the charge and heat pumping of the zx and xy models we used. This results provide a simple practical criterion to reverse or maintain the direction of the charge or heat flow.

	PHS	PS	$\mathcal{PC}$	PHS'	pumping of charge/heat
$H_{xy} + \Sigma$ (hom)	✓	✓	✓	✓	0
$H_{xy} + \Sigma$ (inhom)	✓	-	-	-	odd/even
$H_{zx}(\mu \neq 0) + \Sigma$ (hom)	-	-	✓	-	even/odd
$H_{zx}(\mu = 0) + \Sigma$ (inhom)	-	-	-	✓	odd/even
$H_{zx}(\mu = 0) + \Sigma$ (hom)	-	-	✓	✓	0
$H_{zx}(\mu \neq 0) + \Sigma$ (inhom)	-	-	-	-	$\approx$ odd/even

Table 5.1: Model symmetries and even/odd charge and heat pumping. For the xy model, PHS' is defined by $\mathcal{OK}$, with no Pauli matrix, contrary to the case of the zx model. This table works only for $\Gamma_L = \Gamma_R$.

Chapter 6

Conclusions and future work

In this work we studied transport properties of topological Floquet systems and charge and heat pumping properties in Floquet systems in the presence of symmetries. We began by introducing Floquet systems in Chapter 2, where we developed useful tools for dealing with periodically driven systems.

Then we moved on to the topic of topological insulators in Chapter 3. First we considered the equilibrium case, where we introduced time-reversal, particle-hole and chiral symmetries and presented the periodic table of topological insulators and superconductors. We gave the example of the SSH model, the paradigmatic example of a topological insulator. We introduced the winding number, the topological invariant for topological chiral systems. Following the discussion of the static case we considered the dynamic one. We reintroduced TRS, PHS and CS for Floquet systems and presented the periodic table of Floquet topological insulators and superconductors. Then we explained how to compute the winding number for the dynamical case.

Then we reproduced the topological phase diagram of the driven SSH chain we introduced in section 3.3, which we called zx model. We concluded Chapter 3 considering inhomogeneous chains. In Chapter 4 we introduced electronic transport in Floquet systems. First we considered the static case to briefly refer to the Landauer-Büttiker formalism. Then we proceeded with the driven case, where we derived the expression for the average current using Floquet Green functions techniques. We explained also how to compute the average current numerically. We finished by defining the differential conductance and the derivative of the pumped current with respect to the chemical potential.

In Chapter 5 we presented the results of this work. First we considered a driven SSH chain in the AI symmetry class. We obtained the phase diagrams based on the winding number of the first order Magnus Hamiltonian. We saw that the average current behaves non-monotonically when the system is in a topological phase, and behaves monotonically when the system is in a non-topological phase. Then we considered the homogeneous zx model, whose transmission spectrum was analyzed. Peaks lying in the gaps were observed whenever the winding number for that gap was non-zero. For inhomogeneous chains we first computed the transmission peaks at zero or $\pm\pi/T$ energy, according to the quasienergies of the bound states, with variable chain size. First we considered a chain with the left portion in the topological phase $(\nu_0, \nu_\pi) = (1, 0)$ and the right one in the phase $(\nu_0, \nu_\pi) = (-1, 0)$, so

that we had in total four zero-energy bound states. We found that the transmission peak at zero energy survives for bigger chain sizes compared to the case of homogeneous chains. This happens so because the additional number of bound states opens additional channels for the electrons to tunnel across the chain. Then we plotted the transmission peaks at $-\pi/T$ and $+\pi/T$ energies for a chain with the left portion in the phase $(\nu_0, \nu_\pi) = (0, 1)$ and right one in the phase $(\nu_0, \nu_\pi) = (0, -1)$, so that we had two bound states at energy $-\pi/T$ and other two at energy π/T. The transmission peaks were observed to survive for bigger chain sizes compared to the homogeneous chains, except for $T_{LR}(-\pi/T)$. However, the peaks at $\pm\pi/T$ energies vanish for chain sizes smaller than the ones for which the peaks at zero vanish.

After studying topology we focused on the study of charge and heat pumping. In the zx model the leads break PS, so we have charge pumping. The homogeneous chain with $\mu \neq 0$ does not have PHS, but has the product of PHS and PS, that renders the pumped charge an even function of the chemical potential and the pumped heat an odd function of the chemical potential. For $\mu = 0$ the system has also a special kind of particle-hole symmetry we called PHS', which renders the pumped charge an odd function of the chemical potential and the pumped heat an even function. Thus, being even and odd functions of the chemical potential, the pumped charge and the pumped heat through homogeneous chains of the zx model with $\mu = 0$ are zero. Inhomogeneous chains of the zx model with $\mu \neq 0$ enjoy none of the symmetries considered, besides TRS. Thus the pumped charge and the pumped heat are neither even nor odd functions of the chemical potential. When $\mu = 0$, the inhomogeneous chain enjoys PHS', so the pumped charge and the pumped heat are odd and even functions of the chemical potential, respectively. In the other model we considered, obtained by a permutation of the Pauli matrices of the xz model, the leads preserve PS, so there is neither pumped charge nor pumped heat for homogeneous chains. In inhomogeneous chains PS is broken, so we have charge and heat pumping. Only PHS symmetry is present, which in this case renders the pumped charge and the pumped heat odd and even functions of the chemical potential, respectively. Basically, we can easily reverse the direction of the charge or heat flow by only tuning the chemical potential.

There are some questions that would make sense to be addressed. One is what happens in higher dimensional systems. FTIs beyond one dimension is already a hot topic [9, 32, 35], and transport in 2D and 3D dimensions open up the range of applications. It would be interesting to study the role of edge (2D) and surface (3D) states in the transport properties. Other important question left out of this work is the occupation number of the Floquet states in open systems. Out of equilibrium quantum statistical mechanics is not so well understood as the equilibrium one, since out of equilibrium the notion of Fermi energy and chemical potential can no longer be used to determine the occupation number of the eigenmodes. Some questions addressed in the literature [40, 41] are when do the open Floquet systems resemble some equilibrium systems and how does the statistical mechanics depend on the system-environment coupling and on the time-periodic modulation. These questions are relevant to experimental control and preparation of the Floquet states. Besides that, we are concerned if it is possible to populate selectively the effective bands carrying nontrivial topological invariants to make the analogy with static topological insulators.

Bibliography

[1] T. Oka and H. Aoki. Photovoltaic hall effect in graphene. *Phys. Rev. B*, 79:081406, Feb 2009. doi: 10.1103/PhysRevB.79.081406. URL https://link.aps.org/doi/10.1103/PhysRevB.79.081406.

[2] I. Esin, M. S. Rudner, G. Refael, and N. H. Lindner. Quantized transport and steady states of floquet topological insulators. *Phys. Rev. B*, 97:245401, Jun 2018. doi: 10.1103/PhysRevB.97.245401. URL https://link.aps.org/doi/10.1103/PhysRevB.97.245401.

[3] T. Iadecola, C. Chamon, R. Jackiw, and S.-Y. Pi. Generalized energy and time-translation invariance in a driven dissipative system. *Phys. Rev. B*, 88:104302, Sep 2013. doi: 10.1103/PhysRevB.88.104302. URL https://link.aps.org/doi/10.1103/PhysRevB.88.104302.

[4] M. König *et al.* Quantum spin hall insulator state in hgte quantum wells. *Science*, 318(5851): 766–770, 2007.

[5] B. A. Bernevig, T. L. Hughes, and S.-C. Zhang. Quantum spin hall effect and topological phase transition in hgte quantum wells. *Science*, 314(5806):1757–1761, 2006. ISSN 0036-8075. doi: 10.1126/science.1133734. URL https://science.sciencemag.org/content/314/5806/1757.

[6] R. Yu, W. Zhang, H. Zhang, and S. Zhang. Quantized anomalous hall effect in magnetic topological insulators. *Nature Physics*, 329(5987):61–64, 2010.

[7] C. Chang *et al.* Experimental observation of the quantum anomalous hall effect in a magnetic topological insulator. *Science*, 340(6129):167–170, 2013.

[8] N. Lindner, G. Refael, and V. Galitski. Floquet topological insulator in semiconductor quantum wells. *Nature*, 7:490–495, 2011. doi: https://doi.org/10.1038/nphys1926.

[9] T. Oka and H. Aoki. Photovoltaic hall effect in graphene. *Phys. Rev. B*, 79:081406, Feb 2009. doi: 10.1103/PhysRevB.79.081406. URL https://link.aps.org/doi/10.1103/PhysRevB.79.081406.

[10] G. Jotzu, M. Messer, R. Desbuquois, M. Lebrat, T. Uehlinger, D. Greif, and T. Esslinger. Experimental realization of the topological haldane model with ultracold fermions. *Nature*, 515:237–240, 2014.

[11] F. D. M. Haldane. Model for a quantum hall effect without landau levels: Condensed-matter realization of the "parity anomaly". *Phys. Rev. Lett.*, 61:2015–2018, Oct 1988. doi: 10.1103/PhysRevLett.61.2015. URL https://link.aps.org/doi/10.1103/PhysRevLett.61.2015.

[12] S. Kohler, J. Lehmann, and P. Hänggi. Driven quantum transport on the nanoscale. *Physics Reports*, 406(6):379 – 443, 2005. ISSN 0370-1573. doi: https://doi.org/10.1016/j.physrep.2004.11.002. URL http://www.sciencedirect.com/science/article/pii/S0370157304005071.

[13] O. Balabanov and H. Johannesson. Transport signatures of symmetry protection in 1d floquet topological insulators. *Journal of Physics: Condensed Matter*, 32(1):015503, oct 2019. doi: 10.1088/1361-648x/ab4319. URL https://doi.org/10.1088%2F1361-648x%2Fab4319.

[14] A. Damascelli, Z. Hussain, and Z.-X. Shen. Angle-resolved photoemission studies of the cuprate superconductors. *Rev. Mod. Phys.*, 75:473–541, Apr 2003. doi: 10.1103/RevModPhys.75.473. URL https://link.aps.org/doi/10.1103/RevModPhys.75.473.

[15] A. Farrell, A. Arsenault, and T. Pereg-Barnea. Dirac cones, floquet side bands, and theory of time-resolved angle-resolved photoemission. *Phys. Rev. B*, 94:155304, Oct 2016. doi: 10.1103/PhysRevB.94.155304. URL https://link.aps.org/doi/10.1103/PhysRevB.94.155304.

[16] P. W. Brouwer. Scattering approach to parametric pumping. *Phys. Rev. B*, 58:R10135–R10138, Oct 1998. doi: 10.1103/PhysRevB.58.R10135. URL https://link.aps.org/doi/10.1103/PhysRevB.58.R10135.

[17] T. A. Shutenko, I. L. Aleiner, and B. L. Altshuler. Mesoscopic fluctuations of adiabatic charge pumping in quantum dots. *Phys. Rev. B*, 61:10366–10375, Apr 2000. doi: 10.1103/PhysRevB.61.10366. URL https://link.aps.org/doi/10.1103/PhysRevB.61.10366.

[18] M. Büttiker, H. Thomas, and A. Prêtre. Current partition in multiprobe conductors in the presence of slowly oscillating external potentials. *Phys. B: Condens. Matter*, 94:133–137, March 1994. URL https://doi.org/10.1007/BF01307664.

[19] L. E. F. Foa Torres. Mono-parametric quantum charge pumping: Interplay between spatial interference and photon-assisted tunneling. *Phys. Rev. B*, 72:245339, Dec 2005. doi: 10.1103/PhysRevB.72.245339. URL https://link.aps.org/doi/10.1103/PhysRevB.72.245339.

[20] M. Moskalets and M. Büttiker. "Floquet scattering theory of quantum pumps". *Phys. Rev. B*, 66 (205320), 2002. doi: https://doi.org/10.1103/PhysRevB.66.205320.

[21] M. Holthaus. Floquet engineering with quasienergy bands of periodically driven optical lattices. *Journal of Physics B: Atomic, Molecular and Optical Physics*, 49(1):013001, nov 2015. doi: 10.1088/0953-4075/49/1/013001. URL https://doi.org/10.1088%2F0953-4075%2F49%2F1%2F013001.

[22] S. H. Simon. *The Oxford solid state basics*. Oxford Univ. Press, Oxford, UK, 2013. URL https://cds.cern.ch/record/1581455.

[23] S. Rahav, I. Gilary, and S. Fishman. Effective hamiltonians for periodically driven systems. *Phys. Rev. A*, 68:013820, Jul 2003. doi: 10.1103/PhysRevA.68.013820. URL https://link.aps.org/doi/10.1103/PhysRevA.68.013820.

[24] M. Di Ventra. *Electrical Transport in Nanoscale Systems*. Cambridge University Press, 2008. doi: 10.1017/CBO9780511755606.

[25] K. v. Klitzing, G. Dorda, and M. Pepper. New method for high-accuracy determination of the fine-structure constant based on quantized hall resistance. *Phys. Rev. Lett.*, 45:494–497, Aug 1980. doi: 10.1103/PhysRevLett.45.494. URL https://link.aps.org/doi/10.1103/PhysRevLett.45.494.

[26] D. Tong. Lectures on the Quantum Hall Effect. *arXiv e-prints*, art. arXiv:1606.06687, June 2016.

[27] C. L. Kane and E. J. Mele. Z_2 topological order and the quantum spin hall effect. *Phys. Rev. Lett.*, 95:146802, Sep 2005. doi: 10.1103/PhysRevLett.95.146802. URL https://link.aps.org/doi/10.1103/PhysRevLett.95.146802.

[28] K. Kawabata, K. Shiozaki, M. Ueda, and M. Sato. Symmetry and topology in non-hermitian physics. *Phys. Rev. X*, 9:041015, Oct 2019. doi: 10.1103/PhysRevX.9.041015. URL https://link.aps.org/doi/10.1103/PhysRevX.9.041015.

[29] S. Ryu, A. P. Schnyder, A. Furusaki, and A. W. W. Ludwig. Topological insulators and superconductors: tenfold way and dimensional hierarchy. *New Journal of Physics*, 12(6):065010, jun 2010. doi: 10.1088/1367-2630/12/6/065010. URL https://doi.org/10.1088%2F1367-2630%2F12%2F6%2F065010.

[30] A. Altland and M. R. Zirnbauer. Nonstandard symmetry classes in mesoscopic normal-superconducting hybrid structures. *Phys. Rev. B*, 55:1142–1161, Jan 1997. doi: 10.1103/PhysRevB.55.1142. URL https://link.aps.org/doi/10.1103/PhysRevB.55.1142.

[31] Y. Ando. Topological insulator materials. *Journal of the Physical Society of Japan*, 82(10):102001, 2013. doi: 10.7566/JPSJ.82.102001. URL https://doi.org/10.7566/JPSJ.82.102001.

[32] J. Cayssol, B. Dóra, F. Simon, and R. Moessner. Floquet topological insulators. *physica status solidi (RRL) – Rapid Research Letters*, 7(1-2):101–108, 2013. doi: 10.1002/pssr.201206451. URL https://onlinelibrary.wiley.com/doi/abs/10.1002/pssr.201206451.

[33] T. Kitagawa, E. Berg, M. Rudner, and E. Demler. Topological characterization of periodically driven quantum systems. *Phys. Rev. B*, 82:235114, Dec 2010. doi: 10.1103/PhysRevB.82.235114. URL https://link.aps.org/doi/10.1103/PhysRevB.82.235114.

[34] M. Fruchart. Complex classes of periodically driven topological lattice systems. *Phys. Rev. B*, 93:115429, Mar 2016. doi: 10.1103/PhysRevB.93.115429. URL https://link.aps.org/doi/10.1103/PhysRevB.93.115429.

[35] S. Yao, Z. Yan, and Z. Wang. Topological invariants of floquet systems: General formulation, special properties, and floquet topological defects. *Phys. Rev. B*, 96:195303, Nov 2017. doi: 10.1103/PhysRevB.96.195303. URL https://link.aps.org/doi/10.1103/PhysRevB.96.195303.

[36] S. Datta. *Electronic Transport in Mesoscopic Systems*. Cambridge Studies in Semiconductor Physics and Microelectronic Engineering. Cambridge University Press, 1995. doi: 10.1017/CBO9780511805776.

[37] C. A. Stafford and N. S. Wingreen. Resonant photon-assisted tunneling through a double quantum dot: An electron pump from spatial rabi oscillations. *Phys. Rev. Lett.*, 76:1916–1919, Mar 1996. doi: 10.1103/PhysRevLett.76.1916. URL https://link.aps.org/doi/10.1103/PhysRevLett.76.1916.

[38] S. W. Kim. Floquet scattering in parametric electron pumps. *Phys. Rev. B*, 66:235304, Dec 2002. doi: 10.1103/PhysRevB.66.235304. URL https://link.aps.org/doi/10.1103/PhysRevB.66.235304.

[39] M. Switkes, C. M. Marcus, K. Campman, and A. C. Gossard. An adiabatic quantum electron pump. *Science*, 283(5409):1905–1908, 1999. ISSN 0036-8075. doi: 10.1126/science.283.5409.1905. URL https://science.sciencemag.org/content/283/5409/1905.

[40] D. E. Liu. Classification of the floquet statistical distribution for time-periodic open systems. *Phys. Rev. B*, 91:144301, Apr 2015. doi: 10.1103/PhysRevB.91.144301. URL https://link.aps.org/doi/10.1103/PhysRevB.91.144301.

[41] T. Iadecola, T. Neupert, and C. Chamon. Occupation of topological floquet bands in open systems. *Physical Review B*, 91(23), Jun 2015. ISSN 1550-235X. doi: 10.1103/physrevb.91.235133. URL http://dx.doi.org/10.1103/PhysRevB.91.235133.

[42] W. Li and L. E. Reichl. Floquet scattering through a time-periodic potential. *Phys. Rev. B*, 60:15732–15741, Dec 1999. doi: 10.1103/PhysRevB.60.15732. URL https://link.aps.org/doi/10.1103/PhysRevB.60.15732.

Appendix A

Fourier transform of XZ model

Recall the zx model's Hamiltonian, here in second quantization

$$H = \sum_k \begin{pmatrix} a_k^\dagger & b_k^\dagger \end{pmatrix} H_{zx}(k,t) \begin{pmatrix} a_k \\ b_k \end{pmatrix} = \sum_k \begin{pmatrix} a_k^\dagger & b_k^\dagger \end{pmatrix} \begin{pmatrix} \mu + A\cos(\Omega t) + \cos k & \sin k \\ \sin k & -\mu - A\cos(\Omega t) - \cos k \end{pmatrix} \begin{pmatrix} a_k \\ b_k \end{pmatrix} =$$
$$= \sum_k \left[(\mu + A\cos(\Omega t) + \cos k) a_k^\dagger a_k + \sin k (b_k^\dagger a_k + a_k^\dagger b_k) + (-\mu - A\cos(\Omega t) - \cos k) b_k^\dagger b_k \right] . \tag{A.1}$$

We will need to change the basis of the creation and annihilation operators:

$$\begin{aligned} a_k &= \frac{1}{\sqrt{N}} \sum_j a_j e^{-ikj} , \\ b_k &= \frac{1}{\sqrt{N}} \sum_j b_j e^{-ikj} . \end{aligned} \tag{A.2}$$

First we will consider the term diagonal in the a operator.

$$\begin{aligned} &\sum_k (\mu + A\cos(\Omega t) + \cos k) a_k^\dagger a_k = \sum_k (\mu + A\cos(\Omega t) + \cos k) \frac{1}{N} \sum_j a_j^\dagger e^{ikj} \sum_{j'} a_{j'} e^{-ikj'} = \\ &= (\mu + A\cos(\Omega t)) \sum_{j,j'} a_j^\dagger a_{j'} \frac{1}{N} \underbrace{\sum_k e^{-ik(j'-j)}}_{N\delta_{j,j'}} + \frac{1}{N} \sum_k \sum_{j,j'} a_j^\dagger a_{j'} \frac{e^{ik} + e^{-ik}}{2} e^{ikj} e^{-ikj'} = \\ &= \sum_{j,j'} (\mu + A\cos(\Omega t)) \delta_{j,j'} a_j^\dagger a_{j'} + \sum_{j,j'} \frac{1}{2} a_j^\dagger a_{j'} \Big(\underbrace{\frac{1}{N} \sum_k e^{ik(j+1-j')}}_{\delta_{j+1,j'}} + \underbrace{\frac{1}{N} \sum_k e^{ik(j-1-j')}}_{\delta_{j-1,j'}} \Big) = \\ &= \sum_{j,j'} \left[(\mu + A\cos(\Omega t)) \delta_{j,j'} + \frac{1}{2} (\delta_{j+1,j'} + \delta_{j-1,j'}) \right] a_j^\dagger a_{j'} . \end{aligned} \tag{A.3}$$

Now we focus in the term in $b_k^\dagger a_k$.

$$\begin{aligned}\sum_k \sin k b_k^\dagger a_k &= \sum_k \frac{e^{ik}-e^{-ik}}{2i}\frac{1}{N}\sum_j b_j^\dagger e^{ikj}\sum_{j'} a_{j'}e^{-ikj'} = \\ &= \frac{1}{2i}\sum_{j,j'} b_j^\dagger a_{j'}\Big(\underbrace{\frac{1}{N}\sum_k e^{ik(j+1-j')}}_{\delta_{j+1,j'}} - \underbrace{\frac{1}{N}\sum_k e^{ik(j-1-j')}}_{\delta_{j-1,j'}}\Big) = \\ &= \frac{1}{2i}\sum_{j,j'} b_j^\dagger a_{j'}(\delta_{j+1,j'}-\delta_{j-1,j'})\,.\end{aligned} \tag{A.4}$$

The term in $a_k^\dagger b_k$ is similar, we just need to exchange the a with the b. The term in $b_k^\dagger b_k$ is similar to the first term we handled, with b replaced by a. Finally, the Hamiltonian in real space is given by

$$\begin{aligned}H &= \sum_{j,j'}\left[(\mu + A\cos(\Omega t))\delta_{j,j'} + \frac{1}{2}(\delta_{j+1,j'}+\delta_{j-1,j'})\right]a_j^\dagger a_{j'} + \sum_{j,j'}\frac{1}{2i}(\delta_{j+1,j'}-\delta_{j-1,j'})b_j^\dagger a_{j'} + \\ &+ \sum_{j,j'}\frac{1}{2i}(\delta_{j+1,j'}-\delta_{j-1,j'})a_j^\dagger b_{j'} + \sum_{j,j'} + \left[-(\mu + A\cos(\Omega t))\delta_{j,j'} - \frac{1}{2}(\delta_{j+1,j'}+\delta_{j-1,j'})\right]b_j^\dagger b_{j'} = \\ &= \sum_{j,j'}^{\text{cells}}\begin{pmatrix}a_j^\dagger & b_j^\dagger\end{pmatrix}\begin{pmatrix}(\mu + A\cos(\Omega t))\delta_{j,j'} + \frac{1}{2}(\delta_{j+1,j'}+\delta_{j-1,j'}) & \frac{1}{2i}(\delta_{j+1,j'}-\delta_{j-1,j'}) \\ \frac{1}{2i}(\delta_{j+1,j'}-\delta_{j-1,j'}) & -(\mu + A\cos(\Omega t))\delta_{j,j'} - \frac{1}{2}(\delta_{j+1,j'}+\delta_{j-1,j'})\end{pmatrix}\begin{pmatrix}a_{j'}\\ b_{j'}\end{pmatrix},\end{aligned} \tag{A.5}$$

which can be written in terms of the Pauli matrices as

$$H = \sum_{j,j'}^{\text{cells}}\begin{pmatrix}a_j^\dagger & b_j^\dagger\end{pmatrix}\mathbf{h}_{j,j'}(t).\boldsymbol{\sigma}\begin{pmatrix}a_{j'}\\ b_{j'}\end{pmatrix} = \sum_{j,j'}^{\text{cells}}\mathbf{h}_{j,j'}(t).\boldsymbol{\sigma}^{\mu\nu}c_{j\mu}^\dagger c_{j'\nu}\,, \tag{A.6}$$

with

$$\begin{aligned}h^x_{j,j'}(t) &= \frac{1}{2i}(\delta_{j+1,j'}-\delta_{j-1,j'})\,, \\ h^y_{j,j'}(t) &= 0\,,\ \text{and} \\ h^z_{j,j'}(t) &= (\mu + A\cos(\Omega t))\delta_{j,j'} + \frac{1}{2}(\delta_{j,j'+1}+\delta_{j,j'-1})\,,\end{aligned} \tag{A.7}$$

and $\mu,\nu = 1,2$ indicate the type of the site in the unit cell.

Appendix B

Topological phase transitions and gap closing

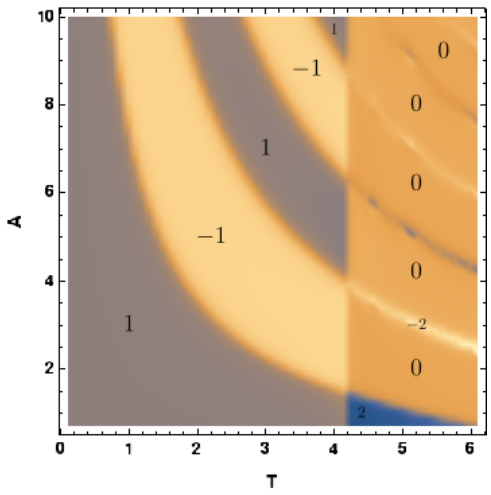

(a) Plot of ν_0.

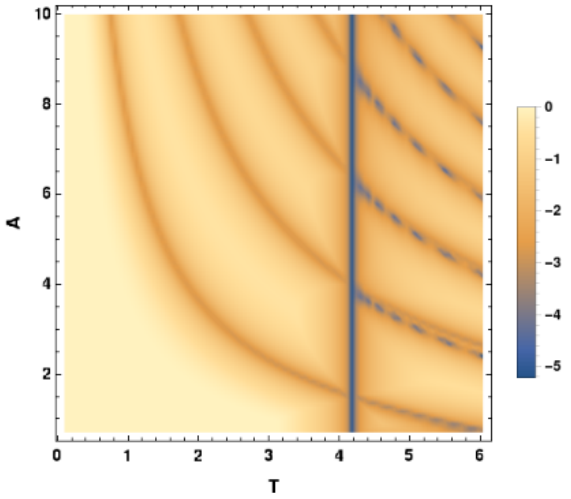

(b) Plot of gap at 0.

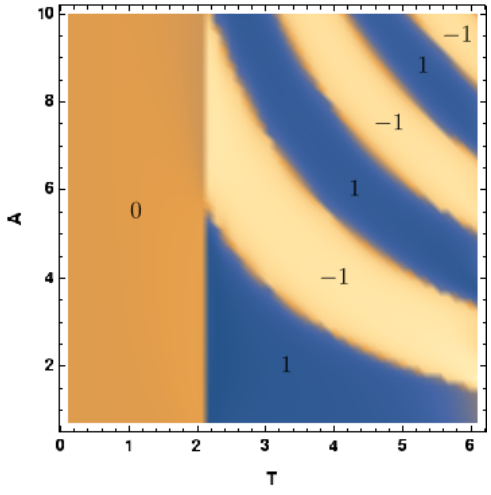

(c) Plot of ν_π

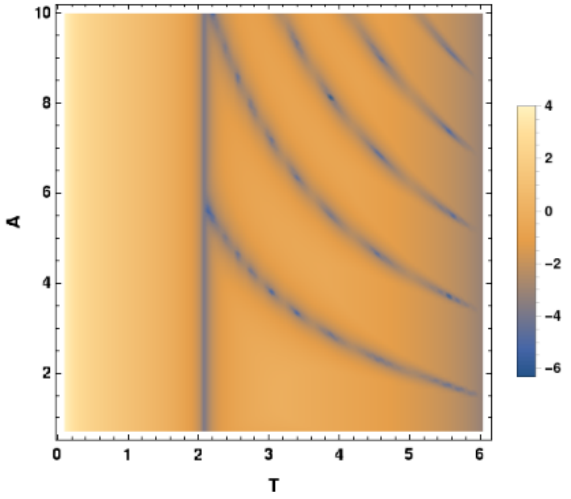

(d) Plot of the gap at π.

Figure B.1: Plot of the winding number side by side with the plot of the respective gap (in logarithmic scale) against the amplitude and period of the driving, for the zx model. We can confirm that the winding at 0 changes when the gap at 0 closes, and the same can be said about the winding at π. $\mu = 0.5$

Appendix C

Symmetries of the Floquet scattering matrix

We present a discussion of the symmetry properties of the Floquet scattering matrix as defined in section 5.3 in general terms, where the asymptotic form of the wave function far from the scatterer assumes a plane-wave form.

We recall here the definition of the main text. We view the Floquet function $\psi(x,t) = \sum_n \phi_n(x) e^{-\frac{i}{\hbar}Et} e^{-in\Omega t}$ with quasi-energy E, as a superposition of states with energies $E + n\hbar\Omega$. For a scattering state, the spatial part of the Floquet functions, $\phi_n(x)$, takes the form of plane waves far from the scatterer:

$$\phi_n(x \to -\infty) = A_n e^{ikx} + C_n e^{-ikx} \tag{C.1}$$

$$\phi_n(x \to +\infty) = D_n e^{ikx} + B_n e^{-ikx}\,. \tag{C.2}$$

The Floquet scattering matrix, $S(E + n'\hbar\Omega, E + n\hbar\Omega)$, relates the Fourier amplitudes of the incoming waves [42] with the outgoing ones:

$$\begin{bmatrix} C_{n'} \\ D_{n'} \end{bmatrix} = S(E + n'\hbar\Omega, E + n\hbar\Omega) \begin{bmatrix} A_n \\ B_n \end{bmatrix}\,. \tag{C.3}$$

We may think of the column vectors as having all entries $n \in \mathbb{Z}$. Then, the S matrix has four blocks:

$$S = \begin{bmatrix} S_{LL}(n',n) & S_{LR}(n',n) \\ S_{RL}(n',n) & S_{RR}(n',n) \end{bmatrix}\,, \tag{C.4}$$

and we rewrite (C.3) as

$$\begin{bmatrix} C^* \\ D^* \end{bmatrix} = S \begin{bmatrix} A^* \\ B^* \end{bmatrix} . \tag{C.5}$$

Probability conservation implies $SS^\dagger = 1$.

We now consider the role of symmetries.

1. TRS: There exists a unitary matrix, T, such that $T\psi^*(x,-t)$ has the same quasi-energy, E. Complex conjugation with $t \to -t$ does not change the time-dependent exponentials, but the spatial part is modified as

$$T\phi_n^*(x \to -\infty) = A_n^* T e^{-ikx} + C_n^* T e^{ikx} , \tag{C.6}$$
$$T\phi_n^*(x \to +\infty) = D_n^* T e^{-ikx} + B_n^* T e^{ikx} , \tag{C.7}$$

   (here it is assumed that T acts on the spinor form of the plane waves). This operation inverts the direction of propagation of the plane waves. We then write

$$\begin{bmatrix} A_{n'}^* \\ B_{n'}^* \end{bmatrix} = S(E + n'\hbar\Omega, E + n\hbar\Omega) \begin{bmatrix} C_n^* \\ D_n^* \end{bmatrix} , \tag{C.8}$$

   Then, from (C.8) and (C.3) we see that

$$\begin{bmatrix} A^* \\ B^* \end{bmatrix} = S \begin{bmatrix} C^* \\ D^* \end{bmatrix} \Leftrightarrow S^\top \begin{bmatrix} C^* \\ D^* \end{bmatrix} = S \begin{bmatrix} C^* \\ D^* \end{bmatrix} . \tag{C.9}$$

   Thus, $S^\top = S$.

2. PHS: There exists a unitary matrix, C, such that the state $C\psi^*(x,t)$ has quasi-energy $-E$. Note that complex conjugation changes both the time and spatial dependence of the exponentials, therefore, the direction of propagation of the waves is not changed. The state $C\psi^*(x,t)$ has the asymptotic behavior:

$$\sum_n \left(A_n^* C e^{-ikx} + C_n^* C e^{ikx}\right) e^{\frac{i}{\hbar}Et} e^{in\Omega t} \text{ as } x \to -\infty ,$$
$$\sum_n \left(D_n^* C e^{-ikx} + B_n^* C e^{ikx}\right) e^{\frac{i}{\hbar}Et} e^{in\Omega t} \text{ as } x \to +\infty . \tag{C.10}$$

   The waves "n" have energy $-E - n\hbar\Omega$. Taking the energy labels into account and the definition of the S matrix, we write

$$\begin{bmatrix} C^*_{n'} \\ D^*_{n'} \end{bmatrix} = S(-E - n'\hbar\Omega, -E - n\hbar\Omega) \begin{bmatrix} A^*_n \\ B^*_n \end{bmatrix}, \tag{C.11}$$

and comparing with (C.3) we get

$$S^*(E + n'\hbar\Omega, E + n\hbar\Omega) = S(-E - n'\hbar\Omega, -E - n\hbar\Omega)\,.$$

In particular, for the case $n = 0$,

$$S^*(E + n'\hbar\Omega, E) = S(-E - n'\hbar\Omega, -E). \tag{C.12}$$

3. Symmetry under $\sigma_3\mathcal{O}\mathcal{K}$ operator: this is the modified PHS for the model H_{zx} at $\mu = 0$, as discussed in the main text.

   The state $\sigma_3\mathcal{O}\phi^*_\epsilon(x,t)$ has quasi-energy $-E$ in the Hamiltonian $H_{-\mu}(t)+\Sigma$. Its asymptotic behavior reads

$$\begin{aligned} &\sum_n \sigma_3 \left(A^*_n e^{-i(k+\pi)x} + C^*_n e^{i(k+\pi)x}\right) e^{\frac{i}{\hbar}Et} e^{in\Omega t + in\pi} \text{ as } x \to -\infty\,, \\ &\sum_n \sigma_3 \left(D^*_n e^{-i(k+\pi)x} + B^*_n e^{i(k+\pi)x}\right) e^{\frac{i}{\hbar}Et} e^{in\Omega t + in\pi} \text{ as } x \to +\infty\,. \end{aligned} \tag{C.13}$$

   Like in the case of PHS, we see that the waves "n" have energies $-E - n\hbar\Omega$. We then can write

$$(-1)^{n'} \begin{bmatrix} C^*_{n'} \\ D^*_{n'} \end{bmatrix} = (-1)^n S^{(-\mu)}(-E - n'\hbar\Omega, -E - n\hbar\Omega) \begin{bmatrix} A^*_n \\ B^*_n \end{bmatrix},$$

   which, compared with the definition (C.3) yields

$$S^*_{(\mu)}(E + n'\hbar\Omega, E + n\hbar\Omega) = S_{(-\mu)}(-E - n'\hbar\Omega, -E - n\hbar\Omega)(-1)^{n+n'}\,. \tag{C.14}$$

   Taking $n = 0$, then

$$S^*_{(\mu)}(E + n'\hbar\Omega, E) = S_{(-\mu)}(-E - n'\hbar\Omega, -E)(-1)^{n'}\,. \tag{C.15}$$

4. PS: There exists a unitary matrix, P, such that the function $P\psi(-x,t)$ has the same quasi-energy, E. The function $P\psi(-x,t)$ then obeys

$$P\phi_n(x \to -\infty) = D_n P e^{ikx} + B_n P e^{-ikx} \tag{C.16}$$

$$P\phi_n(x \to +\infty) = A_n P e^{ikx} + C_n P e^{-ikx}\,, \tag{C.17}$$

so, we write

$$\begin{bmatrix} D \\ C \end{bmatrix} = S \begin{bmatrix} B \\ A \end{bmatrix} \Leftrightarrow \; \sigma_1 S \sigma_1 = S\,, \tag{C.18}$$

where σ_1 acts on the (L, R) subspace. The blocks of the S matrix in (C.4) then obey

$$S_{LL}(n', n) = S_{RR}(n', n) \tag{C.19}$$

$$S_{LR}(n', n) = S_{RL}(n', n)\,. \tag{C.20}$$

In the main text we have simplified the notation for the S matrix by writing $S(E+n\hbar\Omega, E) \equiv S(n, E)$.